

ESTIMATING LIVER IRON NON-INVASIVELY WITH HIGH-FIELD MRI

by

Eamon Doyle

A Dissertation Presented to the
FACULTY OF THE USC GRADUATE SCHOOL
UNIVERSITY OF SOUTHERN CALIFORNIA

In Partial Fulfillment of the
Requirements for the Degree
DOCTOR OF PHILOSOPHY
(BIOMEDICAL ENGINEERING)

December 2017

Copyright 2017

Eamon Doyle

Dedication

To Meghan and my parents for very many things.

Acknowledgments

I would not be here without the support, mentorship, companionship, and patience of so many people throughout my growth as a researcher, scientist and engineer.

I would like to first thank my advisor, John Wood. He taught me to think critically about data, formulate and pursue questions, and wade through confusion to find truth. He has shared his personal interests and time with me in spite of the constant demands from the divergent worlds of research and clinical medicine. In many ways, he is as much my friend as my advisor. I consider it one of the pleasures and privileges of my life to have worked with him as an undergraduate and throughout my PhD.

Second, I wish to thank my lab mate and friend, Adam Bush. From the day I took over half of his office, he has been an boundless source of research ideas and the kinds of rambling discussions that often lead to unexpected insights. I have grown in my understanding of the world through him.

I also would like to thank everyone at Children's Hospital of Los Angeles who worked with me all these years. Dr. Jon Detterich was always willing to take time out of his day to explain fundamentals of physiology and clinical medicine without more than a moment's notice. Dr. Roberta Kato mentored me through the grant writing process and helped me to develop an unlikely idea into a winning grant.

Dr. Thomas Coates provided research space and resources and gave balance and perspective to my thesis committee. Dr. Marvin Nelson and Julia Castro gave me more freedom to use the research magnet than I ever expected a grad student to receive, helping me to develop my ideas quickly. I also benefitted from the hard work of Nathan Smith, Heather Mnoian, Kristin Toy, Bertin Valdez, and Noel Arugay, all of whom were critical to our studies running.

My degree was truly interdisciplinary, in part due to the resources I received at USC. Krishna Nayak co-advised me throughout my PhD work and helped to teach me a variety of technical and theoretical concepts that were invaluable to me. He, and his then-graduate student Kyung Sung, introduced me to MRI research in 2007 and fundamentally changed my path in life.

Through our MRI vendor, Philips Healthcare, I had the pleasure of working with Jon Chia and Tom Perkins, who provided clinical science support to CHLA. They helped start my projects off on the right foot and always helped me to find the technical information I needed to create new things on the scanner.

I would also like to thank a few people who don't fit into one particular category. Sandra Meyers not only helped me to learn Philips pulse programming, she did it with more fun and celebratory dancing than possibly any other pulse sequence has ever received in the early developmental phase. She also welcomed me into her lab at conferences, helping to grow my social and professional networks at the same time. Nilesh Ghugre laid the foundational simulation work that I carried forward and Sam Thornton helped me to extend the simulation framework to answer new questions. There are too many people to thank exhaustively, but I appreciate the help that everyone has given me throughout my time at USC and CHLA.

Finally, I would like to thank my family. My parents taught me the work ethic and commitment that was required of me in my PhD. My sister, Lindsey, provides

me a constant reminder to consider the broader implications of my work. Lastly, to my (almost) wife, Meghan, there simply are not words to describe what you have given me the past 7 years. You started walking this path with me when you proofread my grad school applications in 2010, and what a long, strange trip it has been. Let's start the next one, shall we?

Contents

Dedication	ii
Acknowledgments	iii
List of Tables	ix
List of Figures	x
Glossary	xviii
Acronyms	xx
Abstract	xxii
1 Introduction	1
1.1 Iron Overload Disorders	1
1.1.1 Mechanisms of Iron Overload	1
1.1.2 Iron Storage	3
1.1.3 Treatment for Iron Overload	5
1.1.4 Diagnosis and Monitoring of Iron Overload	9
1.2 Magnetic Resonance and Iron	12
1.2.1 Nuclear Magnetic Resonance	13
1.2.2 Excitation and Acquisition	15
1.2.3 Proton Imaging	20
1.2.4 Spatial Encoding and Selective Excitation	21
1.2.5 Pulse Sequences	26
1.2.6 Interactions with Iron	29
1.3 Monte-Carlo Simulation	29
1.4 Specific Aims & Significance	33
1.4.1 Aim 1 - Translate R_2^* Imaging from 1.5T to 3T	33
1.4.2 Aim 2 - Assess Non-Idealities at 3T	34
1.4.3 Aim 3 - Develop and Test Novel MR-based Iron Quantitation Techniques	34

1.5	Outline	35
2	Improved Liver Iron Estimates using T_1-Corrected Proton Density Estimator	37
2.1	Introduction	38
2.2	Theory	40
2.3	Methods	42
2.3.1	Imaging	42
2.3.2	Simulation	42
2.3.3	Analysis	43
2.4	Results	45
2.5	Discussion	46
2.6	Conclusion	50
2.7	Acknowledgements	50
3	Relaxivity-iron calibration in hepatic iron overload: Predictions of a Monte Carlo model	56
3.0.1	Purpose	56
3.0.2	Methods	56
3.0.3	Results	57
3.0.4	Conclusion	57
3.1	Introduction	57
3.2	Methods	58
3.3	Results	61
3.4	Discussion	63
3.5	Acknowledgements	67
4	Spin Echo-Based Liver Iron Estimates Require B_1^+ Inhomogeneity	72
4.0.1	Purpose	72
4.0.2	Methods	72
4.0.3	Results	73
4.0.4	Conclusion	73
4.1	Introduction	73
4.2	Materials and Methods	74
4.2.1	Patient Population	74
4.2.2	Patient Assessment	75
4.2.3	Simulation	76
4.2.4	Software	78
4.3	Results	78
4.4	Discussion	80
4.5	Conclusions	83

4.6 Acknowledgements	84
5 Ultra-Short Echo Time Images Quantify High Liver Iron	87
5.0.1 Purpose:	87
5.0.2 Theory and Methods:	87
5.0.3 Results:	88
5.0.4 Conclusion	88
5.1 Introduction	88
5.2 Methods	90
5.2.1 Participant Population	90
5.2.2 Participant	94
5.3 Conclusion	100
5.4 Acknowledgments	100
6 Chemical Shift Imaging - A Spectroscopic Approach to Quantifying Iron	109
6.1 Abstract	109
6.1.1 Purpose	109
6.1.2 Theory and Methods	109
6.1.3 Results	110
6.1.4 Conclusion	110
6.2 Introduction	110
6.3 Theory	111
6.4 Methods	113
6.5 Results	116
6.6 Discussion	117
6.7 Conclusion	121
7 Conclusion	129
7.1 Original contributions	130
7.2 Future Work	132
7.3 Summary	134
Reference List	135

List of Tables

1.1	Comparison of common chelators ¹	8
1.2	Common spin nuceli	15
2.1	Relevant scan parameters for patient exam.	51
2.2	Ranges of demographic and laboratory data for the participant population	51
4.1	B_1^+ mean scale values in the whole liver and right and left lobes show that image series from both 1.5T and 3.0T MRI scanners demonstrate significant spatial variation in B_1^+ scale. Further, 3.0T images demonstrate significant mean underexcitation. The mean excitation did not correlate with BMI or weight in 1.5T studies. Underexcitation was weakly associated with weight and BMI at 3T.	84
5.1	Relevant scan parameters	101
5.2	Ranges of demographic and laboratory data for the participant population	102
6.1	R_2 and R_2^* estimates in phantom	121
6.2	3T-CSI and 3T-equivalent R_2^* estimates in four human subjects. Conversion to R_2 is included for reference.	121

List of Figures

1.1	Demonstration of Fenton (Haber-Weiss) reaction, including reaction coefficients showing the extreme reactivity of unbound iron ²	4
1.2	Demonstration of lab and rotating frames used in MRI	14
1.3	Demonstration of precession about a B field with a non-zero transverse RF component	16
1.4	Demonstration of current induced in a coil by time-varying magnetic fields	17
1.5	Example of T ₁ and T ₂ relaxation ³	18
1.6	Demonstration of R ₂ and R ₂ [*] decay with respect to tissue iron content. Reproduced from Wood et al. ⁴	20
1.7	Illustration of approximations of different waveforms with Fourier series. As the number of Fourier coefficients increases, the sum of sine waves becomes a better fit for the waveform. ⁵	22
1.8	Illustration of slice selection producing transverse magnetization in a single slice. The hard pulse with no slice selection gradient produces uniform excitation in the sensitive area of the coil while the sinc pulse with a z-gradient produces excitation of only part of the object.	24
1.9	Illustration of slice selection producing transverse magnetization in a single slice ³	25

1.10	Example of a common multiecho gradient echo pulse sequence.	27
1.11	Example of a common multiecho spin echo sequence.	28
1.12	Illustration of a train of 180° pulses generating multiple spin echoes that decay with T ₂	28
1.13	A demonstration of simulated tissue in 3 dimensions (panels a,b,c) for LIC values of 4.4, 30, and 57.8 ^{mg/g} , respectively. Panels d-f demonstrate 2D projections of 4 μm slices of the 3D geometries; panels g-i show histology samples that demonstrate the similarity with physiologic data that the simulation can achieve. Reproduced from the thesis of Nilesh Ghugre. ⁶	31
2.1	Example of unconstrained and constrained mono-exponential fits for different R ₂ species. When the decay rate is comparable to the first echo time (left), the proton density is underestimated by 8% and the R ₂ is overestimated by 10%. The same trend is seen to a more extreme degree in the right pane where the R ₂ is shorter.	52
2.2	Unconstrained fits of acquired CPMG data plotted against LIC demonstrated that curves derived by Christoforidis show similar fit to the data. The disagreement in slope of fit compared to the Christoforidis-R ₂ [*] curve likely results from the apparent saturation of their protocol due to shorted TE of 2.24 ms in the gradient echo protocol.	53
2.3	Comparison of fitting techniques. Top pane demonstrated the weak relationship between R ₂ and LIC in the unconstrained fits. Lower pane shows the approximate tripling of the calibration curve with the addition of the PDE constraint.	54

2.4 Constrained vs unconstrained fitting of Jensen curve demonstrates that sensitivity of the RR_2 parameter (top pane) follows the behavior of the unconstrained R_2 estimates. The unconstrained aggregation parameter (lower pane) was less correlated tissue iron content but demonstrated large variation. In contrast, the constrained RR_2 saturates quickly; the aggregation parameter (lower pane) increases with iron for the constrained fits. This suggests that the background RR_2 may represent saturating ferritin stores while the a parameter represents large iron particles.	55
3.1 Comparison between simulated relaxivities (x) and clinical calibration curves at 1.5T for both $R2^*$ (a) and $R2$ (b). The clinical calibration curves are reproduced from the literature ^{7,4} , and represent the behavior of in vivo patient data from large clinical trials. Simulated relaxivities at 3T(o) are included for comparison, although no corresponding clinical calibration curves exist. Note that the model predictions for $R2^*$ are highly linear and in agreement with the clinical calibration curves at 1.5T.	68
3.2 Relationship between relaxation rates at 3T and 1.5T. For both $R2^*$ (a) and $R2$ (b), model predictions (x) were highly linear ($R>0.99$) across field strength, and in good agreement with in vivo patient data (o).	69
3.3 Enhancement of $R2^*$ and $R2$ relaxivities with field strength, relative to 1.5T. For $R2^*$, the predicted enhancement varied linearly with field strength, while it was curvilinear for $R2$. At 3T, the predicted relaxivity enhancements agree well with the values calculated from in vivo data.	70

3.4 Bland-Altman plots between matched pairs of 3T simulated and patient data. R _{2*} (a) showed no significant bias and a standard deviation of 3.6%. R ₂ (b) also showed no bias and a standard deviation of 7.2%.	71
4.1 Spatial maps of B ₁ ⁺ scale in patients demonstrate significantly different behavior at 1.5T and 3T. 1.5T maps demonstrate largely uniform excitation patterns and consistently complete excitation. 3T maps demonstrate significant spatial variation in B ₁ ⁺ as well as a mean achieved B ₁ ⁺ of only 69.6%.	85
4.2 Single echo simulations over a wide range of iron loads and B ₁ ⁺ inhomogeneities demonstrate that iron is overestimated in the presence of B ₁ ⁺ inhomogeneity at 1.5T. Further, inaccuracies increase with iron load for a given B ₁ ⁺ . Although 1.5T R ₂ estimates tend to increase with B ₁ ⁺ variation, 3T maps show the opposite effect due to the combination of fast initial decay and lengthened T ₁ resulting in artificially flat decay curves. (B ₁ ⁺ Fraction = B ₁ ⁺ Scale/100)	86
4.3 CPMG simulations over a wide range of iron loads and B ₁ ⁺ inhomogeneities demonstrates that iron is overestimated in the presence of B ₁ ⁺ inhomogeneity except with low iron loads at high B ₁ ⁺ inhomogeneities. (B ₁ ⁺ Fraction = B ₁ ⁺ Scale/100)	86

5.1	Phantom results demonstrate linear correlation of MnCl ₂ concentration and R ₂ [*] . Regression analysis demonstrated the following relationships: R ₂ [*] -UTE = 117×[mM MnCl ₂] + 1.6 ($r^2 = 0.9955$, $r_{adj}^2 = 0.9951$, p<0.0001); R ₂ [*] -GRE = 120×[mM MnCl ₂] + 3.5 ($r^2 = 0.9998$, $r_{adj}^2 = 0.9998$, p<0.0001). The R ₂ [*] -GRE regression excluded the highest-concentration vial due to expected failure of fitting. 95% confidence intervals are shown with dashed lines for each regression.	103
5.2	Example images demonstrating image quality of 3T-UTE (above) and 3T-GRE(below) first echo images and associated R ₂ [*] maps. The image selected is from a subject with high LIC, causing the failure of the 3T-GRE protocol to capture sufficient signal to perform R ₂ [*] estimation.	104
5.3	Scatter plot demonstrating LIC estimates made with 3T GRE and 3T UTE image series compared with clinical estimates. Catastrophic failure in LIC estimates is apparent in 3T GRE estimates for participants with clinical iron loads over 25 mg/g. Points in the shaded region demonstrate 3T-UTE LIC estimates that exceed the upper limit that 1.5T-GRE can quantify.	105

5.6	Simulation of 3T-GRE and 3T-UTE echo times with 0, 5, 10, and 20% PDFF over an LIC range of 0.5-45 mg/g demonstrate that increasing fat fraction has a greater effect on R_2^* for the UTE sequence than the GRE sequence. In particular, the 3T-UTE overestimates LIC more as PDFF increases for a given LIC. Further, at low LIC, the simulations for PDFF=0% indicate that LIC is overestimated when noise is present and the decay rate is slow. The magnitude of error due to physiologically realistic PDFF may explain the increased apparent measurement variation between GRE and UTE.	108
6.1	Comparison if sinc (blue), Dolph-Chebyshev (green), and Tukey (red) excitation pulses for a given flip angle.	122
6.2	Achieved slice profile for Sinc Pulse	122
6.3	Achieved slice profile for Dolph-Chebyshev pulse	123
6.4	Layout of the phantom demonstrating, from top to bottom, left to right, bottles of Philips Solution 11, mineral oil, tap water, 1mM MnCl ₂ , tap water, and 3mM MnCl ₂	123
6.5	Regression of phantom R_2^* estimates. The water vial was excluded due to inability to differentiate it from surrounding MnCl ₂ vials in the CSI R_2^* and S_0 images. The slope is notably steeper than the expected relationship. However, the magnet reported an unreliable shim for the CSI sequence, which can lead to accelerated R_2^* decay. .	124
6.6	Comparison of standard image and R_2^* map with CSI S0 image and R_2^* map. Slice location is not preserved between the images shown. .	125
6.7	Regression of clinically-obtained 3T R_2^* estimates and CSI R_2^* estimates in four human subjects.	126

6.8 A demonstration of signal from a single voxel (blue curve) and resulting fit (red curve). The ExpC model (left) displays reasonable relaxation estimation behavior even in the presence of increased spectral content. The spectral fit (right) fails, likely due to the high order of the model; this often leads to overestimating PDFF significantly.	127
6.9 B_1^+ map demonstrating the wide variety of flip angles achieved in the phantom.	128

Glossary

1-hydrogen todo. 20

ferritin An iron storage molecule that can store significant quantities of iron, found primarily in the liver. 9

flip angle The angle of excitation relative to the axis of B_0 achieved by an RF pulse. 16

Fourier transform A set of forward and inverse mathematical transforms that converts signals between the time domain in which they are acquired and the frequency domain, representing the spectral content of the signal.. 21

gradient Time-varying magnetic fields that allow spatial localization of MRI signals. 21

gyromagnetic ratio todo. 14

magnetic flux magentic flux. 17

relaxation The thermodynamic process in which the net magnetization of a cohort of spins returning to equilibrium after excitation, coninciding with a loss in transverse magnetization and a recovery of longitudinal magnetization. 17

signal-to-noise ratio todo. 28

Acronyms

CT computed tomography. 10, 11

DC direct current. 10

FID free induction decay. 19

G6PD glucose-6-phosphate dehydrogenase deficiency. 2

IV intravenous. 3, 6, 8

milligrams per gram, mg/g milligrams of iron per gram of dry liver tissue. 4,
11, 12, 129

MRI magnetic resonance imaging. xxii, 11

MRS magnetic resonance spectroscopy. xxii

NMR nuclear magnetic resonance. 13, 20

PPM parts-per-million. 29

RF radio frequency. 10, 15, 16

SAR specific absorption rate. 111

SCD sickle cell disease. 2

SQUID superconducting quantum interference device. 10, 11

T Tesla. xxii

Abstract

Magnetic resonance imaging (MRI) has facilitated important advancements in the clinical diagnosis and longitudinal monitoring of tissue iron overload disorders. MRI at 1.5 Tesla (T) has supplanted invasive approaches such as liver biopsy with a non-invasive test and allows for iron assessment in organs including the heart, pancreas, and spleen rather than solely relying on the liver as a surrogate for total-body iron. Most MRI approaches depend on iron's significant paramagnetic effects which noticeably increase R_2 ($1/T_2$) or R_2^* ($1/T_2^*$). However, the increasing popularity of 3T MRI scanners, also known as magnets, is threatening the availability of clinical iron overload diagnosis. The proliferation of 3T scanners has not coincided with improvements in signal acquisition and analysis techniques for fast decay species, leading to a reduction in the quantifiable range of tissue iron as field strength grows. Imaging centers without a 1.5T magnet are therefore unable to quantify the upper half of the clinically-relevant iron range. Though previous studies have demonstrated enhancement of R_2 and R_2^* with field strength, a theoretical basis for the relationship between decay rates and tissue iron at arbitrary field strengths has not been developed. Overcoming these new limitations requires the development of novel scan techniques, improvements to curve fitting approaches, validation of liver iron-relaxation calibration curves, and corrections for non-idealities present at higher field strengths. I pursued these open questions by implementing

echo and gradient echo MRI and magnetic resonance spectroscopy (MRI) pulse sequences with reduced echo times, developing and applying a Monte Carlo Bloch simulation framework to conduct experiments in-silico, scanning humans and calibrated phantoms, and comparing results with clinically-obtained standard values. Spin echo-based R_2 estimates were attractive due to the demonstrated sub-linear enhancement with field strength while gradient echo-derived R_2^* was shown to grow approximately linearly with field strength. However, I found that spin echoes were more susceptible to imaging confounders at 3T than gradient echo approaches. I significantly increased the sensitivity of R_2 to liver iron by deriving signal constraints from within the same image series without additional scan time. Further, I demonstrated that excitation imperfections grew from 1.5T to 3T and quantified the effects on estimated R_2 to demonstrate the need for correction. By developing a ultra-short echo time gradient echo protocol for use in humans, I achieved R_2^* quantitation robust to 3T imaging confounders; this technique demonstrates reliable LIC estimates exceeding 50^{mg/g}, representing a 25% improvement over the dynamic range of 1.5T techniques. Finally, I demonstrated that short TE spin echo spectroscopy shows promise as a method to simultaneously estimate R_2 and R_2^* with high SNR. Overall, these techniques and findings represent a significant step toward the clinical application of 3T-MRI for monitoring tissue iron overload and provide useful insight to extend the dynamic range of iron quantitation at all field strengths.

Chapter 1

Introduction

1.1 Iron Overload Disorders

1.1.1 Mechanisms of Iron Overload

Iron is a critical element in cells. It is necessary for oxygen transport and plays an important role in a wide variety of biological reactions. However, iron is also highly reactive and leads to cell damage if improperly stored. Iron storage is therefore tightly regulated to ensure that cells have access to the necessary quantities for survival without allowing iron to exist in an unbound, reactive state. When a disease or genetic condition results in excessive iron storage in the body, it is known as hemochromatosis or iron overload. Iron overload occurs because the body is unable to substantially increase the rate of iron excretion in response to elevated iron levels. When the origin of iron overload is genetic, the intestinal tract over-absorbs dietary iron, a condition known as hereditary hemochromatosis. Iron accumulation due to other diseases or their requisite treatments is called secondary hemochromatosis.

Primary Hyperabsorption

Hereditary hemochromatosis results from a number of genetic mutations that cause the body to overabsorb iron through the digestive tract. Common hereditary hemochromatosis is the most common inherited genetic disorder in Americans of

Northern European descent, affecting 1 in 250-300 people; it is carried by approximately 1 in 10 white Americans⁸.

Secondary Hemochromatosis

Secondary hemochromatosis can occur when any factor other than the genetic predisposition to over-absorption leads to increases in total body iron. Iron can accumulate in the body due to disorders causing the over-retention of iron, under-utilization of iron by the bone marrow during erythropoiesis, or blood transfusion. Certain cancers, chronic liver disease, and alcoholism can cause iron overload, often through changes to regulatory proteins such as ferroportin⁹. However, the most severe cases of iron overload are seen in severe anemias.

Though the term “anemia” often colloquially refers to insufficient iron intake, or nutritional anemia, anemias represent a much larger group of disorders that result in lower-than-normal red blood cell counts. Severe anemias that cause insufficient erythropoiesis ultimately lead to hemochromatosis. Anemias have many origins ranging from red blood cell production to individual cell longevity. Hemoglobinopathies are genetic conditions in which a patient produces insufficient or abnormally-structured hemoglobin, which can alter the function of red blood cells. Thalassemia, for example, is common in Italian, Greek, Middle Eastern, South Asian, and African descendants¹⁰ and leads severe anemia; oxygen transport is compromised due to insufficient quantities of hemoglobin. Hemolytic anemias, such as glucose-6-phosphate dehydrogenase deficiency (G6PD), result in the premature death of red blood cells. In aplastic anemias like Blackfan-Diamond syndrome, the bone marrow produces an insufficient quantity of red blood cells. Even certain cancers, called myelodisplasias, prevent the maturation of red blood cells in the bone marrow. The diseases vary widely in their origin and sometimes

demonstrate overlap. Sickle cell disease (SCD), a genetic disorder in the equatorial regions around the globe, produces abnormal hemoglobin that polymerizes when deoxygenated, drastically reducing red blood cell survival time — as such, SCD is both a hemoglobinopathy and a hemolytic anemia. Despite their differences, all anemias result in low red blood cell counts that require treatment to improve the patient’s health or ensure survival.

Treatment for anemias is dependent on the origin of the disease. For nutritional anemias, increasing dietary iron intake often resolves the problem, though intravenous (IV) iron may be used as well. Transfusion-dependent anemias, including many forms of aplastic and hemolytic anemias and hemoglobinopathies, require patients to receive red blood cell transfusion therapy about once every 3-4 weeks. Iron overload resulting from transfusion is known as transfusional siderosis. Although iron is normally absorbed through the digestive tract, transfusion circumvents physiologic mechanisms by introducing hemoglobin-bound iron directly into the blood stream at a rate that overwhelms physiologic excretion pathways.

1.1.2 Iron Storage

Iron is both a critical element for the human body and a highly reactive element that can severely damage cells when not appropriately stored. Most tissues in the body do not contain significant quantities of iron under normal circumstances. Notable exceptions are macrophages in the liver, spleen, lymph nodes, and bone marrow. The liver is responsible for excess iron storage and buffering, containing special receptors that permit the uptake of larger-than-normal quantities of iron. The bone marrow uses iron to create the hemoglobin found in circulating erythrocytes. When iron exists in an the Fe^{2+} oxidation state, ions can enter cells through

calcium channels¹¹, leading to the deposition of iron in tissues where intracellular ferritin buffers and converts it to Fe^{3+} . The heart, for example, will not take up iron under normal circumstances. However, cardiac iron overload can occur in transfusion-dependent patients, leading to arrhythmias and high likelihood of cardiogenic death¹². Although iron can be toxic through multiple mechanisms, unbound iron can create free radicals via the Fenton reaction (or Haber-Weiss) which are highly reactive and will damage surrounding cells.

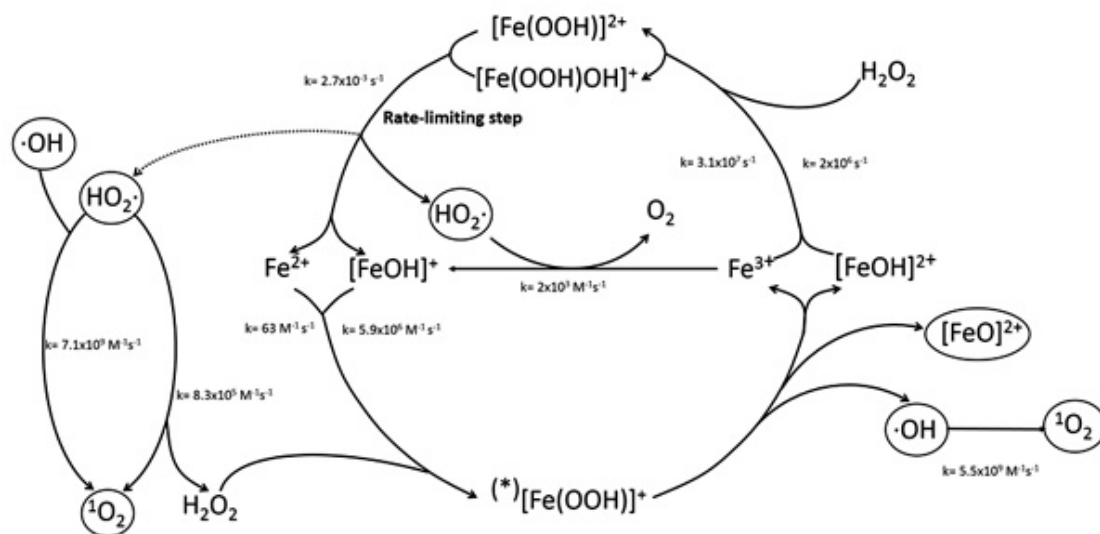


Figure 1.1: Demonstration of Fenton (Haber-Weiss) reaction, including reaction coefficients showing the extreme reactivity of unbound iron²

To prevent tissue damage, iron is tightly regulated in the body. The body's first line of defense against iron storage is transferrin, a circulatory iron-binding protein that is responsible for capturing any unbound iron in the blood and safely shuttling it into the bone marrow for recycling or liver for longer-term storage. Cells throughout the body express a receptor called transferrin receptor 1, TfR1, which

is down-regulated when intracellular Fe^{2+} is present in sufficiently high concentrations. The liver also possesses cells with a second transferrin receptor, TfR2, which does not down-regulate the uptake of transferring in spite of high intracellular ferric iron. When the liver receives transferrin-bound iron, the iron is transferred to ferritin, a large iron storage molecule that can store about 4500 iron atoms distributed between its 24 identical protein subunits¹³. The liver has enough ferritin to store about 3mg/g , about 6 times the normal liver iron load. Once the liver's ferritin stores are saturated, ferritin will begin to aggregate and break down into small iron-rich granules up to about 800 nm in size called hemosiderin, complexes of ferritin, products of ferritin breakdown, and iron. Hemosiderin can store iron in a more concentrated form than ferritin; the iron is in the Fe^{3+} oxidation state and therefore is not accessible to take place in physiological reactions.

1.1.3 Treatment for Iron Overload

Iron has profound effects on a number of organs. Iron has been shown to cause liver disease¹⁴, endocrine dysfunction, myocardial damage^{15,12}, and cognitive effects¹⁶. It is therefore critical to maintain healthy iron levels to prevent tissue damage to many organs.

Phlebotomy

The treatment for iron overload resulting from hereditary hemochromatosis is straight-forward, requiring only phlebotomy (blood-donation) to maintain safe tissue iron levels. Patients will generally donate a unit of blood once every 2-4 weeks to rapidly decrease total body iron and then maintain a safe level by donating blood about 3-6 times per year¹⁷.

Chelation

Treatment of secondary hemochromatosis is more challenging. Because phlebotomy would simply undo the transfusion treatment used for anemias, a pharmacological approach called chelation therapy is used to remove iron. Chelation therapy involves the use of intravenous, subcutaneous, or oral drugs that bind to metals in the body and safely remove them through the kidneys or gastrointestinal tract.

Careful monitoring of iron stores is important for clinical decision making because chelation therapy is both disease-dependent and patient-dependent. Some drugs are more effective at binding to iron in the blood stream to reduce exposure to free iron while others can penetrate cells to reduce iron stores. Physicians depend on regular (generally, annually or semi-annually) iron estimates to assess the effectiveness of a prescribed treatment at removing excess iron for at-risk organs. Further, uncontrolled chelation therapy can be toxic: chelators have the potential to remove physiologically necessary iron or other metals such as magnesium, leading to kidney damage, neurotoxicity, arthritis, bone development, and reductions in platelet and neutrophil counts^{18,19}. For these reasons, safe and accurate iron monitoring techniques are key.

Despite the importance of chelation therapy, patient compliance is often challenging. Notably, chelators have a variety of negative side-effects including headache, nausea, vomiting, and diarrhea. IV and subcutaneous treatment can cause burning sensations at the injection site and skin irritation. Issues of practicality also affect compliance. Oral chelators require the patient to remember their medication regimen multiple times per day while IV requires proximity to equipment, whether the treatment is in a clinical or home setting. Motivating a patient to tolerate these effects is challenging in the absence of demonstrable short-term

benefit. Diagnostic tests for iron that are safe for both regular and long-term use can motivate the patient by giving them a concrete improvement metric while also providing valuable data for clinical decision making.

Table 1.1: Comparison of common chelators¹

Property	Deferoxamine	Deferiprone	Deferasirox
Route	Subcutaneous, IV	Oral	Oral suspension
Usual dose	20-40 mg/kg/day over 8-24 hours, 5 days/week	3 doses/day, 25-33 mg/kg	20-40 mg/kg/day
Excretion	Urinary, faecal	Mainly urinary 3-4 hours	Faecal 8-16 hours
Half-life	20-30 min	Gastrointestinal Agranulocytosis/ neutropenia Arthralgia Elevated liver enzymes	Gastrointestinal Rash Rise in creatinine Proteinuria Ophthalmological Auditory Elevated liver enzymes
Adverse effects	Local skin reactions Ophthalmological Auditory Allergic reactions Growth retardation Bone abnormalities At high doses: - Pulmonary - Neurological		
Challenges	Adherence due to parenteral administration; need for yearly ophthalmology and audiometric examination	Need for weekly blood count monitoring; not commercially available in all countries; limited data in children; variable efficacy in removal of hepatic iron	Need for weekly blood count monitoring; not commercially available in all countries; limited data in children; variable efficacy in removal of hepatic iron
Status	Licensed	Licensed in USA and Europe	Licensed in USA and Europe
Indications	Treatment of chronic iron overload due to transfusion-dependent anaemias (and for treatment of acute iron intoxication)	Treatment of iron overload in thalassemia major when DFO is contraindicated or inadequate.	In USA licensed for the treatment of chronic iron overload due to transfusion-dependent anaemias in individuals aged 2 years and older. In Europe licensed for the treatment of transfusional iron overload in beta-thalassaemia major patients, 6 years and older, and approved for use when DFO is inadequate or contraindicated in patients with other anaemias, patients 2-5 years, and patients with non-transfusion-dependent thalassaemia
Age considerations	Not recommended for children <3 years with low transfusional burden	Limited or no data on children aged <6-10 years	Studied in children as young as 2 years old

1.1.4 Diagnosis and Monitoring of Iron Overload

Due to the importance of accurately assessing tissue iron quantity, a number of quantitative tests were developed, each with widely varying invasiveness, measurement variability, sensitivity, and cost. Further, the resolution of these tests ranges from providing total-body iron to organ-specific estimates.

Biopsy

Early attempts to quantify liver iron used needle biopsy to assess hepatic iron stores. This outpatient procedure, performed about once per year in cases of chronic iron overload, requires a small sample of liver to be removed and desiccated; the resulting mass of iron versus sample weight is reported. Because the spatial distribution of iron is known to vary based on the cause of iron overload and even the primary indication for transfusion therapy, light microscopy is sometimes performed when the cellular distribution of iron is relevant to treatment²⁰. However, biopsy presents a variety of challenges, including risk of complications²¹ and sampling error^{22,23,24}. Iron quantitation in the heart is possible by biopsy but increases complication rates when used over a prolonged period²⁵. Furthermore, cardiac iron is heterogeneously distributed and biopsies can only be safely obtained from the right ventricular septal surface. Pancreas iron quantitation is also crucial in transfusion-dependent patients and cannot be safely accomplished with biopsy due to its high complication and mortality rate²⁶. Despite the noted measurement variability, biopsy is still often cited as the reference standard for liver iron quantitation²⁷.

Serum Ferritin

Serum ferritin is a measure of the ferritin concentration in a blood sample obtained by phlebotomy. Because ferritin can store a large quantity of iron and is critical to enabling iron transport by ferritin, may attempts have been made to correlate its presence with total body iron. Overall, serum ferritin concentration does correlate with liver iron^{28,29}. However, most studies demonstrate significant variability between patients, repeat measurements, and disease populations^{30,21}. Further, serum ferritin is discordant with LIC in certain studies, especially in transfused populations³¹. Together, these limitations cause serum ferritin to be an undesirable metric of iron in transfusion-dependent patients.

CT

Computed tomography (CT) is an X-ray imaging technique that can generate cross-sectional images of anatomy. The signal intensity demonstrated by each tissue is proportional to its X-ray absorption properties. Liver iron content has been demonstrated to increase X-ray absorption compared to normal tissue with both single and dual energy CT^{32,33,34}. In addition to producing tighter correlation to liver iron than serum ferritin, CT is widely available due to its use in a variety of other clinical imaging contexts. Its speed and low cost make it attractive for iron quantitation. However, CT suffers from poor sensitivity to low iron loads³⁵ and there is little human validation data available³⁶. Further, when fat is present in the liver, a condition often occurring secondary to chronic iron overload, the inverse correlation between x-ray signal attenuation and fat lead to underestimates tissue iron³⁷. CT also exposes patients to unnecessary radiation increasing lifetime cancer risk, especially in pediatric populations³⁸.

SQUID

Superconducting quantum interference device (SQUID) is a device that uses radio frequency (RF) or direct current (DC) signals to make extremely sensitive measurements of magnetic fields. Due to iron's influence on magnetic fields, SQUID can detect its presence in tissues. SQUID is the earliest approach to assessing tissue iron burden³⁹ that is completely non-invasive. Although SQUID is highly sensitive to iron, it suffers from a number of impediments. The combination of its high installation cost and relatively limited utility outside of iron content assessment in the liver and spleen have limited the availability of SQUID significantly⁴⁰. At the time of writing, only three SQUID devices are operational in the US.

MRI

MRI is an imaging technique that forms cross-sectional images by applying static and time-varying magnetic fields to subjects, relying on a Fourier-based mathematical transform to create images from received signal. Due to MRI's dependence on magnetic fields, it showed promise for iron quantitation early as 1984 based on iron's magnetic effects similar to SQUID^{41,42,43}. MRI, unlike SQUID, received wide-spread adoption due to its imaging capabilities, which provided an unparalleled set of capabilities and flexibility that permitted the emphasis of certain tissues based on the scan parameters. This made MRI a promising candidate for a completely non-invasive approach to gathering sensitive, accurate iron measurement in a variety of tissues. Although early attempts at iron quantitation failed, MRI has become the clinical standard in iron quantitation due to its superior inter-measurement variability and noninvasiveness.

1.2 Magnetic Resonance and Iron

Magnetic resonance imaging is a complex technology that has strong applications throughout medicine. Due to iron's magnetic properties, researchers have tried to leverage its effects on MRI signals since the late 1980s. Nonetheless, biopsy remained the dominant tissue iron detection method into the early 2000s. In the early-to-mid 2000s, a number of techniques were developed using 1.5T MRI scanners that allowed the successful quantification of tissue iron. Studies demonstrated success quantifying tissue iron in the liver, heart, pancreas, spleen, brain, and bone marrow^{4,7,44,45,46}. Compared to biopsy and serum ferritin measurements, MRI demonstrates tighter measurement variability of about 3-8%. Further, MRI demonstrates strong correlation with iron even at low tissue iron content while its dynamic range reaches up to 40^{mg/g}, providing sufficient information to prescribe chelators accurately and monitor their effectiveness. As methods to suppress or quantify fat were developed, MRI became a more complete quantitative solution than CT. Due to its clear superiority compared to other available diagnostic techniques, MRI supplanted biopsy as the clinical standard for iron quantitation in all organs and obviated the need for the other quantitative modalities.

Despite MRI's success, a number of limitations in existing scan techniques remain. First, the maximum tissue iron content that can be quantified at 1.5T is presently limited to approximately 40^{mg/g}. Clinical iron loads of at least 60^{mg/g} have been identified through histology, suggesting that MRI may fail to correctly estimate iron in an important subset of patients. Above an LIC of 20^{mg/g}, the precise iron load does not change the clinical treatment. However, quantitation that is safe for repeat use still provides value in assessing chelation efficacy — which is dependent on patient, tissue, and chelator — and provides important motivation for patients to continue with chelation therapy in spite of uncomfortable

side-effects. A second problem arose as MRI technology developed higher field strength magnets such as 3T. Though higher field magnets improve many aspects of clinical imaging, the effects of iron on the signal are directly proportional to the field strength. Increasing field strength from 1.5T to 3T leads to a 50% reduction in the dynamic range for iron quantitation in an otherwise identical test. Other problems, such as increased spatial intensity variation in images, have further confounded iron quantitation at 3T.

Understanding the underlying principles of MRI allows us to acquire and process signals in a way that tell us about iron even though it cannot be directly measured with MRI, allowing us to overcome the current limitations in imaging technology.

1.2.1 Nuclear Magnetic Resonance

Nuclear magnetic resonance (NMR) is an atomic phenomenon that forms the basis for MRI, though “nuclear” and “atomic” simply refer to the nucleus of an atom rather than ionizing radiation. Atoms with an odd number of protons or neutrons demonstrate NMR when an external magnetic field is applied to them. Quantum mechanics describes such atoms as having a non-zero quantum spin states, leading to these atomic nuclei being called “spins.” The interaction between spins and the magnetic field ultimately allow a signal to be generated from them.

Magnetization and Precession

In one sense, spins are like tiny bar magnets because they align with external using magnetic fields. When a powerful magnetic field, called the main field or B_0 , is applied to a sample containing spins, they align with the magnetic field. This means that the individual magnetic vector of each of the spins sum together

to form a magnetic vector pointing parallel to B_0 . This forms the basis for a coordinate system that defines the spatial orientation of the magnetic vectors. The two primary coordinate systems used in NMR, the lab frame and the rotating frame, are both 3-dimensional Cartesian coordinate systems whose Z-axis is parallel to the B_0 . Known as the longitudinal axis, the Z axis is orthogonal to a plane known as the transverse plane. The transverse plane contains orthogonal X and Y axes, which remain fixed in physical space in the lab frame. The axes X' and Y' also lie in the transverse plane but rotate at the same frequency as the spins in the rotating frame. At equilibrium, there is no net magnetization pointing in the transverse plane, only along the longitudinal axis.

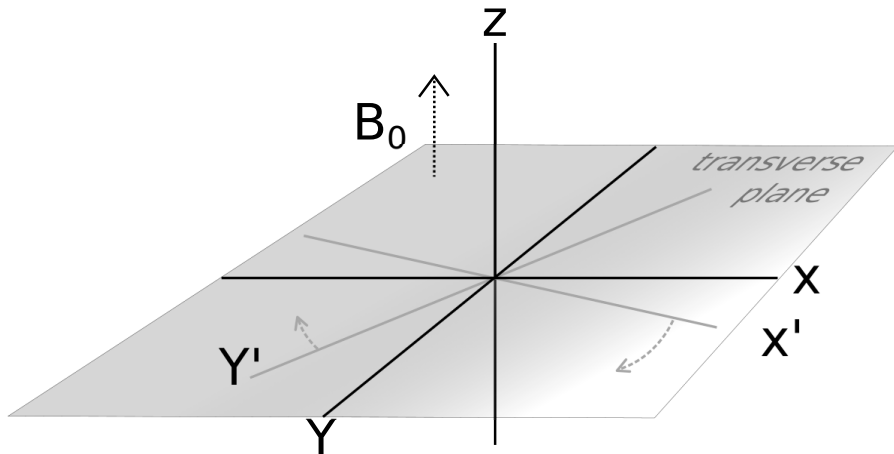


Figure 1.2: Demonstration of lab and rotating frames used in MRI

In addition to aligning with this axis, the spins demonstrate a second behavior called precession that is unlike a standard bar magnet. The magnetic vectors of the nuclei precess, or spin, around the main field in a counter-clockwise or “left-handed” rotation. The angular velocity of this rotation is specific to the type of nucleus and is proportional to the field strength. The frequency of precession can be determined with the gyromagnetic ratio, which is equal to 42.58 MHz/T for hydrogen;

Element	Spin	Gyromagnetic Ratio (MHz/T)
¹ H	$\frac{1}{2}$	42.58
² H	1	6.54
³ He	$\frac{1}{2}$	-32.43
¹³ C	$\frac{1}{2}$	10.71
¹⁴ N	1	-4.32
¹⁹ F	$\frac{1}{2}$	40.05
²³ Na	$\frac{3}{2}$	11.26
³¹ P	$\frac{1}{2}$	17.24

Table 1.2: Common spin nuclci

the gyromagnetic ratios of other relatively common nuclei are summarized in table 1.2.1. Although precession is taking place constantly, no signal can be acquired from the longitudinal magnetization. Until the spins are perturbed by an external force, their net magnetization will remain in pointed along the longitudinal axis.

The precession of spins around a magnetic field is described by the Bloch equation^{47,48}:

$$\frac{\overline{\partial M}}{dt} = \gamma(\overline{M(t)} \times \overline{B(t)}) \quad (1.1)$$

which demonstrates that the rotation of the magnetization is dependent on magnetic fields orthogonal to it. The change in the magnetization is non-zero only when \overline{M} and the external \overline{B} field are not parallel.

1.2.2 Excitation and Acquisition

The Bloch equation demonstrates a key relationship between proton magnetization and an external, applied magnetic field that ultimately allows for the generation of images. If the B field can be manipulated to include a component in the transverse plane, the spins will begin to rotate around it, effectively turning the net magnetization vector onto the transverse plane. This is accomplished using

electromagnetic pulses oscillating at the Larmor frequency (γ in equation 1.1) of the protons. This frequency is proportional to field strength, equal to 63.87 MHz at 1.5T and 127.7 MHz at 3T, placing the electromagnetic waves in the RF spectrum. RF pulses are applied in the transverse plane rather than along the longitudinal axis, creating an axis of rotation that is orthogonal to the magnetization of the spins. As the spins rotate about the new magnetization vector, a portion of the net magnetization will move from the longitudinal axis into the transverse plane — this process is called excitation.

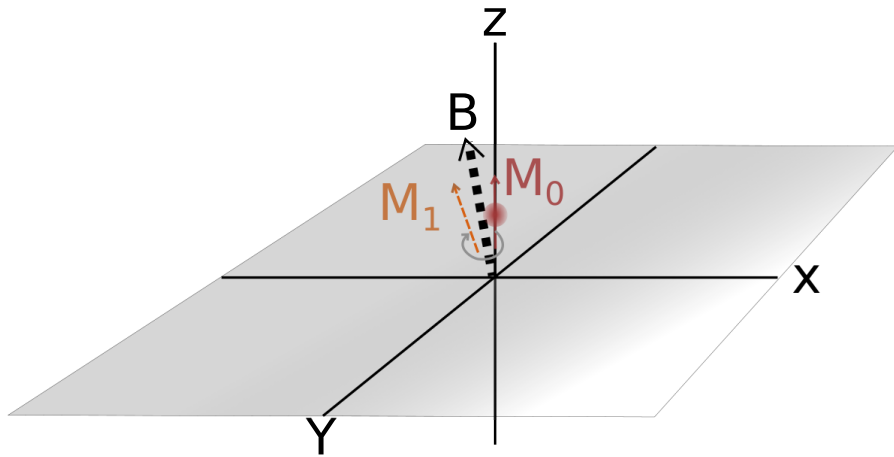


Figure 1.3: Demonstration of precession about a B field with a non-zero transverse RF component

The strength and duration of the RF pulse determines the amount of excitation achieved. Because the magnetization is a vector and because excitation is a disturbance from equilibrium, the excitation is normally measured with an angle relative to the B_0 field. The flip angle demonstrates how far the magnetic vector has rotated, so a 90° flip angle would move the entire magnetization vector onto the transverse plane while a 180° flip angle would invert the magnetization entirely, making it point anti-parallel to B_0 . Assuming an arbitrary excitation flip angle of

Θ , the resulting transverse (M_{xy}) and longitudinal (M_z) magnetization magnitudes immediately after excitation ($t = 0$ seconds) will be:

$$\begin{aligned} M_{xy}(0) &= M_{z,eq}\cos(\Theta) \\ M_z(0) &= M_{z,eq}\sin(\Theta) \end{aligned} \quad (1.2)$$

Once the spins are excited, they will continue rotating around the B_0 field according to the Bloch equation. As the magnetization rotates, it will create a sinusoidally-varying magnetic flux, a time-varying magnetic field, in the lab frame which can induce a current in a properly oriented wire loop. By recording this current, we can determine the magnitude of the spins' magnetization. If we can add more coils orthogonal to the transverse plane, we can gather information about phase, or the angle of the magnetization.

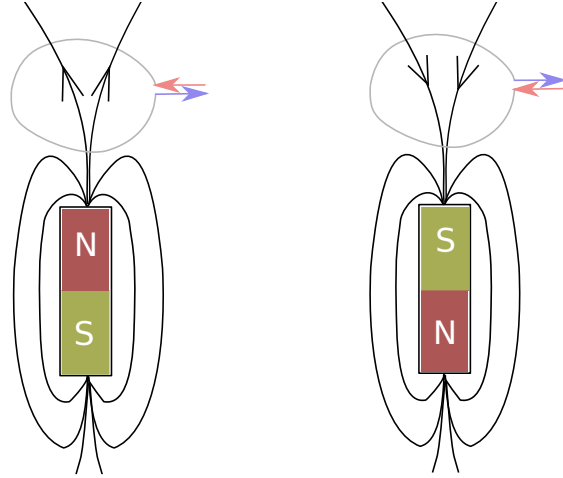


Figure 1.4: Demonstration of current induced in a coil by time-varying magnetic fields

Relaxation

Although the spins can be pushed into the transverse plane with RF pulses, the net magnetization will eventually reorient to the original equilibrium state, returning to parallel with the B_0 field. In a process called relaxation. This process involves the loss of transverse magnetization as well as the increase in longitudinal magnetization. Transverse decay and longitudinal recovery are normally modeled as exponential processes as follows:

$$\begin{aligned} M_{xy}(t) &= M_{xy}(0)e^{-t/T_2} \\ M_z(t) &= M_{z,eq} - M_z(0)e^{-t/T_1} \end{aligned} \quad (1.3)$$

The processes are described by two separate time constants, T_1 and T_2 . T_1 specifies how long longitudinal recovery to 63.9% ($1 - e^{-1}$) takes to occur while T_2 describes how quickly transverse signal falls to 36.7% (e^{-1}) of its original value. Because transverse decay must happen no slower than longitudinal recovery, T_1 is always greater than T_2 . However, it is possible to lose transverse magnetization without experiencing longitudinal recovery at the same rate, so T_2 is often significantly smaller than T_1 .

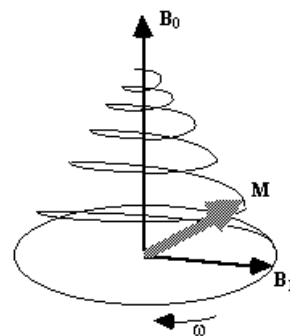


Figure 1.5: Example of T_1 and T_2 relaxation³

The complete Bloch equation accounts for T_1 and T_2 relaxation as follows:

$$\frac{\partial M}{\partial t} = \gamma(M(t) \times B(t)) - \frac{M_x(t)\hat{i} + M_y(t)\hat{j}}{T_2} - \frac{(M_z(t) - M_0)\hat{k}}{T_1} \quad (1.4)$$

Although relaxation that is intrinsic to a given nucleus in a certain magnetic field is described by T_1 and T_2 , many factors influence the NMR signal. Spatial magnetic heterogeneity leads to an apparent increase in the transverse decay rate. This apparent decay following a time constant called T_2^* . It is common to write T_2^* as it relates to T_2 :

$$\frac{1}{T_2^*} = \frac{1}{T_2} + \frac{1}{T'_2} \quad (1.5)$$

where the decay component, T'_2 , introduced by field inhomogeneities is greater than 0. Equation 1.5 demonstrates that T_2^* is never larger than T_2 and converges to T_2 when the field is perfectly homogeneous. Molecular motion such as diffusion interacts with magnetic field disturbances to accelerate T_2 decay as well.

When a sample is excited, it will produce a free induction decay (FID), or an observable, decaying electromagnetic signal described by the Bloch equations. This FID will appear to decay with T_2^* rather than T_2 unless the magnetic environment is perfectly homogeneous. The spins rotate out of phase with each other, causing the vector sum of their magnetizations to fall. However, the transverse magnetization, which is merely “hidden”, still decays with T_2 .

When working with iron, it is convenient to consider quantities that are proportional to iron rather than inversely proportional. Because T_2 and T_2^* fall with iron, their reciprocals grows. These quantities are called “relaxation rates” and are defined:

$$R_2 = \frac{1}{T_2} \quad (1.6)$$

$$R_2^* = \frac{1}{T_2^*} \quad (1.7)$$

For most purposes, referring to “T” or “R” decay is functionally equivalent. However, some nuances appear. First, R_2^* was found to be linearly related to iron quantity, making it a desirable diagnostic metric due to its strong dependence on iron⁴. R_2 is also related to iron, but loses sensitivity as the iron load increases⁷. Although this makes it a less effective metric for total iron quantitation, it can uncover tissue iron distribution that cannot be differentiated with R_2^* alone⁴⁹.

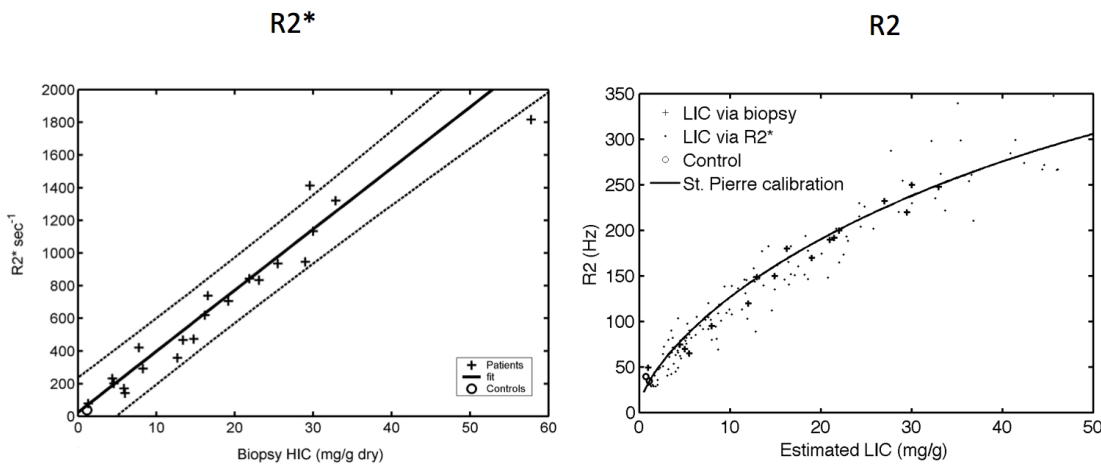


Figure 1.6: Demonstration of R_2 and R_2^* decay with respect to tissue iron content.
Reproduced from Wood et al.⁴

1.2.3 Proton Imaging

Although any nucleus with a non-zero spin state demonstrates NMR, hydrogen proton imaging, or the imaging of ^1H is almost exclusively used in medicine due to the high proportion of hydrogen atoms in the human body, bound mostly to water or fat. In addition to the abundance of hydrogen in the body, practical matters such as hardware equipment design limit most MRI systems to ^1H . The

terms “proton,” “spin,” and “nucleus” henceforth refer to ^1H atoms in particular, though the general principles apply to imaging other nuclei.

MRIs are like large NMR spectrometers with a few modifications. Shaped like a car-sized doughnut, the center of the magnet is called the bore. The bore, commonly on the order of 60 cm in diameter, is large enough to fit a person but is kept as small as possible to keep the magnetic field inside very accurate. Although other magnetic configurations and field strengths exist, 1.5T and 3T toroid magnets are most common in clinical settings. In fact, the field in the MRI only varies by 1 part per million (ppm), or 0.000001%. The field needs to be precise to enable the techniques that lead to image formation.

1.2.4 Spatial Encoding and Selective Excitation

In order to create images rather than whole-body NMR measurements, the signal must be encoded with position and transformed from an acquired set of waveforms into an image. The encoding of spatial information simply extends the relationship between magnetic field strength and Larmor frequency by giving different spins slightly different resonant frequencies relative to their physical position. This is accomplished using gradients, time-varying magnetic fields that linearly relate their strength to a position along the X, Y, or Z axis in the lab frame. Spins at different locations can be identified by their slightly different resonant frequencies, which can be exploited to ensure that only certain portions of tissue produce signal and that the received signal can be traced back to a particular location.

After the application of appropriately-designed gradient fields, the encoded data can then be decoded using Fourier transform. The Fourier transform is a deceptively simple mathematical concept with major ramifications. A transform is based on the idea that a signal can be represented in a number of ways, much

like how we can describe all colors as combinations of a few colors. For example, purple is red plus blue. Every shade of purple can be obtained by varying the ratio of red and blue. Similarly, a Fourier transform converts an arbitrary, often apparently complicated or random, function into a simple sum of sine waves. That means that a function $f(x)$ can be written like this:

$$f(x) = \sum_{n=1}^{\infty} F(n)(\cos \Theta - i \sin \Theta) = \sum_{n=1}^{\infty} F(n)e^{-i\Theta} \quad (1.8)$$

$$\Theta = 2\pi(\frac{n}{T})x \quad (1.9)$$

where $F(n)$ is a set of weight coefficients for each n th out of a set of N total samples, Θ is an oscillatory frequency in Hz, $f(x)$ represents an infinitely long signal in the time domain, and T is the length along a time-domain sampling dimension. By adding higher frequency waves, the approximation gets better.

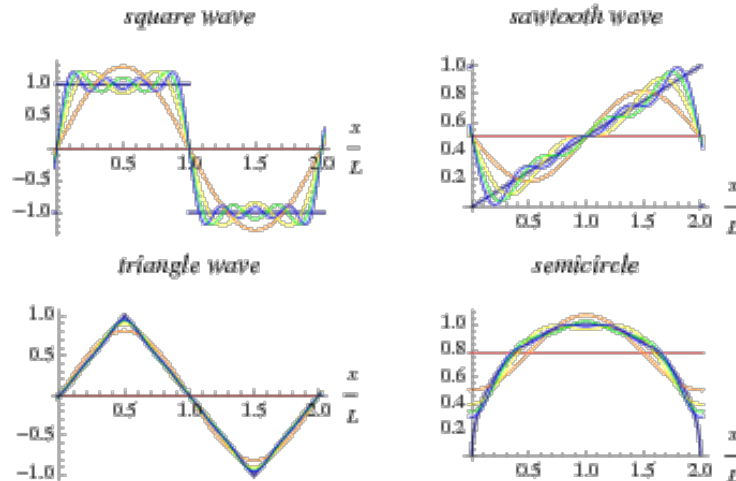


Figure 1.7: Illustration of approximations of different waveforms with Fourier series. As the number of Fourier coefficients increases, the sum of sine waves becomes a better fit for the waveform.⁵

Moving from discrete coefficients into the continuous time domain, the integral form of the Fourier transform is as follows:

$$F(\xi) = \int_{-\infty}^{\infty} f(x)e^{-2\pi i x \xi} dx \quad (1.10)$$

with the inverse transform being:

$$f(x) = \int_{-\infty}^{\infty} F(\xi)e^{2\pi i x \xi} d\xi \quad (1.11)$$

Thus, gradient fields relate a spin's precession frequency to a point in space and the Fourier transform relates frequency and time. Using these principles, we can create a set of equations with only one variable. We can apply RF pulses or sample signals in the *time* domain and use a combination of gradients and the Fourier transform to gain *spatial* knowledge about the signal. For excitation, this means that we can excite only certain spins by shaping our RF pulse. Consider the following two pulses and their respective Fourier transforms:

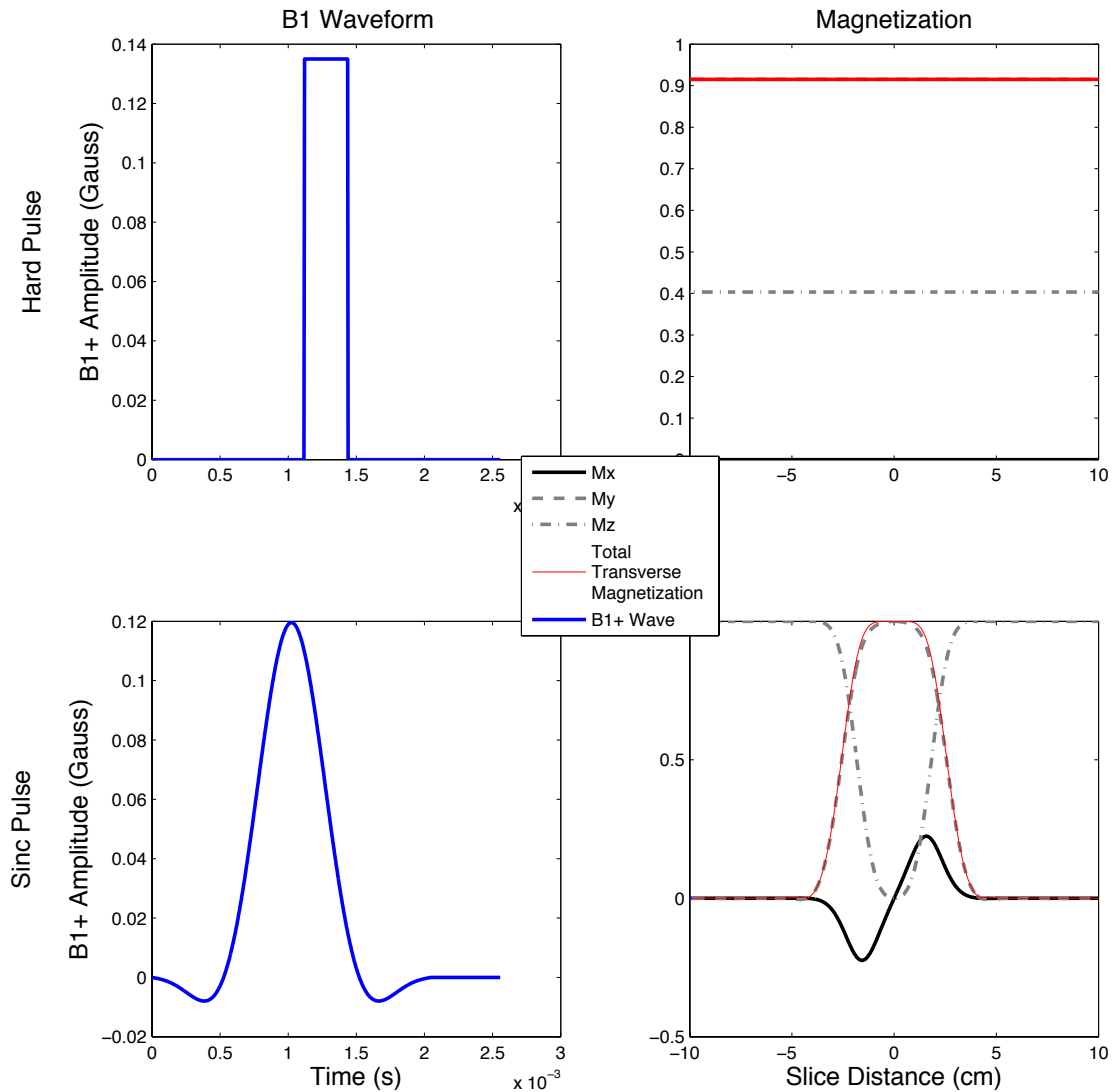


Figure 1.8: Illustration of slice selection producing transverse magnetization in a single slice. The hard pulse with no slice selection gradient produces uniform excitation in the sensitive area of the coil while the sinc pulse with a z-gradient produces excitation of only part of the object.

The hard pulse has a nearly constant effect across all frequencies while the sinc ($\sin(x)/x$) pulse only operates over a central set of frequencies. This means that if a magnetic gradient is active, only spins in the region of the “bandwidth” will be

excited when a sinc pulse is used and the resulting signal comes only from those spins.

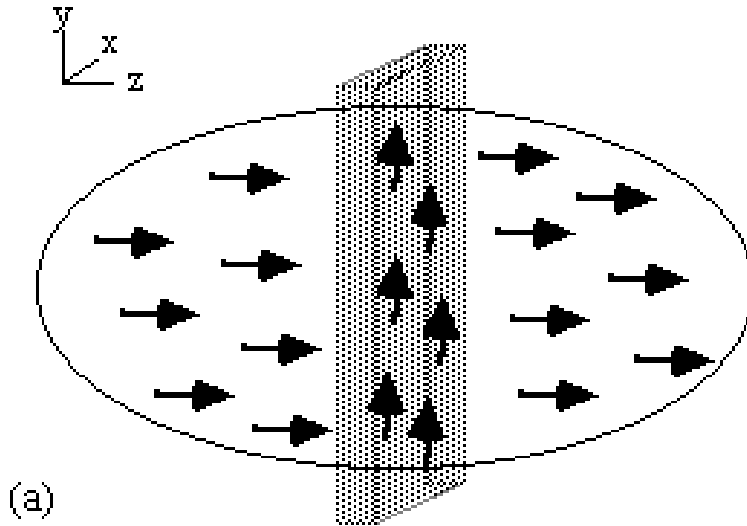


Figure 1.9: Illustration of slice selection producing transverse magnetization in a single slice³

Similarly, if we have a gradient active along the X direction during signal reception, we apply a spatial-spectral constraint to our signal. More simply, the signal's position can be known if its frequency can be known. It results in a signal, $s(t_x)$, that has the following mathematical form:

$$s(t_x) = \int_x m(x)e^{-i\gamma G_x t_x} dx \quad (1.12)$$

where $m(x)$ is the projection of the object onto the x axis, G_x is the gradient amplitude, x is distance along the X-axis, and t_x is time. Comparing equation 1.12 to equation 1.10 for a Fourier transform, we see that they are identical if $\gamma G_x t_x \equiv 2\pi i \xi$ and $m(x, y) \equiv f(x)$. By using a gradient amplitude G_x and duration t_x , we can encode signal from the magnetization in a way that can be decoded by

a Fourier transform: to get the image back, we just compute the inverse Fourier transform of our signal. By adding another gradient, we can expose the Y-axis as well rather than projecting the object onto the X axis, giving us a signal, $s(t_x, t_y)$ of the form:

$$s(t_x, t_y) = \int_x \int_y m(x) e^{-i\gamma G_x t_x x} e^{-i\gamma G_y t_y y} dy dx \quad (1.13)$$

where G_y is the Y-gradient amplitude and t_y is the length the Y gradient is turned on. After acquiring signal for all relevant combinations of t_x and t_y , we can simply invert the Fourier transform along t_x and along t_y to give us an image in x and y .

1.2.5 Pulse Sequences

When RF pulses, gradients, and acquisition parameters are combined to generate images, the combination is called a pulse sequence. Though many pulse sequences exist, they share some common features. For iron quantitation, the most important parameter in a pulse sequence is echo time, or TE. An echo occurs when spins rephase after losing transverse magnetization, leading to a sudden increase in signal. This is true for all classes of pulse sequences but the precise meaning of echo time changes depending on the pulse sequence. Two types of sequences, spin echo and gradient echo, are useful in iron overload because they demonstrate different contrast mechanisms.

Gradient Echo

A gradient echo is the simplest type of pulse sequence, requiring only a single RF pulse and encoding gradients to make an image. Because signal decays away, gradient echoes actually accelerate the decay and then reverse the decay using a gradient. For this reason, gradient echo signals decay with T_2^* . Many gradient

echo sequences use a “Cartesian” encoding scheme, which acquires lines of k-space sequentially. They are popular due to the ease of image reconstruction but suffer from echo time limitations related to gradient strength. Other sampling schemes, such as center-out radial, can achieve shorter TEs but increase the complexity of reconstruction. Further, “multi-echo” gradient echoes can play a series of gradients that generate multiple echoes for a single excitation, with each echo showing more T_2^* decay than the preceding echo.

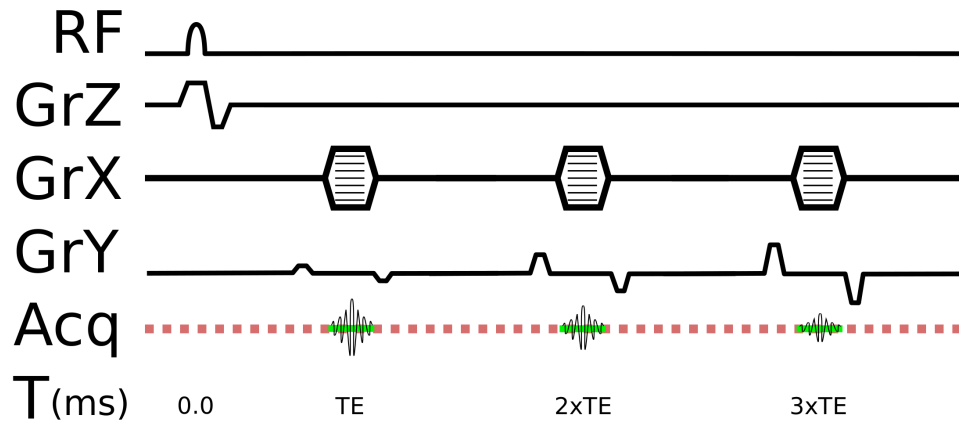


Figure 1.10: Example of a common multiecho gradient echo pulse sequence.

Spin Echo

A spin echo is like a gradient echo, but with a second RF pulse called an inversion pulse that is played half-way between the excitation pulse and the intended TE. The inversion causes the phase accrued due to magnetic inhomogeneities to be reversed, so the natural rotation of the spins rewinds the phase accrual. This means that spin echoes can be formed without the application of a gradient, though the readout gradient is necessary for spatial encoding. By naturally reversing the effects of magnetic inhomogeneities, spin echo signals decay with T_2 rather than T_2^* . Just as gradient echoes can create multiple echoes for a single excitation, spin

echoes can play an “RF train,” or a series of RF pulses, to generate many echoes with compounding T_2 decay.

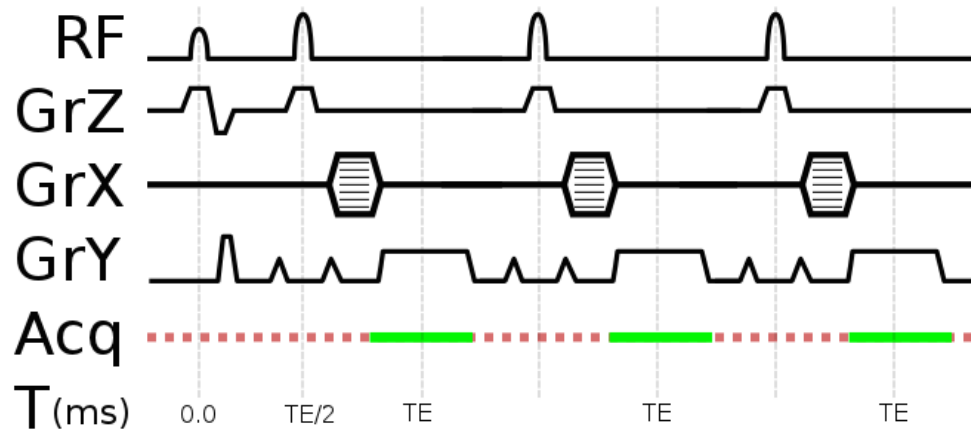


Figure 1.11: Example of a common multiecho spin echo sequence.

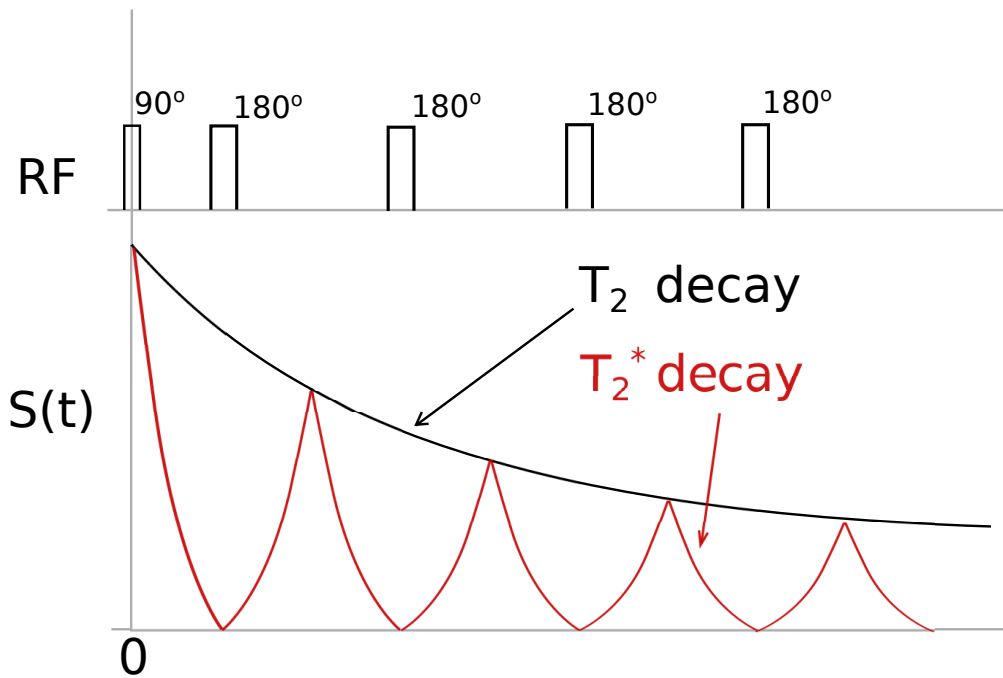


Figure 1.12: Illustration of a train of 180° pulses generating multiple spin echoes that decay with T_2

1.2.6 Interactions with Iron

Iron demonstrates a profound effect on MR signals. Its paramagnetic behavior causes the local magnetic field to be amplified, leading to more rapid T_2^* and T_2 decay. In practice, tissues with even mild iron loading can appear dark or completely black, reducing the signal-to-noise ratio, SNR, to nearly 0. But the effect is predictable. As iron load increases, T_2 and T_2^* decrease.

In the absence of noise, the rapid decay caused by iron would be easy to estimate using common curve fitting techniques. However, thermal noise causes unavoidable error in the sampled signal. As the signal nears zero, the noise complicates the iron estimates. What's more, the complex signal is often reduced to its absolute value for analysis purposes, leads a more complicated relationship between noise and signal. This means that both the decay rate and the SNR are iron dependent, which makes accurate fitting a challenge.

The presence of iron leads to increased dephasing along with the rapid decay rates. Such unanticipated dephasing can cause phase-based quantitative techniques to fail because the assumption of 1-parts-per-million (PPM) B_0 field homogeneity is no longer true. In a spectroscopic sense, the rapid decay of the water protons cause the water peak to spread, enveloping fat peaks, making accurate fat quantitation challenging.

1.3 Monte-Carlo Simulation

Although magnetic resonance imaging is an extremely popular research technique, conducting studies can be expensive and time-consuming. In response to these limitations, many attempts have been made to simulate MRI signals computationally to reduce protocol development time and magnet use. In the context

of iron, such a simulation must perform a series of tasks to accurately capture the nuances of physiologic iron: simulate liver’s cellular tissue structure, simulate iron distribution within the tissue, calculate the magnetic effects of the iron, track simulated proton paths as water diffuses in the tissue, excite the simulated protons, and apply the iron-based magnetic disturbances to the protons. Hoping to extend simulations to iron imaging, Nilesh Ghugre developed a modular, iron-oriented simulation framework from tissue histology to accomplish these tasks⁶. The framework generated signals demonstrating R_2 - and R_2^* -LIC estimates with the same variability seen in patient populations, effectively allowing nearly-unlimited virtual patient studies. To accomplish this life-like variability, Ghugre used light microscopy of tissue histology to estimate Gamma probability distributions describing the spatial statistical properties of iron particles in the liver.

Tissue is modeled in the simulation by an 80 μm cube of liver tissue containing 64 cuboidal hepatocytes measuring 20 μm and 18 cylindrical sinusoidal regions measuring 10 μm diameter and 20 μm height, ignoring portal structures. The model includes the ability to distribute iron-containing spheres with varying size, frequency, and spacing in the hepatocytes and/or sinusoid based on the probabilistic Gamma distributions for each iron overload phenotype. The tissue model is complete with boundaries to represent cell membranes, which is necessary to restrict diffusion. Within the tissue model, iron stores are placed in the tissue according to gamma probability distributions, a two-parameter function that is commonly used to model probability events. From the sphere placements, a spatial magnetic disturbance map can be computed as follows:

$$\frac{\Delta B(r, \Theta)}{B_0} = \frac{1}{3} \chi_L \left(\frac{R}{r}\right)^3 (3 \cos^2 \Theta - 1) \quad (1.14)$$

where B_0 is the main magnetic field, R is sphere radius, r is the sphere's radial distance from the center of the sampling volume, Θ is the azimuthal angle relative to the magnetic axis, χ_L is the magnetic susceptibility $\frac{(HIC/WDR)*\chi_F}{v}$ where v is the sphere volume fraction, HIC is the tissue iron content and WDR is the tissue wet to dry weight ratio (set to 4.1⁵⁰).

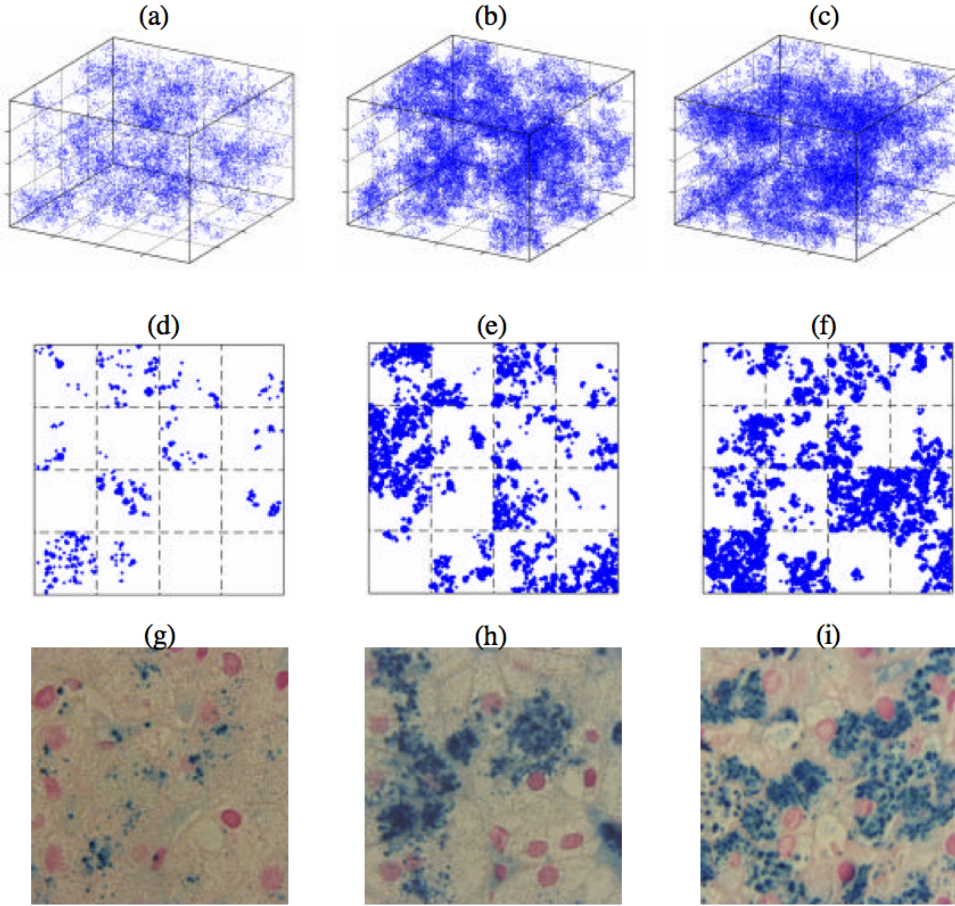


Figure 1.13: A demonstration of simulated tissue in 3 dimensions (panels a,b,c) for LIC values of 4.4, 30, and 57.8 mg/g, respectively. Panels d-f demonstrate 2D projections of 4 μm slices of the 3D geometries; panels g-i show histology samples that demonstrate the similarity with physiologic data that the simulation can achieve. Reproduced from the thesis of Nilesh Ghugre.⁶

Simulating signal from water protons in a heterogeneous magnetic environment requires the ability generate realistic motion so that the magnetic disturbances from iron can be experienced. This is accomplished using a Monte Carlo simulation, which uses repeated random sampling of probabilistic functions that describe the motion of water molecules. In this framework, water motion can be free or restricted to cell boundaries. Proton paths were computed by sampling a proton's displacement change at each timestep from a Gaussian distribution. The mean absolute displacement, σ , is given by:

$$\sigma = \sqrt{2D\delta} \quad (1.15)$$

where D is the diffusion coefficient ($0.76 \text{ nm}^2/\text{ms}$ for human liver⁵¹) and δ is the simulation time step ($0.5 \mu\text{s}$). At each timestep, the next position is randomly selected; cell boundaries are tested according to the chosen rules before accepting a new position. Once the random walk of the proton is known, the magnetic disturbances can be calculated from the previously-generated field map.

MR signal can be estimated in a variety of ways. The first revisions of the simulation assumed perfect RF pulses, achieving exact, instantaneous excitation — perfect inversion was simulated by reversing the accrued phase for each proton at $T_{E/2}$. The behavior of the resulting signal showed strong agreement with experimental data.

Despite the strong correlation between simulated and acquired data, the framework did not allow for certain phenomenon such as pulse bandwidth to be modeled. Further, the amplitude effects and non-idealities in RF transmit systems could not be simulated using phase-based signal calculations alone. To create a more complete simulation, a 3D Bloch simulator was added to the framework,

allowing for the computation of a proton's magnetization vector in X, Y, and Z. This also allowed RF pulse waveforms to be used for excitation and allowed for pulse non-idealities that occur due to imperfect flip angles. This approach added critical functionality to the simulation framework for addressing many practical questions.

1.4 Specific Aims & Significance

Though 1.5T MRI is now the clinical standard for iron overload diagnosis, a variety of challenges have arisen. Most notably, the extreme loss of dynamic measurement range of liver iron 3T is hindering iron overload quantitation. It is estimated that over 50% of new MRI installations are 3T, leaving some imaging centers without a 1.5T magnet for diagnosis and monitoring of iron overload. This research focused on one primary unifying goal: make 3T MRI a reliable diagnostic tool for all clinically-relevant tissue iron loads. To accomplish this goal, a variety of practical and theoretical challenges needed to be overcome relating to lack of human validation, pulse sequence limitations, and increasing non-idealities at 3T. The results will help to remove barriers to the use of 3T MRI while providing valuable insight into resolving limitations at 1.5T and permitting the use of even higher-field magnets should they become available clinically.

1.4.1 Aim 1 - Translate R_2^* Imaging from 1.5T to 3T

Develop and implement imaging protocols and quantitative evaluation techniques to enable iron quantitation at 3T.

Hypothesis 1a) Clinical R_2^* estimates will exhibit field-dependent relaxation enhancement in humans.

Hypothesis 1b) Ultra-short echo time imaging will extend the dynamic range of LIC estimates at 3T further than Cartesian gradient echo can achieve.

Hypothesis 1c) Relaxometry of ultra-fast decay species can be improved with information from a patient's iron-free tissues without the need for additional imaging series.

1.4.2 Aim 2 - Assess Non-Idealities at 3T

Understand and correct for known imaging confounds that are present or more pronounced at 3T.

Hypothesis 2a) B_1^+ inhomogeneity must be corrected at 3T when spin echo imaging is used for R_2 quantitation.

Hypothesis 2b) B_1^+ inhomogeneity will not appreciably affect R_2^* quantitation.

1.4.3 Aim 3 - Develop and Test Novel MR-based Iron Quantitation Techniques

Determine the feasibility of using novel pulse sequences to robustly perform iron quantitation.

Hypothesis 3a) A spectroscopic approach using chemical shift imaging can simultaneously quantify R_2 and R_2^* with high robustness.

Hypothesis 3b) Short TE spin echo sequences can quantify R_2 at 3T.

1.5 Outline

Chapter 2 demonstrates the benefit of fitting CPMG spin echo data with a proton density estimator to improve sensitivity to tissue iron content. This retrospective study showed that using only data derived from within an imaging series, the relationship between R_2 and LIC becomes stronger than estimates made without the constraint. This study validates this effect by replicating another center's imaging study parameters and demonstrating nearly identical relationships between LIC and unconstrained or constrained R_2 .

Chapter 3 examines the relationship between relaxation estimates made with 1.5T and 3T MRI systems. This study uses simulation data to demonstrate a closed-form solution for converting liver R_2 and R_2^* estimates acquired at an arbitrary field strength to any other field strength. It also presents human imaging data from 1.5T and 3T to validate the predictions of the model.

Chapter 4 assesses the effect of B_1^+ inhomogeneity, a common imaging confounder at 3T, on R_2 and R_2^* estimates. Simulation results demonstrate the importance of correcting single spin echo and CPMG-based R_2 estimates in the presence of B_1^+ inhomogeneity. Human imaging results demonstrate the magnitude of B_1^+ inhomogeneity in a patient population at both 1.5T and 3T. Correction at 1.5T was found to be beneficial while correction at 3T was critical.

Chapter 5 demonstrates a new imaging protocol to assess liver iron at 3T using ultra-short echo time imaging in conjunction with existing clinical processing pipelines. A 23-patient study found that UTE imaging could assess moderate-to-high liver iron with similar variability seen with clinical techniques at 1.5T. Comparison by Bland-Altman and regression analysis are provided. Further, the effects of tissue fat are assessed for each imaging protocol to explain disagreement between clinical LIC estimates and UTE estimates.

Chapter 6 describes a novel approach to iron imaging through a modified chemical shift imaging spectroscopy sequence. Through the application of custom RF pulses and a decreased minimum echo time, the sequence successfully quantifies R_2^* in a small patient cohort. Phantom data provide a proof of concept for simultaneous R_2/R_2^* imaging using CSI.

Chapter 2

Improved Liver Iron Estimates using T_1 -Corrected Proton Density Estimator

Abstract

Purpose: CPMG spin echo series are attractive due to their time efficiency and potential to reveal unique information about tissue iron distribution. Clinical adoption remains low due to the traditionally flat relationship between CPMG-based R_2 estimates and LIC. In this work, we demonstrate that the inclusion of a proton density estimator from within acquired image datasets can increase the sensitivity of CPMG R_2 estimates to iron in both human and simulated data.

Theory and Methods: A retrospective data analysis of 50 patient records was performed, fitting CPMG spin echo data with and without a muscle-based proton density estimator segmented from within each image series. Data was compared to R_2^* -based clinical iron estimates. A Monte Carlo simulation was performed with matching imaging and fit parameters. **Results:** The sensitivity of CPMG-derived R_2 triples when a proton density constraint is applied. Over a moderate iron load range, human data snaps to one of two fit regimes. Simulation data demonstrates the same increase in sensitivity but does not demonstrate the bimodal behavior over the middle iron ranges. **Conclusion:** A proton density constraint can increase

the sensitivity of CPMG-based R_2 estimates to iron. Such an increase may allow for improved adoption of CPMG sequences over multiple single echoes for their associated scan efficiency improvements and potential for more insight into tissue iron distribution.

2.1 Introduction

Chronic anemias such as thalassemia and sickle cell disease represent the most common genetic disorders in the world. Transfusion therapy in these patients produces severe iron deposition in the liver and other organs, leading to cardiac and endocrine dysfunction and liver cirrhosis. Iron overload in transfusional siderosis cannot be treated with phlebotomy. Instead, patients receive iron chelators that bind and remove iron with dosing specific to their tissue iron content. Determining safe chelation dosing requires reliable iron quantitation techniques. Before 2005, needle biopsies were required to quantify liver iron, with their attendant risks²¹ and sampling error^{22,23,24}. Since then, magnetic resonance imaging systems have become key tools for diagnosing and monitoring iron overload disorders such as transfusional siderosis in sickle cell disease and thalassemia, hemochromatosis, liver disease, and a number of neurodegenerative disorders. Both transverse relaxivity and magnetic susceptibility measurements have been used to estimate tissue iron concentrations in the liver, heart, endocrine glands, and brain. MRI-based iron quantitation at 1.5 Tesla(T) is now standard of care.

One common approach for measuring liver iron concentration (LIC) is to estimate the transverse relaxation rate R_2 ($1/T_2$) from images formed with a spin echo (SE) pulse sequence. Most often, protocols obtain a set of single spin echo (SSE) images at a variety of echo times (TE) and fit an exponential decay curve to the

samples in the image domain. This approach yields curvilinear calibration curves relating SSE- R_2 to LIC that demonstrate high sensitivity at low iron loads and reduced sensitivity in high iron loads as the curve flattens^{4,7}. This high sensitivity, which can appear linear over a limited range of iron loads^{52,53}, is useful for precisely estimating iron loads below 20^{mg/g}. Estimating higher LICs in this manner remains a challenge due the insensitivity of the curve over higher LICs. Nonetheless, SSE series are attractive due to the straight-forward acquisition and analysis. However, scan time and the number of required breath holds grows linearly with the number of echoes desired and later echoes cannot sample useful signal in high-iron patients.

Less commonly, R_2 estimates are made using Carr-Purcell-Meiboom-Gill multiecho spin echo sequences (CPMG)^{46,54,55,49,56}. Such sequences require only one excitation to form images at a variety of echo times, reducing the scan duration while still acquiring multiple echoes. Compared to SSE, signal loss is reduced in later echoes due to the dependence of each echo on preceding echoes, leading to improved SNR in high-iron subjects. This dependence may also provide information about cellular iron distribution that cannot be assessed with SSE images⁵⁶. Gathering the necessary decay information for analysis is challenging due to CPMG's echo timing limitations. Constraints on both the minimum echo time and the interecho spacing, τ , limit CPMG's sampling more than SSE.

Despite the benefits of CPMG, its timing limitations lead to undersampling of initial signal decay. Subsequent R_2 estimates demonstrate poor sensitivity to increasing iron load due to underestimates of tissue's proton density (S_0), which hinders clinical applicability. Figure 2.1 demonstrates characteristic decay curves for R_2 values of 166 Hz (left pane, $T_2 = 6$ ms, 1.5T LIC=8.9^{mg/g}, 3T LIC=15.8^{mg/g}) and 333 Hz (right pane, $T_2 = 3$ ms, 1.5T LIC=61.1^{mg/g}, 3T LIC=28.2^{mg/g}). The left pane shows that low and moderate iron loads produce sufficient SNR that

constrained and unconstrained fitting approaches agree within 7% of each other, on par with test-retest variability for MRI-based iron quantitation. Signal from high iron loads (right pane) demonstrates over 50% disagreement between constrained and unconstrained R_2 estimates. Most of the error comes from the unconstrained technique vastly underestimating the early signal decay. By anchoring the fit with an estimate of the intersection point between the y-axis and the decay curve, the R_2 estimate captures the decay effectively. In this work, we investigate the potential of using a muscle-based S_0 constraint to improve the sensitivity of the relationship between CPMG-derived R_2 and LIC, thereby increasing the clinical applicability of CPMG series for liver iron estimation without the need to include additional scans.

2.2 Theory

The choice of signal model can have significant impact on quantitative results from MRI. In this work, we applied two signal equations to the acquired data: the Yamada CPMG signal equation and the Jensen model for non-exponential decay in the liver. The Yamada equation and similar mono-exponentials are the most common signal models used in MRI while the Jensen model specifically describes CPMG signal behavior in iron loaded tissue.

The Yamada CPMG model accounts for the R_2 envelope that is traditionally seen in spin-echo sequences as well as the T_1 weighting that is present. 2.8):

$$S(t) = S_0 \times \exp\left(-R_2 t\right) \left[1 - \exp\left(\frac{-TR}{T_1}\right)\right] \quad (2.1)$$

$$S_0 = k \times M_0 \quad (2.2)$$

where S_0 represents proton density as a product of a constant k and the initial longitudinal magnetization M_0 , R_2 represents transverse relaxation rate, and t represents echo formation time.

Although the Yamada equation is commonly used for R_2 relaxometry, it does not differentiate between the decay processes in SSE and CPMG sequences. Spins that are stationary with respect to magnetic inhomogeneities with demonstrate identical SSE and CPMG R_2 estimates. When spins diffuse their echoes are weighted by the magnetic heterogeneity experienced between any two RF pulses, leading to a cohort of spins whose apparent decay is sampling-dependent. Although the echo times produced by SSE and CPMG sequences may match, the distance between the RF pulses after the first echo will differ. In cases where proton motion distance and tissue mesostructure scale are similar, as with iron, the diffusion and sampling scheme will lead to different R_2 estimates from the two sequences. The Jensen model accounts for this by providing two decay parameters rather than one - T_1 effects are omitted for brevity:

$$S(t) = S_0 \times e^{-RR_2 t} \times \exp(-a^{\frac{3}{4}}(\Delta t)^{\frac{3}{4}}(t - t_s)^{\frac{3}{8}}) \quad (2.3)$$

where RR_2 represents reduced R_2 , a represents a nonlinear aggregation parameter, t represents time, and t_s is a time shift given by:

$$t_s = 2\tau \left[1 - \left(\frac{\tau}{\Delta t} \right)^2 \right] \quad (2.4)$$

where τ represents the time of the first RF pulse and Δt represent the time between successive RF pulses, such that echoes form at $t = 2\tau + 2(n-1)\Delta t$ (or $2n\Delta t$ when $\tau = \Delta t$). The resulting signal in the presence of iron stores is therefore a function

of properties that are intrinsic to the tissue, such as diffusion and iron aggregation, as well as acquisition parameters such as echo spacing.

2.3 Methods

2.3.1 Imaging

Patients with β -Thalassemia, Sickle Cell Disease, and other rare anemias received clinically indicated MRI assessments for liver iron content. All scans were completed on a Philips Achieva 1.5T magnet (Philips HealthTech, Best, Netherlands) on software revisions 2.6.1, 2.6.3, or 3.2.2. Imaging series were sampled from a large clinical dataset to yield a wide range of LIC burdens as part of a retrospective study jointly approved by institutional review boards at Children’s Hospital of Los Angeles and Boston Children’s Hospital (IRB#CHLA-15-00010). All scans were performed with breath holds. Three 8-echo gradient echo sequences with minimum TEs of 1.16 ms and maximum TEs of 8.6, 11.66, and 16.56 ms were used to estimate R_2^* for use as a standard LIC estimate. An 8-echo CPMG sequence with TEs from 6.5-52 ms was used to capture R_2 . Expanded imaging parameters for both protocols are shown in Table 2.1.

2.3.2 Simulation

An internally developed, previously validated Monte Carlo simulation framework was used to generate synthetic signals matching the echo times used in the clinical scans on a range of 1-50 [mg/g iron/dry tissue weight]⁵⁷. Briefly, liver tissue was modeled as 80 μm cubes of liver tissue containing 64 cuboidal hepatocytes and 18 cylindrical sinusoid regions⁵⁸. Iron overload was modeled by distributing spheres of iron in the hepatocytes using Gamma distributions to statistically

describe their size and spacing. From the iron distributions, magnetic field disturbances were calculated based on the field strength and magnetic susceptibility of iron. 2500 spin cohorts were tracked using a random walk simulation through iron distributions and obeyed cell and obstacle boundaries. A 3D Bloch equation simulator calculated the magnetization at each timestep. RF excitations and inversions were modeled as 90° and 180° instantaneous flips; the CPMG phase cycling scheme was applied. Iron-free relaxation rates T_1 and T_2 were set to 576 ms and 42 ms, respectively⁵⁹. Iron-mediated T_1 enhancement was not modeled in the simulations due to the lack of scan repetitions obviating the need for T_1 correction.

2.3.3 Analysis

Image series were segmented for whole liver and bilateral latissimus dorsi skeletal muscle regions of interest (ROI) in a single mid-hepatic slice by a cardiologist with 15 years experience and a graduate student with 5 years experience. R_2^* estimates were derived from magnitude gradient echo images using a previously validated pseudo-pixel wise technique with gradient echo images⁶⁰; R_2^* values were used to generate reference LIC estimates using the Wood R_2^* -LIC calibration⁴ via equation 2.5:

$$FE_{R_2^*} = 0.0254 \times R_2^* + 0.202 \quad (2.5)$$

R_2 was estimated by fitting sampled data with a signal model based on Yamada's CPMG signal equation⁶¹. A constant c was added to account for magnitude noise bias and the T_1 weighting was omitted in favor of weighting muscle signal (see equation 2.8)

$$S(t) = S_0 \times \exp\left(-R_2 t\right) + c \quad (2.6)$$

We also tested Jensen's iron-specific, non-exponential signal model (see equation 2.4), including an additional c parameter representing noise bias:

$$S(t) = S_0 \times e^{-RR_2t} \times \exp(-a^{\frac{3}{4}}(\Delta t)^{\frac{3}{4}}(t - t_s)^{\frac{3}{8}}) + c \quad (2.7)$$

A Levenburg-Marquardt algorithm was used to fit the signal models to magnitude images (pseudopixel-wise⁶⁰) and simulation data (all spin cohorts averaged, magnitude acquired at echo times noted in CPMG protocol). Both fitting models assumed that RF pulses achieved perfect 90° excitations and 180° inversions. All research fits were performed using a non-negativity constraint on values of S_0 , R_2 , a and c .

After fitting both signal models to the data, a second set of fits were generated after placing a more strict constraint on the value of S_0 . We assumed that the initial point on the R_2 decay curve should only be weighted by the liver's proton density, not the presence of iron. Skeletal muscle was chosen as a surrogate for proton density because its resistant to iron uptake provided a reliable reference tissue in all patients. Based on the reported densities of 1.06^{kg/L} and 1.02^{kg/L} for muscle⁶² and liver⁶³, respectively, we assumed that skeletal muscle and muscle would have approximately the same S_0 . PDEs were determined in the image series by performing ROI-averaged T_2 estimation with T_1 correction on the skeletal muscle signal using the T_1 term from the Yamada equation and assuming muscle T_1 to be 1008 ms⁵⁹:

$$S_{\text{muscle,corrected}} = S_{\text{muscle,acquired}} \times \frac{\left[1 - \exp\left(\frac{-TR}{T_{1,\text{liver}}}\right)\right]}{\left[1 - \exp\left(\frac{-TR}{T_{1,\text{muscle}}}\right)\right]} \quad (2.8)$$

The PDE in the simulations was known apriori. Liver T_1 was initially estimated using a T_2 value from a linearized exponential fit and then iteratively refined three times using an internally derived LIC- T_1 model. In constrained fits, S_0 was constrained to $\pm 10\%$ of PDE estimate value from T_1 -corrected muscle signal (equation 2.8). Muscle and liver of all iron loads were assumed to have identical proton density values.

Constrained and unconstrained T_2 fits were compared using gradient-echo based reference LIC estimates in human subjects or specified simulation iron loads as the standard iron load metric.

2.4 Results

Retrospective patient data analysis was completed in 50 patients (24M, 26F, 16.4 ± 9.4 years, 24 Thalassemia, 6 Sickle Cell Disease, 5 Diamond-Blackfan Syndrome, 15 Other Rare Anemia) with a broad range of LIC. Figure 2.2 demonstrates the unconstrained R_2 estimates versus R_2^* -derived LIC. Linear regression is shown for comparison with two linear models demonstrated in previous research⁶⁴. The data compared to the R_2 -MR_HIC (R_2 vs LIC derived from ratio of liver to muscle)⁶⁵ and R_2 -LIC (R_2 vs LIC derived from R_2^*)⁴ models demonstrate adjusted r^2 values of 0.85 and 0.87, respectively, suggesting that the acquired data is representative of data used in other studies.

Figure 2.3 demonstrates unconstrained and constrained R_2 estimates of human data and polynomial regression of simulation R_2 vs LIC; the St. Pierre calibration curve between SSE- R_2 and LIC is included for reference. Unconstrained human and simulation R_2 estimates demonstrate weak correlation with LIC. Agreement between unconstrained estimates in patients and simulation data was strong across

all iron burdens, with all but 2 patient R_2 estimates falling within the 95% confidence intervals of the simulation estimates. S0-constrained R_2 estimates in both human and simulation data display a increased sensitivity to LIC. The simulation fit and St. Pierre reference curve agree within 10% up to an LIC of 30 mg/g . At low and high iron loads, constrained patient R_2 estimates agreed with constrained simulation fits, displaying the same increase in R_2 -LIC sensitivity. Over an intermediate region from 12-22 mg/g LIC, constrained patient R_2 fits demonstrated increased LIC sensitivity compared to matched unconstrained fits, but most fell significantly below the confidence interval of the simulated fits.

The both constrained and unconstrained RR_2 estimates demonstrated a weak dependence on LIC, similar to the behavior of R_2 in the unconstrained Yamada signal model. The unconstrained RR_2 shows slightly higher sensitivity than the constrained RR_2 . The a parameter was insensitive to LIC in the unconstrained fits, demonstrating a curvilinear sensitivity in the constrained fits similar to the behavior of the constrained R_2 in the Yamada fits.

2.5 Discussion

CPMG sequences have been proposed as rapid alternatives to SSE acquisitions for LIC determination but remain impractical due to insensitivity between LIC and R_2 . We demonstrate by analysis of acquired images and synthetic MRI signals that sensitivity can be improved by including a proton density estimator to capture rapid initial signal decay. The signal from iron loaded tissue acquired with a CPMG sequence is non-exponential⁵⁶ — a non-exponential, rapid decay component is governed by “near-field” iron stores and an exponential slow decay component called “reduced R_2 ” accounts for diffuse iron storage. Adequately sampling the

rapid decay component is challenging because the minimum first echo time is limited around 4 ms for a slice-selective acquisition. Jensen noted that capturing the initial decay is particularly important in high-iron tissues and his model; the model permits a first echo time that is shorter than the CPMG interecho spacing for this reason. However, attempts to vary the interecho spacing or first echo time over multiple acquisitions to improve fitting constraints reduces the time savings of using CPMG.

In addition to the acquisition challenges, the problem of separating the fast and slow decay components with a single CPMG series is ill-posed because there are three free fit parameters (S_0, a, RR_2) in the Jensen model. In fact, when the condition $a \lesssim (\Delta t)^{-3/2}$ is not met, the rapid-decay signal cannot be detected at all⁵⁶. Imaging magnets cannot achieve sufficiently short TEs to capture the rapid decay for even moderate-iron patients. It is therefore attractive to fit with simpler models like a mono-exponential which has only two free parameters(S_0, R_2). Mono-exponential fitting leads to a weighted average of the fast and slow decay components with the proportion of fast decay signal increasing with LIC⁴⁹. Due to TE limitations, mono-exponential fitting mostly ignores the fast decay and almost exclusively fits the slow-decay component of the non-exponential model. This is apparent in figure 2.4, where unconstrained R_2 tracks the relatively iron-insensitive RR_2 from both constrained and unconstrained fits of a single CPMG series while the a parameter increases with liver iron. The agreement between the constrained and unconstrained Jensen fits and the unconstrained mono-exponential R_2 estimates suggests that the lack of a proton density constraint leads to the fitting of only the slow decay component, which saturates between 2.5 and 8 mg/g. Previous work by Ghugre⁴⁹ demonstrated that increasing echo spacing leads to a decrease in the fast-decay component of a bi-exponential fit rather than a change

in the decay rate of either exponential. This is similar to our finding that the unconstrained mono-exponential fits primarily capture the slow-decay component.

Due to the complete loss of fast decay species at clinically achievable first echo times, unconstrained mono-exponential fits will underestimate proton density. Unconstrained exponential fitting of simulation data underestimated proton density by up to 70% of its known value. Similar behavior was noted in-vivo when comparing to a muscle-based proton density estimate. Such a precipitous drop in S_0 cannot be accounted for by the mass of the iron alone. Without a physical basis for the decrease in S_0 , applying a constraint can reduce the sampling bias that favors the slow decay component. This approach is similar to that used to constrain bi-component exponential fits of SSE data in FerriScan®, Resonance Health, Australia)⁶⁶. By using an S_0 constraint derived from tissue whose iron load is independent of disease status, we can effectively increase the weight of the fast decay component and increase the LIC sensitivity of mono-exponential R_2 estimates. Signal decay in tissue with mild iron overload is primarily governed by diffuse iron and exhibits slow decay that can be adequately fit with either a constrained or unconstrained exponential (figure 2.1, left panel). In high-iron tissues, the fast decay component is more prevalent and the signal demonstrates primarily rapid decay that cannot be sampled with long echo times. The decay is recovered by the application of the proton density constraint (figure 2.1, right panel). However, signals from moderate iron tissues demonstrate non-negligible fast and slow decay components. When attempting to apply a constrained mono-exponential, the fits snap to one of the decay regimes more effectively than the other, leading to the bimodal fitting distribution demonstrated by our constrained patient fits. We hypothesize that uncorrected noise rectification may be partially responsible for this effect⁶⁷. Applying a Rician noise correction or fitting in the complex domain

will capture noise behavior better than a bias constant. Fat is also known to be present in concentrations of about 0-20% in the liver, but the contributions from fat have been ignored. Over the bimodal regime, the CPMG's relatively short TR may lead to amplification of fat brightness in later echoes to artificially decrease the apparent decay rate. We hope to study the effects of noise and fat in future work.

The constraints chosen in this work were selected to be wide enough to reasonably accommodate all clinical iron burdens without prior knowledge of iron load or additional scans. For this reason, estimates of non-idealities in the muscle-based PDE or corrections could not be made. Including additional scans may further improve constrained estimates by gathering information on other non-idealities. For example, nonuniform RF excitation due to B_1^+ inhomogeneity or spatial variation of coil sensitivity could produce images that show signal intensity difference between muscle and liver, leading to poor S0 constraints. Subsequent fits using the constraint would demonstrate increased error. Without a B_1^+ correction to ensure that the muscle-based PDE and the liver signal intensities are appropriately normalized, reducing the variation seen in patient fits will be difficult. Despite perfect knowledge of the proton density in the simulations and the absence of T_1 effects, the 95% confidence intervals on the simulation fit data indicate that S0-constrained R_2 estimates from CPMG data still have confidence bounds of over $10^{\text{mg/g}}$, matching the demonstrated patient variation.

2.6 Conclusion

Muscle-based proton density estimators derived from within existing imaging datasets provide a robust way to increase the sensitivity of CPMG-based R_2 estimates, increasing the potential clinical utility of such a sequence. The effect was demonstrated in both human and simulated data. Improved selection of scan timing parameters, signal models, and fitting techniques may improve the accuracy of estimates that rely on a proton density estimator.

2.7 Acknowledgements

This research is supported by the National Institute of Diabetes, Digestion and Kidney Diseases of the National Institutes of Health, grant 1R01DK097115-01A1. Computation for the work described in this paper was supported by the University of Southern California's Center for High-Performance Computing (hpc.usc.edu).

Spin Echo

Type	CPMG Multi echo sequence
TE	6.5, 13, 19.5, 26, 32.5, 39, 45.5, 52 ms
TR	247 ms
NSA	1
Voxel Size	2.5x2.5mm
Slice Thickness	8 mm
Matrix	64x64
Bandwidth	4.1 kHz/pixel

Gradient Echo

Type	Multi-echo GRE Sequence
Echo Time	1.16, 2.22, 3.28, 4.35, 5.41, 6.47, 7.54, 8.60 ms (short T_2^*) 1.16, 2.66, 4.16, 5.66, 7.16, 8.66, 10.16, 11.66 ms (medium T_2^*) 1.16, 3.36, 5.56, 7.76, 9.96, 12.16, 14.36, 16.56 ms (long T_2^*)
TR	50 ms
NSA	1
Voxel Size	1.25x1.25mm
Slice thickness	8mm
Matrix	128x128
Bandwidth	1.5 kHz/pixel

Table 2.1: Relevant scan parameters for patient exam.

Measurement	Min	Max	Mean±StDev
Height [cm]	117	179.8	156.2±15.3
Weight [kg]	20.1	89.7	54.3±17.1
Body Surface Area [m^2]	0.81	2.1	1.5±.3
Body Mass Index [kg/m^2]	14.7	34.3	21.9±5.1
Ferritin [ng/mL]	199	16300	4483±4890
ALT [U/L]	18	391	74.5±84.5

Table 2.2: Ranges of demographic and laboratory data for the participant population

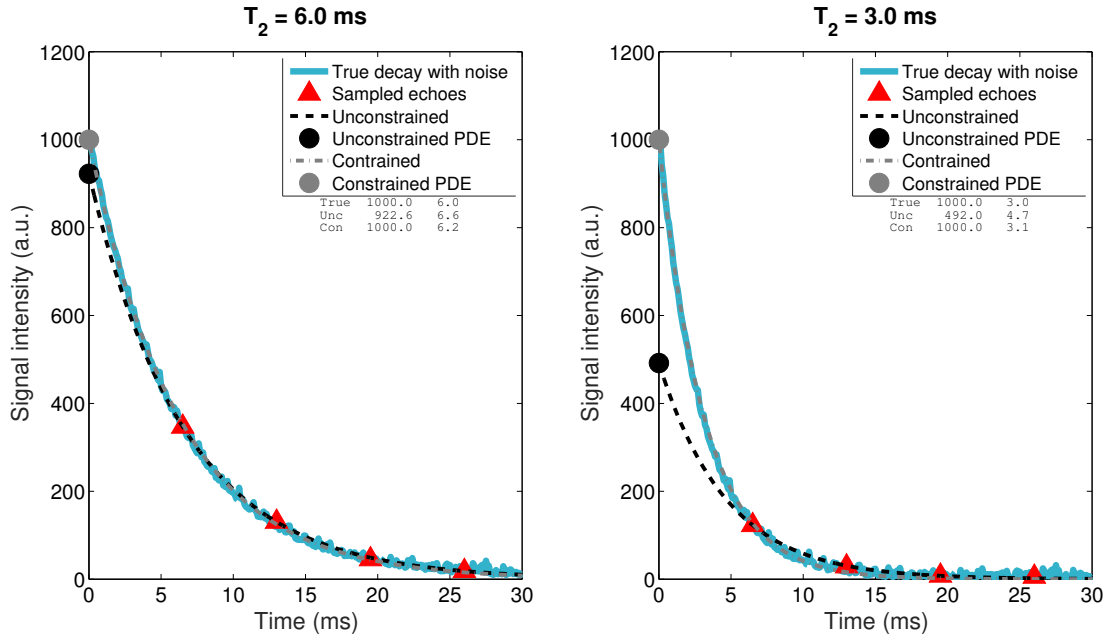


Figure 2.1: Example of unconstrained and constrained mono-exponential fits for different R_2 species. When the decay rate is comparable to the first echo time (left), the proton density is underestimated by 8% and the R_2 is overestimated by 10%. The same trend is seen to a more extreme degree in the right pane where the R_2 is shorter.

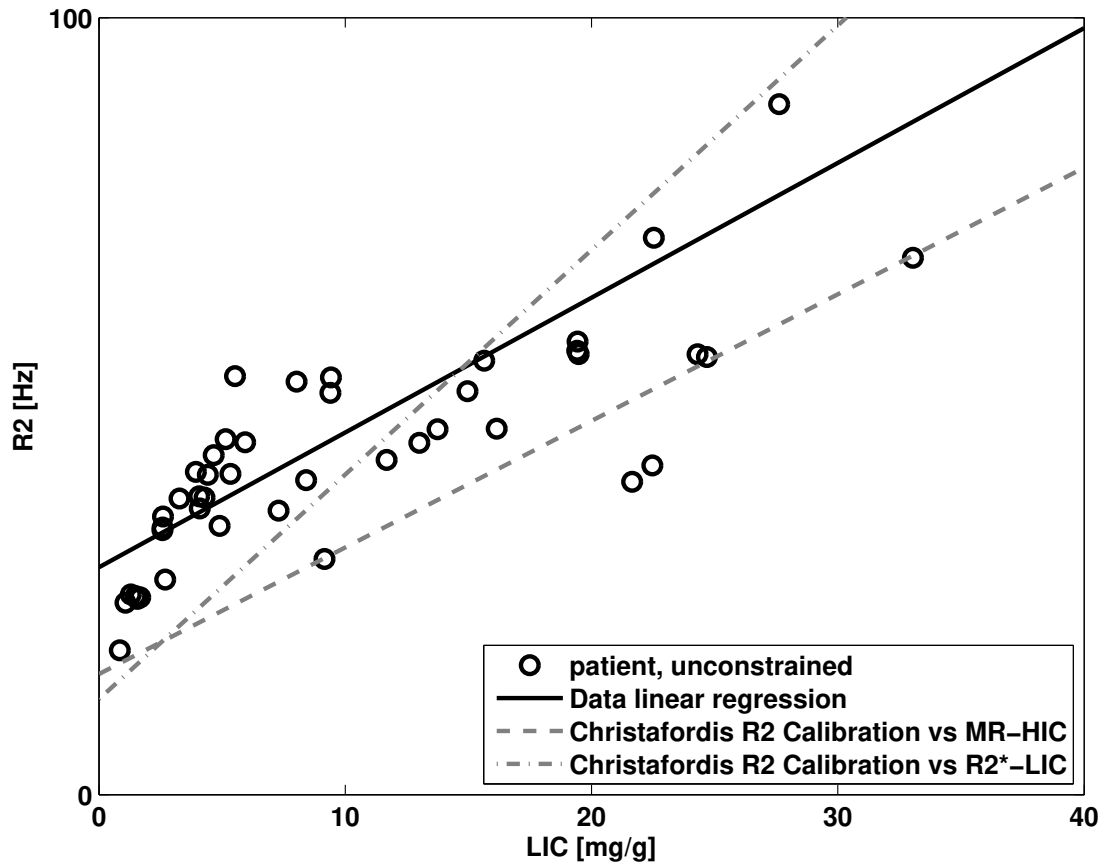


Figure 2.2: Unconstrained fits of acquired CPMG data plotted against LIC demonstrated that curves derived by Christoforidis show similar fit to the data. The disagreement in slope of fit compared to the Christoforidis- R_2^* curve likely results from the apparent saturation of their protocol due to shorted TE of 2.24 ms in the gradient echo protocol.

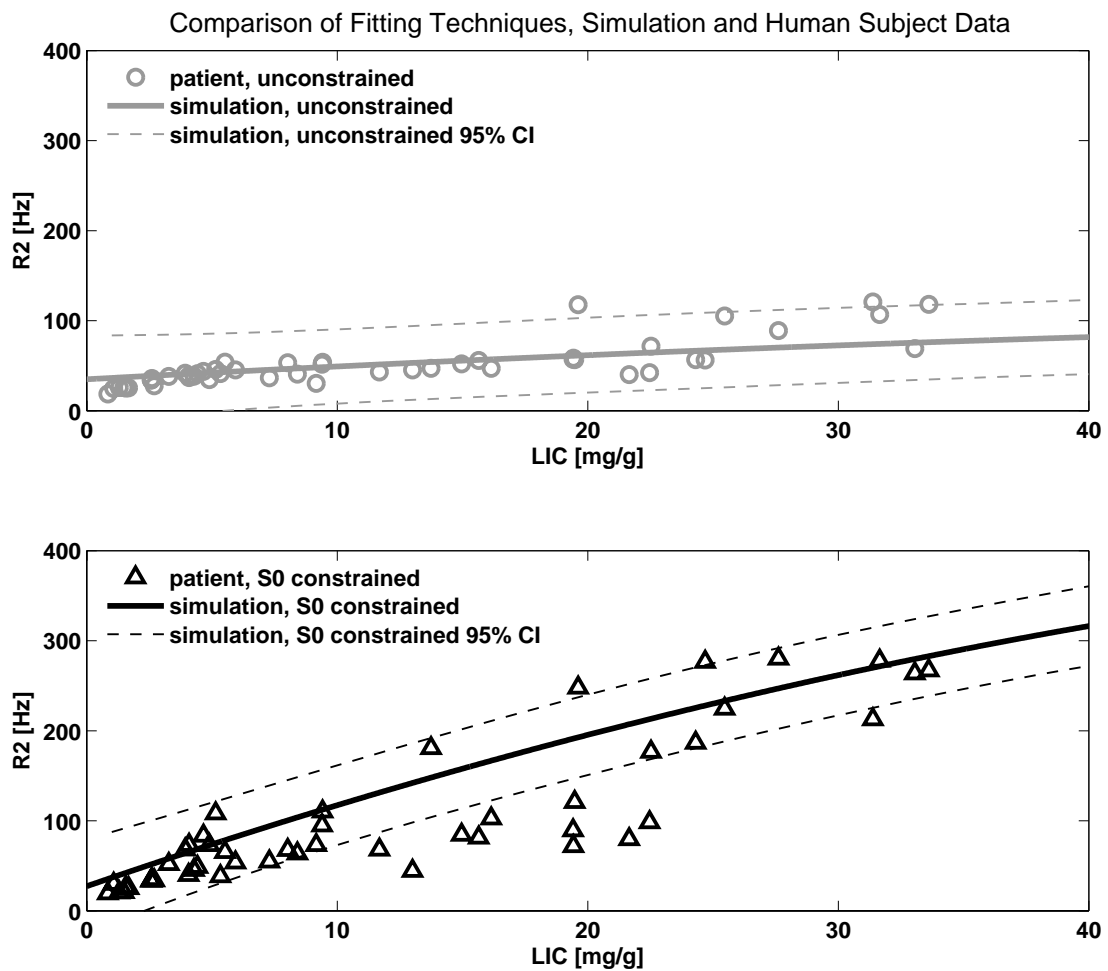


Figure 2.3: Comparison of fitting techniques. Top pane demonstrated the weak relationship between R_2 and LIC in the unconstrained fits. Lower pane shows the approximate tripling of the calibration curve with the addition of the PDE constraint.

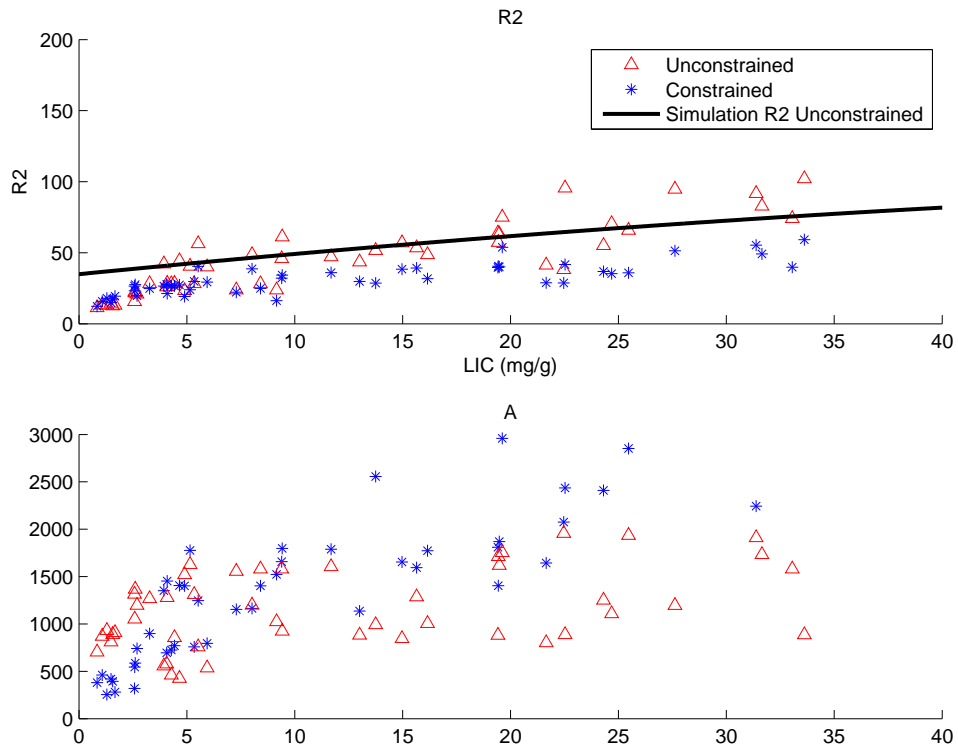


Figure 2.4: Constrained vs unconstrained fitting of Jensen curve demonstrates that sensitivity of the RR_2 parameter (top pane) follows the behavior of the unconstrained R_2 estimates. The unconstrained aggregation parameter (lower pane) was less correlated tissue iron content but demonstrated large variation. In contrast, the constrained RR_2 saturates quickly; the aggregation parameter (lower pane) increases with iron for the constrained fits. This suggests that the background RR_2 may represent saturating ferritin stores while the a parameter represents large iron particles.

Chapter 3

Relaxivity-iron calibration in hepatic iron overload: Predictions of a Monte Carlo model

Abstract

3.0.1 Purpose

R_2^* ($1/T_2^*$) and single echo R_2 ($1/T_2$) have been calibrated to liver iron concentration (LIC) in patients with thalassemia and transfusion-dependent sickle cell disease at 1.5 Tesla. The R_2^* -LIC relationship is linear while that of R_2 is curvilinear. However, the increasing popularity of high-field scanners requires generalizing these relationships to higher field strengths. This study tests the hypothesis that numerical simulation can accurately determine the field dependence of iron-mediated transverse relaxation rates.

3.0.2 Methods

We have previously replicated the calibration curves between R_2 and R_2^* and iron at 1.5T from using Monte Carlo models incorporating realistic liver structure, iron deposit susceptibility, and proton mobility⁵⁷. In this paper, we extend our model to predict relaxivity-iron calibrations at higher field strengths. Predictions

were validated by measuring R_2 and R_2^* at 1.5T and 3T in six β -thalassemia major patients.

3.0.3 Results

Predicted R_2^* increased two-fold at 3T from 1.5T while R_2 increased by a factor of 1.47; patient data exhibited a coefficient of variation of 3.6% and 7.2%, respectively, to the best-fit simulated data. Simulations over the 0.25-7T range showed R_2^* increasing linearly with field strength while R_2 exhibited a concave-downward relationship.

3.0.4 Conclusion

A model-based approach predicts alterations in relaxivity-iron calibrations with field strength without repeating imaging studies. The model may generalize to alternative pulse sequences and tissue iron distribution.

3.1 Introduction

MRI has gained clinical acceptance as a non-invasive tool to monitor tissue iron stores in patients with iron overload syndromes. Relaxation rates R_2 ($1/T_2$) and R_2^* ($1/T_2^*$) have been calibrated to liver biopsy on 1.5T scanners to quantify liver iron concentration (LIC) with clinical accuracy^{7,4}. R_2^* increases linearly with LIC while R_2 has a curvilinear relationship. However, these relationships have not been extensively characterized for higher field strengths.

While one can physically calibrate imaging techniques across field strengths, it is tedious and expensive. An alternative approach is to use numerical modeling by generating realistic (iron overloaded) liver geometries and simulating R_2 and

R_2^* imaging experiments. Such a model has already been successful in predicting R_2^* -iron and R_2 -iron relationships within tolerable limits of clinical accuracy at 1.5T⁵⁷. Here we extend the model to find relaxivity with respect to iron, or iron-relaxivity calibration, over a range of field strengths. To validate the predictions of the model, we performed R_2 and R_2^* imaging of the liver at 1.5T and 3T in six patients with transfusional iron burden and 11 non-iron overloaded controls.

3.2 Methods

We modeled the liver architecture as consisting of hepatocytes and sinusoids, ignoring vascular and biliary structures. As previously described⁵⁷, realistic liver geometries were simulated as 80 μm blocks consisting of 64 cuboidal hepatocytes. Sinusoids were represented as 18 cylindrical regions with a diameter of 10 μm and height of 20 μm . Hepatic iron concentration was in the clinically-relevant range of 0.5-40 mg/g dry tissue weight and corresponding volume fractions of iron deposits were determined from prior relationship⁶⁸. Spherical iron deposits were distributed in this virtual environment based on Gamma distribution functions that represented particle size, inter-particle distance and inter-cellular iron anisotropy⁶⁸. Sinusoidal iron fraction was determined from a previously derived relationship⁶⁹. Each iron load geometry was independently generated and represented a virtual patient. The magnetic susceptibility of the impenetrable spherical iron deposits was computed assuming a 4:1 mixture of hemosiderin and ferritin and using literature values of 1.1E-6 and 1.6E-6 $\text{m}^3/\text{kg}_{\text{Fe}}$ respectively^{70,71}. 5000 protons performed a random walk (diffusion coefficient = 0.76 m^2/ms ⁶¹) through the magnetic environment and FIDs were computed from phase accruals, providing R_2^* estimates. Tissue wet-to-dry weight ratio was assumed to be 4:1⁵⁰. A single echo

experiment with echo times (TE) logarithmically spaced between 0.1-30 ms was also simulated to measure R_2 . Echo times were chosen to maximize the dynamic range of the simulation for the computation time. Protons could not cross hepatocyte boundaries. The model neglected any contact or exchange mechanisms. Details of MRI simulation have been described earlier⁵⁷.

Monte Carlo simulations were performed at field strengths of 1.5T, 3T, and ten other field strengths in the range of 0.25-7T. Realistic liver geometry and iron morphology was employed with hepatic iron concentrations in the range of 0.5-40 mg/g. R_2^* and R_2 values were estimated from signal decay curves corresponding to each iron burden. Simulations were subsequently extended up to 60 mg/g hepatic iron concentration for comparison. Bland-Altman analysis was performed with matched pairs of iron-loaded patient and simulation data for R_2 and R_2^* at 3T to determine bias and standard deviation.

In-vivo validation scans were performed as part of a prospective, Institutional Review Board (IRB)-approved study using a phased array coil on 1.5T and 3T GE Signa Twinspeed systems. Consent was obtained from six thalassemia major patients (2 male, 4 female; ages 12-44) or minors' legal guardians, and 20 non-iron overload subjects (10 male, 10 female; ages 19-41). Liver R_2^* was measured in a single mid-hepatic slice using a multiple-echo gradient echo sequence with 16 equally spaced echo times(TE) from 1.2 – 17.2 ms, flip angle(FA)=20, repetition time(TR)≈13 ms, bandwidth(BW)=83.3 kHz, number of averaged excitations(NEX)=6, and matrix size=128x128. In patients in whom signal intensity was completely extinguished by the second echo, the protocol was modified to have a first TE=0.8 ms, FA=10, TR=10 ms, and NEX=8. The sequence was repeated at the same gain settings using manually incremented initial echo times (TE=0.1 or 0.2ms); the first echo time was increased until the liver tissue appeared

black. The echoes from each scan were combined and ROIs manually adjusted to improve sampling of rapid decay. A comprehensive description of the procedure is described in⁷². Liver R₂ was measured in 4 slices using a 90-90 Hahn spin echo sequence with TE=[3,3.5,5,8,12,18,30] ms at 1.5T and TE=[4,5,8,12,18,30] ms at 3T, TR=300 ms, BW=62.5 kHz, NEX=1 and matrix size=64x64⁷². R₂ values were computed in 16 regions of interest (4 per slice) by fitting the mean signal decay to an (exponential+constant) model⁷³. R₂ imaging was not performed in control subjects.

Relaxation rates at 3T were compared with those at 1.5T for both model and experimental data. Similarly, the variation in relaxivities (defined below) with field strength was investigated and characterized using linear and power law relationships over the range 0.25 – 7T. Relaxivity is defined as the increase in the relaxation rate with iron concentration, , at a given field strength in units of [mM⁻¹ * s⁻¹]. Relaxivity enhancement (RE), the increase of relaxivity with field strength, was calculated between arbitrary field strengths B₀ and 1.5T as follows:

$$E(B_0) = \frac{\frac{\partial R}{\partial C}|_{B_0}}{\frac{\partial R}{\partial C}|_{1.5T}} \quad (3.1)$$

where C represents the iron concentration in mg/g dry weight and R represents either R₂ or R₂^{*}. To generalize the relationship, relaxivity enhancement was plotted against field strength and fit to linear equations. For R₂, log transformation of both RE and field strength was needed to linearize the relationship.

For the purpose of this work, relaxation is modeled as follows:

$$R = R_i + R' \quad (3.2)$$

where R is the relaxation rate (R_2 or R_2^*) of a given tissue sample with iron, R_i is the intrinsic relaxation rate without iron, and R' is the extrinsic relaxation rate due to iron load.

By applying the RE equation to the relaxation model, we find the following transformation to translate R_2 and R_2^* values from 1.5 Tesla to any arbitrary field strength:

$$R(Y) - \alpha_Y = (R(1.5T) - \alpha_{1.5}) \times RE_R(Y) \quad (3.3)$$

where R is the relaxation rate (R_2 or R_2^*) for a given field strength, α_Y is the corresponding intrinsic liver relaxation rate, and RE is the relaxivity enhancement for a given field strength. The background relaxation was assumed to be 20 s^{-1} independent of field strength for the simulations.

3.3 Results

Figure 3.1 shows simulated R_2^* and R_2 values as a function of iron concentration for both 1.5T and 3T. Simulated R_2^* (Figure 3.1a) rises linearly with iron concentration for both 1.5T and 3T. The ratio of the slopes (i.e. the predicted RE at 3T relative to 1.5T) was 2.01 ± 0.01 (mean \pm std). Simulated 1.5T values fall within the 95% confidence intervals derived from liver biopsy studies in humans⁴. Simulated R_2 estimates (Figure 3.1b) follow a concave downward pattern with increasing iron concentration at both 1.5 and 3T; this curvilinearity results from increased static refocusing at high iron concentrations^{57,74}. While simulated R_2 is higher at 3T than at 1.5T, the effect is not as large as for R_2^* . The 1.5T R_2 -iron calibration falls within the 95% confidence bounds derived from human liver biopsy data^{7,4}.

Figure 3.5a shows the relationship between R_2^* at 3T and 1.5T for both simulation and patient data. The R_2^* values are highly correlated with an r^2 of 0.999. The slopes of the best fit lines were 2.01 ± 0.01 for the model and 2.00 ± 0.06 for the patient and control data. Thus, within measurement precision, both model and patient data demonstrated a two-fold increase in R_2^* at 3T relative to 1.5T, in agreement with reference⁷². Bland-Altman analysis of R_2^* (3.5a) demonstrated no significant bias between observed and predicted R_2^* with a standard deviation of 3.6%; predicted R_2^* was calculated from the best-fit line of the simulated 3T-1.5T relationship. Figure 3.5b shows R_2 at 3T versus 1.5T; the model-predicted relationship was highly linear with an r^2 of 0.996. The regression slope of the simulated data was 1.47 ± 0.01 , indicating that R_2 at 3T averaged 47% higher than measured at 1.5T. For the patient data, the regression slope was 1.34 ± 0.07 . Bland-Altman analysis again demonstrated that observed and best-fit predicted R_2 (figure 3.5b) were unbiased and had a standard deviation of only 7.2%.

In order to generalize the effect of magnetic field on relaxivity, simulations were repeated for multiple field strengths. Figure 3.5 shows model-predicted R_2^* and R_2 relaxivities over the range 0.25 – 7T, relative to corresponding relaxivities at 1.5T. For R_2^* , the RE was a linear function of field strength, as expected, but for R_2 it represented a power law relationship (linear on a log-log scale). The equations of the best-fit lines are given by

$$E_{R2}(B_0) = 0.8 \times B_0^{0.56} \quad (3.4)$$

$$E_{R2*}(B_0) = -0.0086 + 0.68 \times B_0 \quad (3.5)$$

where γ is the field strength in units of tesla. Note that the second equation is very close to the expected relationship:

$$E_{R2*}(Y) = \frac{Y}{1.5} \quad (3.6)$$

Equations 4 and 5 predict RE factors of 2.03 and 1.48, respectively, for 3T. If R_2 and R_2^* calibration curves are known at 1.5T, they can be translated to other field strengths using equations 3.4 and 3.5.

3.4 Discussion

With the increased migration to 3T scanners, existing calibration curves must be translated to higher fields. 3T MRI scanners offer higher signal-to-noise ratio, which can be traded for improved resolution or speed. A 2007 study⁷² established the relationship between R_2^* at 3T and 1.5T over a wide range of LIC; R_2^* increased two-fold with field strength in agreement with our model predictions. A recent publication by Meloni et al. also demonstrated doubling of R_2^* at 3T compared to 1.5T⁶⁰. Similar relationships have been shown in cardiac tissue^{72,60}. In our study, 1.5T simulations were in excellent agreement with in-vivo calibration curves (Fig. 3.1a) and predicted R_2^* enhancement was linear with static magnetic field strength (Fig. 3.5). This result is expected since higher fields proportionally increase the magnetization of the iron particles through the equation

$$M = \chi H \quad (3.7)$$

where M is the magnetization, χ is the magnetic susceptibility of the particles, and H is the applied field. At higher iron concentrations, diffusing water protons

encounter spatially larger magnetic inhomogeneities and R_2^* is primarily determined by magnetic susceptibility⁵⁷.

On the other hand, R_2 enhancement demonstrated a non-linear relationship with field strength (Fig. 3.1b, Fig. 3.5). The higher field strength expands the range of static refocusing, particularly at higher iron concentrations, partially saturating R_2 at high iron concentrations. This occurs because the iron-dependent field inhomogeneities grow with field strength. This moves more protons near iron stores into the static refocusing regime in which the phase accrual can be completely refocused by a spin echo. The increase in size of this regime increases the likelihood that a spin will experience a static increase in field strength over its diffusion window rather than a local field inhomogeneity. Thus, R_2 values at 3T were only 47% higher than values at 1.5T. The experimental agreement of these predictions at 3T is excellent (Fig. 3.5). Previously, the field dependence of R_2 had been studied only in the heart over a relatively small range of iron concentrations⁶⁰. The R_2 enhancement factor between 1.5T and 3T was reported to be approximately 1.55⁷⁵, comparing favorably with our estimate of 1.47. The in-vivo estimate for relaxivity enhancement from our liver data showed an estimate of 1.34; we believe that limitations in the spin echo pulse sequence caused the estimates for high-iron decay rates to be less reliable than moderate iron loads and will be corrected with improved pulse sequences. It was not possible for our group to validate our predictions for higher field strengths, but these data establish testable benchmarks. We acknowledge that the calculation of RE depends on assuming that the iron-mediated relaxation dominates that of the base tissue. Our RE values are targeted at patients with moderate to high iron loads; to determine a RE value for lower iron loads, the relationship in equation 3 must be applied to account for the nonlinear enhancement in base tissue relaxation rates.

From a practical imaging perspective, these simulations have important consequences. Maximum measurable R_2^* and R_2 are hardware limited by the minimum achievable echo time. Since R_2 values scale more slowly with field strength than R_2^* values, it may be easier to use spin-echo measurements to quantify high LIC concentrations at higher field. R_2^* estimation at high field may require specialized techniques such as the use of free induction decay measurements, center-out radial acquisitions, ramp sampling, half pulse excitations, or other variations of ultra-short echo time imaging^{76,77}. In this manuscript, we have demonstrated how a generalized and validated Monte Carlo model can be used to predict relaxivity-iron behavior at different field strengths. Future extensions of the model could include simulating a different MRI pulse sequence including, for example, the multi-echo CPMG sequence. Iron calibration curves have been obtained experimentally for CPMG sequences^{54,55,49} but differ from the spin echo R_2 relationships. The model can be used to interrogate complicated CPMG behavior and expose complex interplays among proton diffusion, effective particle size and inter-echo spacing. Furthermore, underlying mechanisms of the nonexponential nature of MRI signal in the presence of magnetic inhomogeneities can also be studied^{49,56}. Lastly, accurate values for diffusion coefficient (D) of protons in liver tissue are currently lacking; even the published value of 0.76⁵¹ has a large standard deviation of 0.27. More recent estimates of the diffusion coefficient show standard deviations of 25-50% of the estimated ADC⁷⁸. The virtual liver model can be used to calculate an ‘effective D ’ and test whether there is any systematic dependence on iron concentration. Accurate values of D are critical for structure, motion and time sensitive sequences like CPMG. It would also be interesting to see if field-dependent relaxation enhancement (Fig. 3.5) is modified by the diffusion coefficient. R_2^*

enhancement should not change since R_2' is unaffected by D while the effect on R_2 enhancement is not clear since R_2 is systematically altered by changes in D⁵⁷.

Figures 3.1 and 3.5 demonstrate some variability that may appear to be iron-load dependent. Because the iron geometries are generated in an independent manner, the variability in RE with iron load is a result of the stochastic nature of the iron generation process rather than the random proton paths. Each simulated sample represents a single patient and decreasing the variability would require numerous simulations at each iron load for computational efficiency. These iron geometries were reused across the field strengths so some apparent variation is indicative of a single iron distribution's properties rather than systematic dependence on iron load. This variability could be reduced by performing multiple simulations at each iron load and averaging the results.

This study was limited by modest validation with experimental data. For the field-dependent study, R_2^* and R_2 was measured in only 6 subjects with significant iron overload. However, these data spanned a wide range of LIC measurements (~3-35 mg/g dry wt.)⁷ and were in excellent agreement with the model. Since the choice of R_2^* measurement protocol required a subjective decision, it is possible that a selection bias could be introduced into the high-iron R_2^* estimates. Ongoing 3T-1.5T comparisons in larger patient populations will provide further validation of the model. We additionally hope to perform scanning at additional field strengths when such a scanner is available to us. At 3T and above, a customized pulse sequence will be required to quantify higher R_2^* and R_2 values than measured in the present study. Additionally, no systematic study into the relationship between the hemosiderin-ferritin ratio and iron load has been conducted; it is conceivable that molar magnetic susceptibility may depend on liver iron burden.

We have demonstrated that a computational model utilizing realistic liver architecture and iron morphology can likely extend iron calibrations to higher magnetic field strengths. Characterization of the R_2 -iron calibration at 3T is novel and may improve patient access to LIC estimates at centers having only 3T scanners. However, the real power of the model lies in predicting changes to R_2^* and R_2 calibration curves in response to modifications of MRI pulse sequences, field strength, and systemic disturbances in tissue iron distribution. Non-idealities of the imaging sequences can also be easily modeled to determine their impact on iron calibration curves. Understanding key parameters of the relaxivity-iron behavior can also help in creating tissue-specific models (through autopsy studies) for organs which iron concentration cannot be probed via biopsy e.g. heart, kidney, and pancreas. While *in silico* calibration curves always warrant targeted experimental verification, Monte Carlo simulation can greatly reduce dependence on expensive validation studies, shortening the design cycle for novel techniques.

3.5 Acknowledgements

We would like to acknowledge the following sources of funding: General Clinical Research Center (National Institutes of Health, RR00043-43), Department of Pediatrics at Children’s Hospital Los Angeles (CHLA), National Institute of Diabetes, Digestive and Kidney Diseases (1 RO1 DK097115-01A1), National Heart Lung and Blood Institute of the National Institutes of Health (1 R01 HL75592-01A1), Novartis Pharma AG., The Wright Foundation, Saban Research Institute at CHLA. Computation for the work described in this paper was supported by the University of Southern California Center for High-Performance Computing and Communications (hpcc.usc.edu).

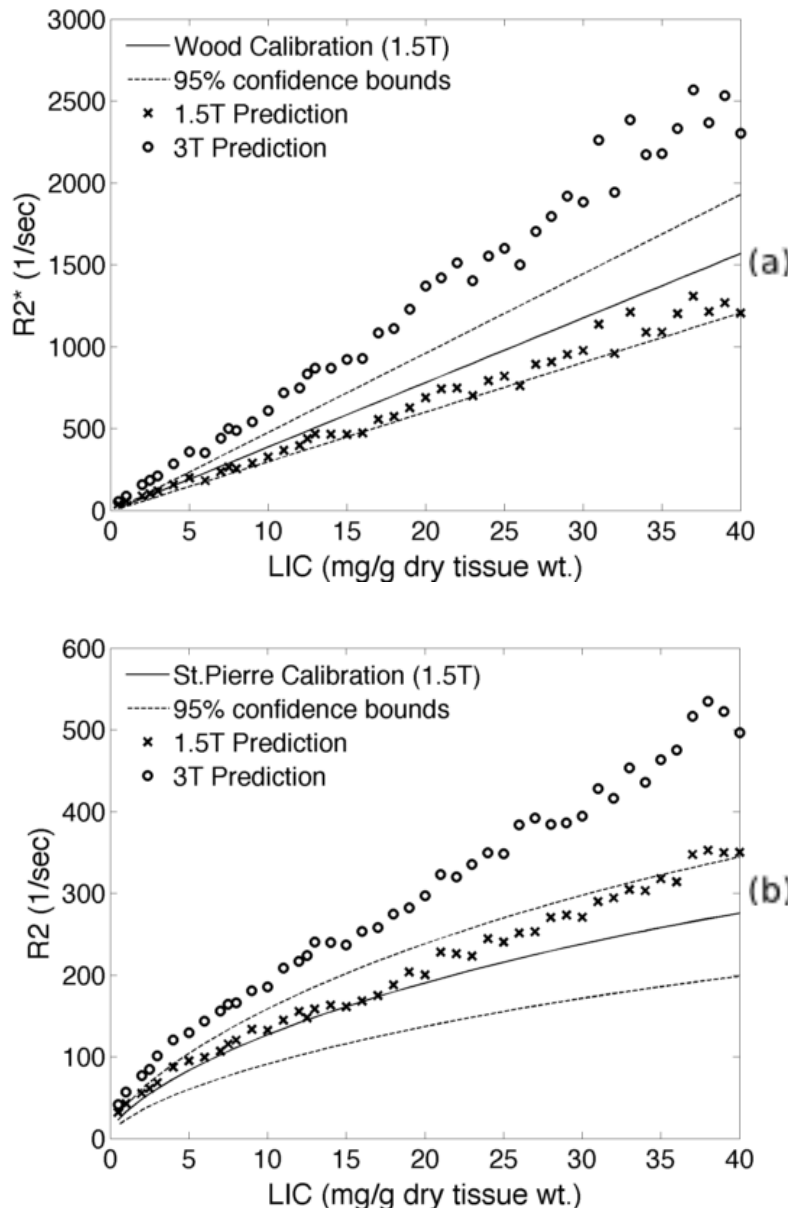


Figure 3.1: Comparison between simulated relaxivities (x) and clinical calibration curves at 1.5T for both $R2^*$ (a) and $R2$ (b). The clinical calibration curves are reproduced from the literature^{7,4}, and represent the behavior of *in vivo* patient data from large clinical trials. Simulated relaxivities at 3T(o) are included for comparison, although no corresponding clinical calibration curves exist. Note that the model predictions for $R2^*$ are highly linear and in agreement with the clinical calibration curves at 1.5T.

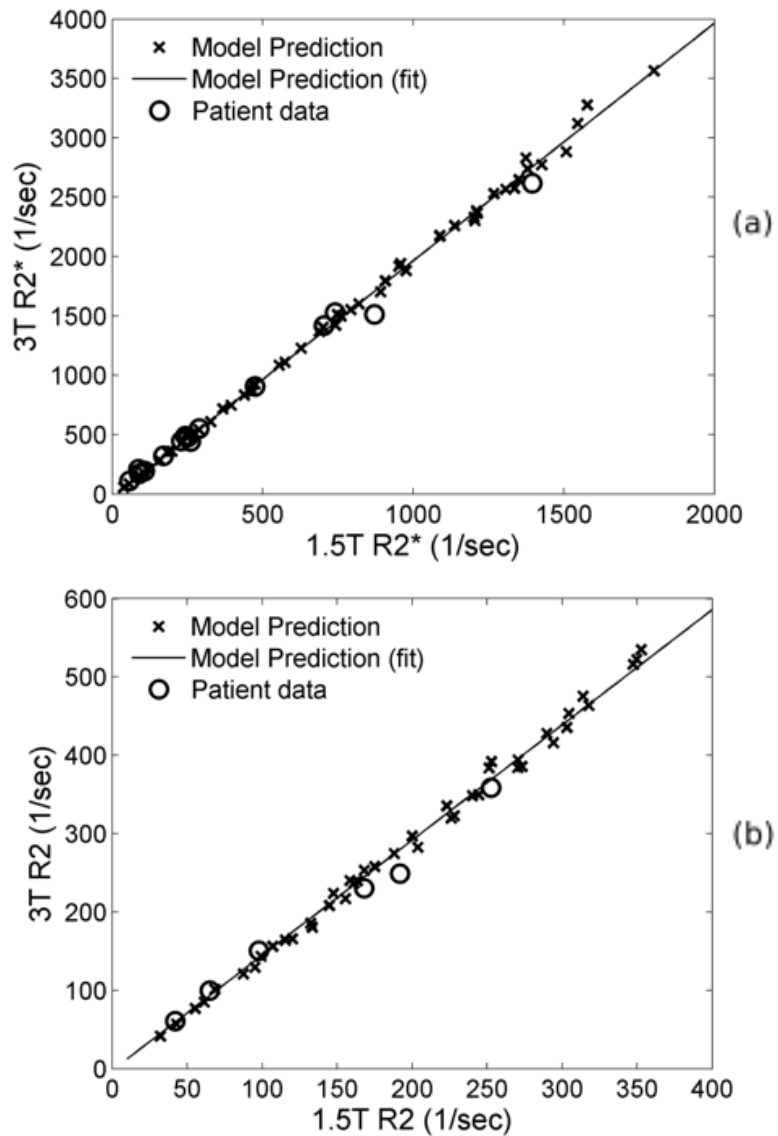


Figure 3.2: Relationship between relaxation rates at 3T and 1.5T. For both $R2^*$ (a) and $R2$ (b), model predictions (x) were highly linear ($R>0.99$) across field strength, and in good agreement with in vivo patient data (o).

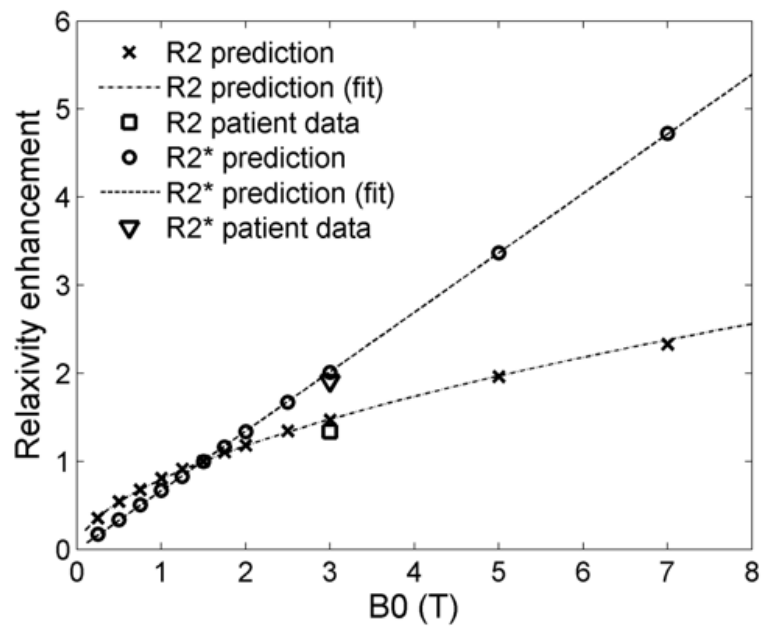


Figure 3.3: Enhancement of $R2^*$ and $R2$ relaxivities with field strength, relative to 1.5T. For $R2^*$, the predicted enhancement varied linearly with field strength, while it was curvilinear for $R2$. At 3T, the predicted relaxivity enhancements agree well with the values calculated from *in vivo* data.

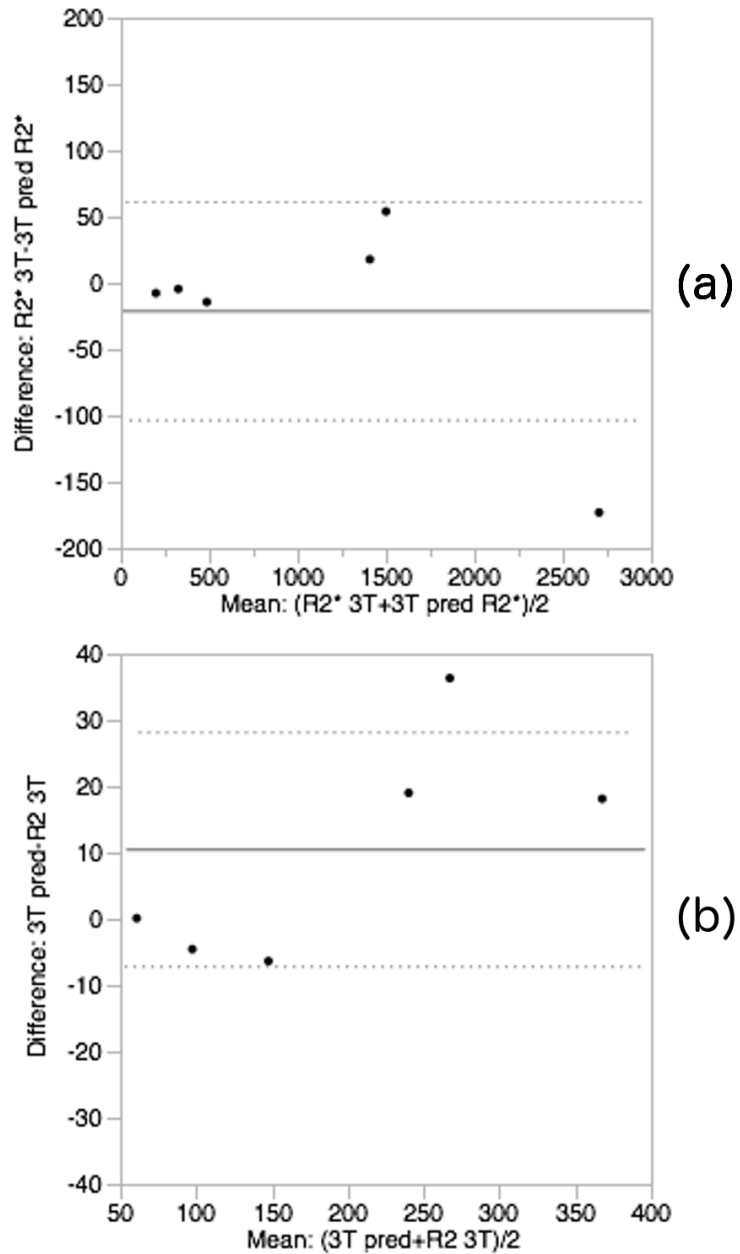


Figure 3.4: Bland-Altman plots between matched pairs of 3T simulated and patient data. (a) showed no significant bias and a standard deviation of 3.6%. (b) also showed no bias and a standard deviation of 7.2%.

Chapter 4

Spin Echo-Based Liver Iron Estimates Require B_1^+ Inhomogeneity

Abstract

4.0.1 Purpose

Magnetic resonance imaging is an important imaging modality to non-invasively assess liver iron. RF transmit (B_1^+) inhomogeneity is known to cause spatial intensity variation that can lead to quantitation errors. In this work, we assess the severity of B_1^+ inhomogeneity in patients at both 1.5 and 3 Tesla.

4.0.2 Methods

A patient study probed the mean and spatially-dependent excitation error in spin echo and gradient echo image series. A Monte Carlo simulation framework was used to quantify the R_2 ($1/T_2$) and R_2^* ($1/T_2^*$) decay rate errors resulting from a wide range of B_1^+ errors over the clinically-relevant range of liver iron loads.

4.0.3 Results

The patient study revealed that 1.5T and 3T both show significant spatial B_1^+ variation that varies between patients; 3T images also demonstrate underexcitation leading to over 30% error in achieved flip angle. Simulation results estimate that modest flip angle errors lead to significant R_2 estimate errors that may affect care and show disagreement with R_2^* -based iron estimates.

4.0.4 Conclusion

Voxel-wise error compensation in R_2 estimates is critical at 3T and will improve accuracy of iron estimates at 1.5T.

4.1 Introduction

Chronic anemias such as thalassemia and sickle cell disease represent the most common genetic disorders in the world. Transfusion therapy in these patients produces severe iron deposition in the liver and other organs, leading to cardiac and endocrine dysfunction and liver cirrhosis. Iron overload in transfusional siderosis cannot be treated with phlebotomy; instead, patients receive iron chelators that bind and remove iron with dosing specific to their tissue iron content, necessitating reliable iron quantitation techniques. Before 2005, needle biopsies were required to quantify liver iron, with their attendant risks²¹ and sampling error^{22,23,24}. Since then, magnetic resonance imaging systems have become key tools for diagnosing and monitoring iron overload disorders such as transfusional siderosis in sickle cell disease and thalassemia, hemochromatosis, liver disease, and a number of neurodegenerative disorders. Both transverse relaxivity and magnetic susceptibility

measurements have been used to estimate tissue iron concentrations in the liver, heart, endocrine glands, and brain.

MRI-based iron quantitation at 1.5 Tesla(T) is now standard of care⁷⁹ but iron quantitation in the liver using high-field scanners (3T and above) is limited by rapid signal decay and susceptibility artifacts. When increasing the field strength from 1.5T to 3T, field-dependent enhancement causes R_2^* ($1/T_2^*$) decay to double, leading to transverse decay below 0.5 ms in organs such as the liver, well below the range standard gradient-echo techniques can reliably quantify⁵⁸. Spin echo-based R_2 ($1/T_2$) estimates have shown potential to overcome these limitations at 3T and already see widespread use at 1.5T³⁶. However, spin echo estimates are more susceptible to spatially-varying excitation error (also called B_1^+ inhomogeneity) that lead to incorrect flip angles, a well-characterized imaging confounder in high field^{80,81}. Quantifying and correcting for this inhomogeneity could lead to more accurate liver iron concentration (LIC) estimates.

In this work, we measured B_1^+ scale inhomogeneity at 1.5T and 3T in patients over a broad range of iron burdens. The scale of the inhomogeneity was used to simulate the estimate error in R_2 -based LIC estimates at both field strengths using a Monte Carlo model. We demonstrate significant spatial B_1^+ scale inhomogeneity at both 1.5T and 3T and show that even modest B_1^+ scale error leads to clinically-relevant quantitation error across the physiologic LIC range.

4.2 Materials and Methods

4.2.1 Patient Population

Study participants were selected from a population of patients at the Children's Hospital of Los Angeles (CHLA), undergoing clinical treatment for iron

overload primarily resulting from transfusional treatment of sickle cell disease, thalassemia, and other rare anemia syndromes. Participants were recruited and provided informed consent to participate in an IRB-approved study (CHLA Study CCI-14-00034). Each participant received a clinically indicated MRI assessment for iron overload on the 1.5T scanner; a similar research protocol was completed at 3T.

4.2.2 Patient Assessment

Magnitude-only images were acquired on single-RF-transmit 1.5T and 3T clinical scanners (Philips Achieva, v3.2.2, Best, Netherlands) using 16-element SENSE-XL torso coils. Liver iron estimates were obtained at 1.5T using a 3-slice gradient echo acquisition with the following parameters: 16 echoes linearly spaced with TE/TR=0.96-11.47/50ms, FA=30°, matrix/voxel=72x67/1.25x1.25x10mm, BW=4409Hz/pixel. R_2^* estimates were made in hand-segmented regions of interest (ROI) in the liver and an exponential+constant model (see below) was fit to the data using Levenberg-Marquardt damped least squares minimization with software developed at CHLA in MATLAB (Mathworks, Natick, MA); LIC estimates are made using a R_2^* -LIC calibration curve derived from biopsy⁴. The signal model chosen was:

$$S(t) = S_0 e^{-R_2^* t} + c \quad (4.1)$$

where $S(t)$ represent echo intensity at each echo time t , S_0 represents signal intensity at $t=0$, R_2^* represents relaxation rate, and c represents noise bias.

B_1^+ maps represented in B_1^+ scale ($100 * [B_1^+ \text{ achieved} / B_1^+ \text{ desired}] \%$) were obtained at 1.5T and 3T in a single slice using a dual repetition time (TR) B_1^+ mapping

sequence⁸² with TE/TR₁/TR₂ =3ms/20ms/120ms, bandwidth of 2894Hz/pixel, voxel size of 4.2x4.2x8 mm³, and one signal average. A second set of B₁⁺ maps were obtained at both fields using an echo time of one millisecond to ensure that we could sample severely iron loaded patients who demonstrate particularly rapid T₂^{*} decay.

The maps were manually segmented to quantify the B₁⁺ scale inhomogeneity found in an iron overloaded patient population. B₁⁺ maps were assessed for dependence on patient weight, BMI, and clinical iron-load. Aggregate patient B₁⁺ maps were averaged by non-rigidly warping individual maps to a canonical liver shape. Because of imperfect registration, some pixels in the canonical liver shape received contributions from <5 patients and were excluded; each pixel was properly weighted according to the number of contributing patients. The canonical B₁⁺ maps were used to estimate spatial statistics in the right and left lobe.

B₁⁺ maps were validated in a phantom (0-16 mM MnCl₂ vials in a 0.5 mM MnCl₂ bath) with transverse decay rates as low as 1.7 ms prior to use in patients to ensure that the B₁⁺ map had sufficient dynamic range to reliably map the patient population.

4.2.3 Simulation

An internally developed simulation framework written in MATLAB was used to create physiologically realistic liver iron geometries in-silico over a range of 1-50 mg/g (mg-iron/g-dry tissue weight). A detailed description of this model may be found in previous reports^{58,68,57}. Briefly, liver tissue was modeled as 80 μm cubes of liver tissue containing 64 cuboidal hepatocytes and 18 cylindrical sinusoid regions⁶⁸. Iron overload was modeled by distributing spheres of iron in the hepatocytes using Gamma statistical distributions describing sphere size and spacing.

From the iron distributions, magnetic field disturbances were calculated based on the field strength and magnetic susceptibility of iron⁶⁸. Simulated protons were then diffused through the geometries using a random walk simulation obeying cell boundaries.

The first version of the simulation framework assumed perfect excitation and refocusing, ignored pulse bandwidth, and did not model longitudinal magnetization or T_1 decay. To model B_1^+ scale inhomogeneities, we implemented a full Bloch simulator to calculate the 3D magnetization of each proton at every time step. The simulations calculated rotations from instantaneous excitation and inversion pulses, realistic iron-free T_2/T_1 relaxation rates of 42ms/812ms at 3T and 50ms/576ms at 1.5T⁵⁹, and the iron-based phase accrual from the proton's random walk at each 0.05 μ s time step. Iron-dependent T_1 changes were ignored due to minimal longitudinal recovery over the duration of the echo trains simulated and lack of multiple TRs. Excitations and inversions were modeled as instantaneous pulses and achieved angles were scaled by B_1^+ scale for each simulation. For example, a 90_x - 180_y single spin echo sequence with 90% excitation efficiency would be simulated with an excitation pulse of 81° about x and an inversion pulse of 162° about y .

Signals from 2500 separate spin cohorts were superposed to form a transverse signal for each combination of iron load and B_1^+ scale. Simulations varied B_1^+ scale from 53% to 127% in single echo and CPMG multiecho spin echo experiments with 90° excitations and 180° inversions; spin echo and CPMG echo times were [1.70,2.56,3.86,5.82,8.76,13.2,19.9,30.0] ms and [2.0,4.0,6.0,8.0,10,12,14,16,18,20] ms, respectively. A complex signal model with a non-negativity constraint on R_2 was fit to transverse signals to estimate the R_2 relaxation rate of each sample. R_2 as a function of LIC was determined for each simulated B_1^+ scale by fitting

individual results to a 2nd order polynomial to capture the nonlinearity of the behavior.

4.2.4 Software

A historical repository containing snapshots of simulation specification files, analysis code, and simulation framework, and SHA IDs for sub-repositories may be found at:

https://github.com/cornercase/snapshot_research_b1_liver_iron
Revision SHA ID: 7858e34557fc5059f50adf311f12af5d464ce337
DOI: 10.5281/zenodo.155955

An actively developed repository containing the simulation framework is available at:

<https://github.com/cornercase/IronBloch>

4.3 Results

B_1^+ maps were acquired in 47 subjects (19M, 28F, 29.9 ± 11.6 years of age, 19 β -Thalassemia, 21 Sickle Cell, 7 other rare anemia, LIC=0.2-41.5 mg/g). Mean B_1^+ scale was found to be uncorrelated with BMI and weight at 1.5T and showed weak, negative correlation at 3T (see Table 4.1). Figure 4.1 demonstrates B_1^+ inhomogeneity in the liver at 1.5T and 3T from nine representative subjects. At 3T, mean B_1^+ scale was low and the standard deviation was high ($69.6\% \pm 14.6\%$). Statistics are summarized in table 4.1. Excitation efficiency was significantly higher in the right lobe than the left lobe (right mean=73.6%, left mean=62.1%) but there was considerable inter-subject variability. Mean achieved B_1^+ scale was independent of liver iron burden (1.5T: $r^2 = 0.047$, $p=0.143$; 3T: $r^2 = 0.051$, $p=0.127$). Both

the spatial homogeneity and the mean achieved B_1^+ scale ($99.3\% \pm 12.3\%$) were better at 1.5T compared to 3T; right and left lobe means were 103.3% and 92.0% respectively. The phantom study (results not included) confirmed that the specified dual TR method had sufficient dynamic range to capture the highest expected physiologic decay rate; the off-resonance effects of iron could not be replicated.

Simulations were performed examining the impact of B_1^+ inhomogeneity on free induction decay R_2^* estimates, multiple single echo R_2 estimates (Figure 4.2), and CPMG multiecho R_2 estimates (Figure 4.3). The R_2^* iron calibration was robust to B_1^+ errors (not shown); no change in R_2^* -LIC calibration was detectable. Spin echo simulations demonstrate that calibration error increases significantly with B_1^+ deviation above physiologic iron loads in both single-echo and CPMG sequences. Multi-echo calibrations were more stable over B_1^+ scale errors of $\pm 20\%$ but demonstrated a larger proportional B_1^+ effect than the single echo calibration for extreme B_1^+ error in moderate to high iron loads. Uncorrected B_1^+ inhomogeneity in single echo experiments cause systematic overestimation of R_2 in patients at 1.5T, though the effect is less pronounced for small values of inhomogeneity at high iron loads. Single echo R_2 estimates at 3T produce a less pronounced overestimation up to 25 mg/g of iron; B_1^+ scale error causes R_2 estimates to fall dramatically in higher iron burdens. CPMG sequences show a slight underestimation of R_2 at below 5 mg/g and a systematic overestimation of R_2 above 5 mg/g . Figure 4.2 and Figure 4.3 demonstrate near-symmetry about 100% flip angle efficiency, indicating equivalent effects of over and under excitation.

4.4 Discussion

This is the first study to examine the magnitude of B_1^+ excitation efficiency in the liver and its potential impact on clinical liver iron estimates. At 1.5T, full average excitation was achieved in the liver but variation between right and left lobes was 12%. Significantly larger B_1^+ inhomogeneities were observed in the liver at 3T. We had postulated a potential iron effect because B_0 and B_1^+ inhomogeneities can interact⁸². Because off-resonance from liver iron can exceed 1000 Hz, we expected that the excitation bandwidth for standard B_1^+ mapping sequences would be too narrow, though the phantom study demonstrated a sufficiently short TE. Further, off-resonance can cause slice misplacement. In spite of this, excitation efficiency was uncorrelated with liver iron and manual evaluation of the images did not indicate that slices were meaningfully shifted. At 3T, we observed an unexpected systematic underexcitation in the liver, averaging just 69.6% of our specified flip angle in whole-liver ROIs. The effect was not observed at 1.5T. A wide range of iron loads was observed, making it unlikely that we have shown incomplete excitation at 3T resulting from doubling of off-resonance effects relative to 1.5T. The underexcitation was seen in normal controls, leading us to speculate that incomplete excitation is due to aggressive specific absorption rate (SAR) models. Manual increases of the transmit gain improved whole-ROI average B_1^+ scale to near 100% at 3T, though the observed spatial inhomogeneity remained.

In single echo simulations (Figure 4.2), the estimate error appears to be primarily dependent on decay rate rather than field strength. The overestimation of liver R_2 occurs up to 200-250 s⁻¹ in both 1.5T and 3T simulation, representing approximate LIC burdens of 30 and 15 mg/g respectively. For this range of iron burdens, the apparent R_2 decay increases with B_1^+ scale error as reduction in amplitude of the later echoes prematurely pulls the fit decay curve down. At decay rates over 250 s⁻¹

in both 1.5T and 3T simulations, the amplitude of the early echoes is significantly reduced as well. The correspondingly flat decay curves lead to a reduction in R_2 estimate. Although this effect is less apparent in the 1.5T simulation, reduction in R_2 is visible for iron loads over 40 mg/g and is more notable for higher B_1^+ error. The significant decrease in R_2 estimates is clear at 3T for moderate-to-high iron burdens. In cases of moderate-to-fast decay, the underexcitation may cause the first echo to appear substantially darker; this may lead observers to overestimate iron burden due to the loss of signal intensity even though the iron is not exclusively responsible for diminished signal intensity.

For CPMG simulation estimates (Figure 4.3), the phase cycling of the echo pulses leads to “saw-toothing” that envelopes the true decay curve: the odd echoes have lower amplitudes than subsequent even echoes. For smaller B_1^+ scale errors, the error is mostly self-correcting. As B_1^+ becomes large, a significant portion of the longitudinal magnetization remains after the excitation pulse and is recovered into the transverse plane when echo pulses are applied; similarly, transverse magnetization is stored in the longitudinal plane when incomplete echo pulses are applied. The saw-toothing eventually increases such that the first echo amplitude is smaller than all of the even echoes, even for very high LIC burdens; the resulting fits show reduced R_2 estimates. The differing behavior of the 1.5T and 3T calibration curves in the presence of B_1^+ scale error over 27% is primarily a T_1 effect. The longer T_1 at 3T compared to 1.5T causes less longitudinal magnetization recovery, leading to a less pronounced addition of transverse signal over the course of the echo train. Later echoes at 3T therefore demonstrate more realistic decay than 1.5T echoes in the presence of large B_1^+ inhomogeneity. Nonetheless, the inclusion of longitudinal magnetization and diminished first echo intensity lead to the apparent reduction of R_2 for high iron loads in the presence of large B_1^+ error.

The patient study demonstrated that B_1^+ spatial inhomogeneity and error in mean whole-liver flip angle were much smaller at 1.5T than 3T. Nonetheless, a 10% error in achieved flip angle in a patient with an LIC of 10 mg/g increases the predicted LIC by 30%. While a difference between 10 mg/g and 13 mg/g does not markedly change that patient's risk assessment, consistent with the widespread use of 1.5T R_2 techniques in clinical practice⁴, B_1^+ inhomogeneity probably worsens the agreement between LIC values estimated by R_2^* and by R_2 ^{79,83} by adding patient-specific errors to the R_2 estimate without affecting R_2^* . B_1^+ variation could also contribute to the observed curvilinearity in the R_2 -iron calibration curve⁷. With perfect excitation, the R_2 -iron relationship is relatively linear over a wide range of LIC's but even mild B_1^+ errors introduce marked concavity to the calibration curve. B_1^+ inhomogeneity could also potentially confound techniques that rely on proton-density estimators to stabilize LIC measurements at high iron concentrations. Carefully controlled studies are warranted to determine whether B_1^+ correction could improve R_2 LIC measurements at 1.5 Tesla.

In contrast, correcting B_1^+ inhomogeneity is an absolute necessity for R_2 -based iron estimation at 3T. Eliminating the observed mean underexcitation of the liver at 3T, even in the presence of the spatial flip angle variation, would immediately improve iron estimates using existing fitting techniques. RF shimming using multi-transmit RF systems or updates to transmit gain selection algorithms may help to improve the observed underexcitation and spatial variation. Adiabatic pulses cannot be used in this context because their long duration precludes the short echo times necessary to measure signals in high iron load subjects. Further, many adiabatic pulses demonstrate significant dependence on off-resonance which will not be known a priori in iron overloaded patients. When B_1^+ homogeneity cannot be improved, manual or automatic exclusion of voxels experiencing over $\pm 25\%$ B_1^+

excitation error would improve LIC estimates. It is especially important when performing iron estimation using multiple small ROIs because sampling of regions in the far right and far left lobes in an attempt to sample the whole liver will lead to significant estimate error. It may also be possible to apply voxel-wise corrections to echo amplitudes based on acquired B_1^+ maps or fit to a signal model that considers the effects of B_1^+ , though T_1 or R_2^* effects may vary with iron load, thus necessitating an iterative approach. The success of the simulation framework in this context would allow for patient-specific corrections to be developed and potentially allow for bespoke excitation pulses to be developed in near-real-time.

4.5 Conclusions

Patient results demonstrate that significant whole-liver underexcitation is observed at 3T and spatial flip angle variation is observed at both 1.5T and 3T. Simulation results demonstrate that B_1^+ effects can cause systematic liver R_2 estimation error up to 30% at 1.5T; error worsens significantly at 3T. To ensure accurate diagnosis and treatment of these patients, B_1^+ mapping is essential for error compensation at 3T. Passive voxel-wise corrective measures such as voxel exclusion or numerical correction should be applied over 25% B_1^+ excitation error. If available, measures like RF shimming may actively correct B_1^+ error. Further simulations and signal modelling will be performed to better understand the effect of very high levels of B_1^+ inhomogeneity on liver iron estimates and develop correction schemes to improve R_2 estimates.

Field	Whole (mean %±std)	Left (mean %)	Right (mean %)	B_1^+ Scale vs Weight Correlation (r^2)	B_1^+ Scale vs BMI Correlation (r^2)
1.5T	99.3±12.3	92.0	103.3	0.0043 (p=0.66)	0.0092 (p=0.52)
3.0T	69.6±14.6	62.1	73.6	0.20 (p=0.0016)	0.11 (p=0.024)]

Table 4.1: B_1^+ mean scale values in the whole liver and right and left lobes show that image series from both 1.5T and 3.0T MRI scanners demonstrate significant spatial variation in B_1^+ scale. Further, 3.0T images demonstrate significant mean underexcitation. The mean excitation did not correlate with BMI or weight in 1.5T studies. Underexcitation was weakly associated with weight and BMI at 3T.

4.6 Acknowledgements

This research is supported by the National Institute of Diabetes, Digestion and Kidney Diseases of the National Institutes of Health, grant 1R01DK097115-01A1. Computation for the work described in this paper was supported by the University of Southern California’s Center for High-Performance Computing (hpc.usc.edu).

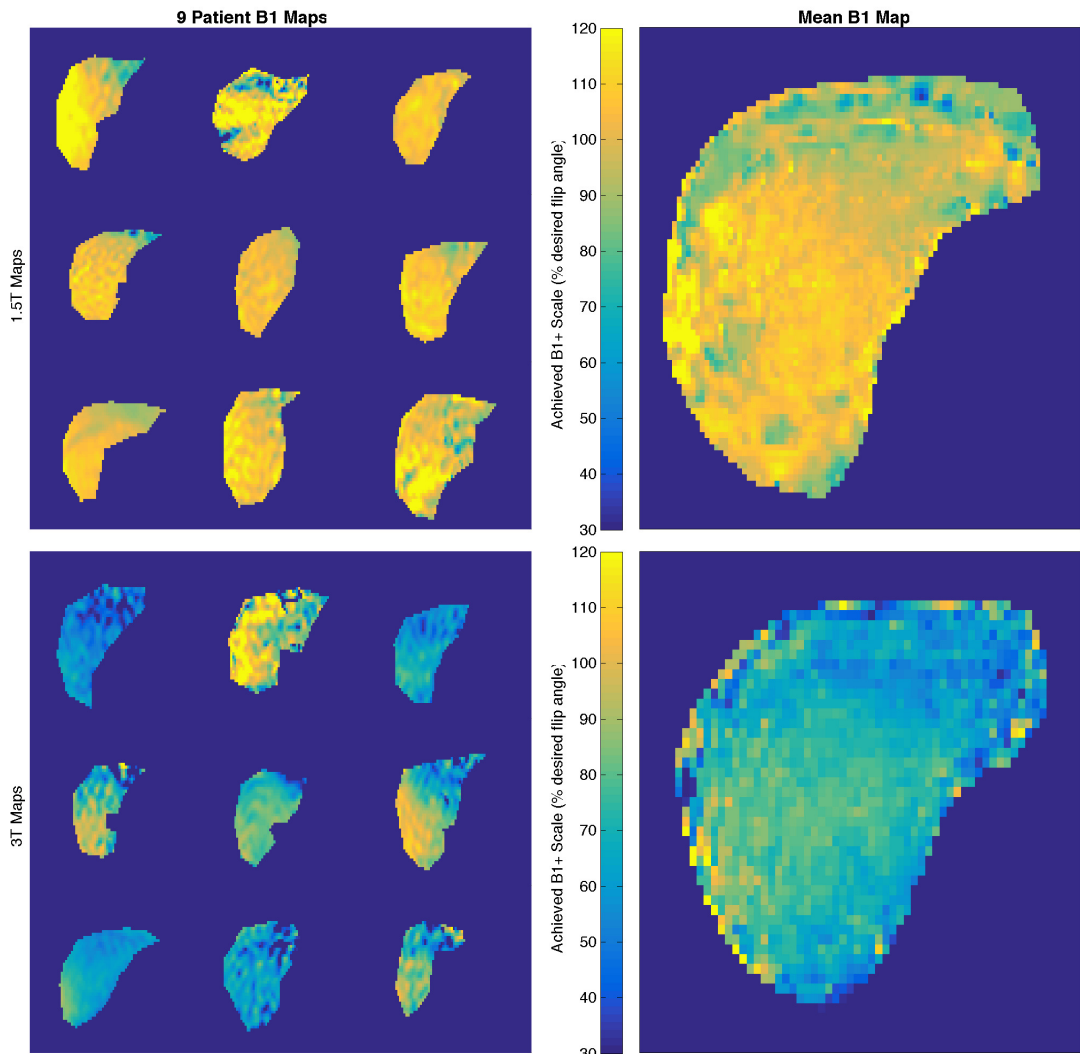


Figure 4.1: Spatial maps of B_1^+ scale in patients demonstrate significantly different behavior at 1.5T and 3T. 1.5T maps demonstrate largely uniform excitation patterns and consistently complete excitation. 3T maps demonstrate significant spatial variation in B_1^+ as well as a mean achieved B_1^+ of only 69.6%.

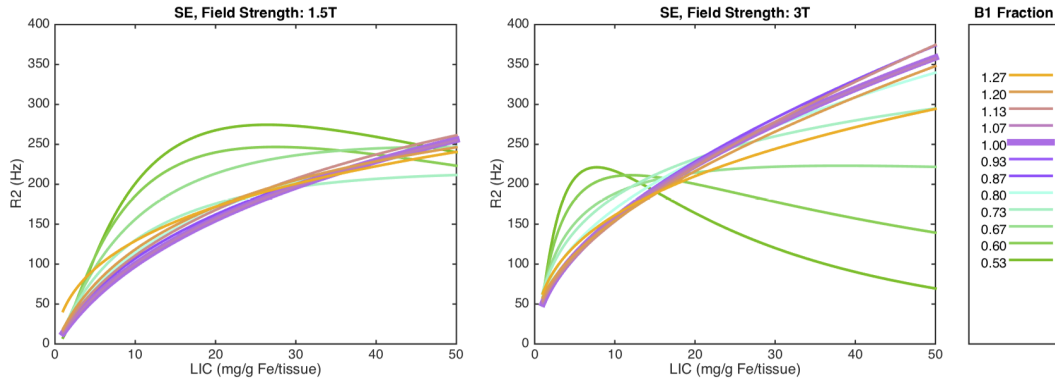


Figure 4.2: Single echo simulations over a wide range of iron loads and B_1^+ inhomogeneities demonstrate that iron is overestimated in the presence of B_1^+ inhomogeneity at 1.5T. Further, inaccuracies increase with iron load for a given B_1^+ . Although 1.5T R_2 estimates tend to increase with B_1^+ variation, 3T maps show the opposite effect due the combination of fast initial decay and lengthened T_1 resulting in artificially flat decay curves. (B_1^+ Fraction = B_1^+ Scale/100)

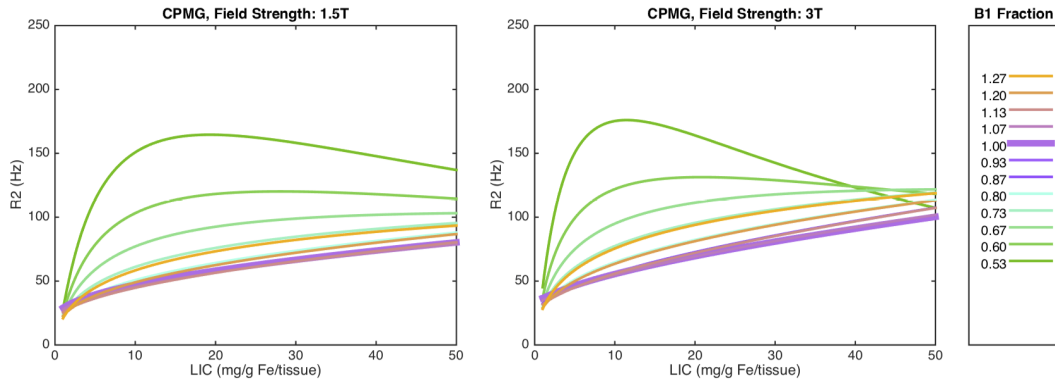


Figure 4.3: CPMG simulations over a wide range of iron loads and B_1^+ inhomogeneities demonstrates that iron is overestimated in the presence of B_1^+ inhomogeneity except with low iron loads at high B_1^+ inhomogeneities. (B_1^+ Fraction = B_1^+ Scale/100)

Chapter 5

Ultra-Short Echo Time Images Quantify High Liver Iron

ABSTRACT

5.0.1 Purpose:

1.5T gradient echo-based R_2^* estimates are standard-of-care for assessing liver iron concentration(LIC). Despite growing popularity of 3T, echo time (TE) limitations prevent 3T liver iron quantitation in the upper half of the clinical range($LIC \gtrapprox 20^{\text{mg/g}}$). In this work, a 3D radial pulse sequence was assessed to double the dynamic range of 3T LIC estimates.

5.0.2 Theory and Methods:

The minimum TE limits the dynamic range of pulse sequences to estimate R_2^* . 23 chronically-transfused human volunteers were imaged with 1.5T cartesian gradient echo(1.5T-GRE), 3T cartesian gradient echo(3T-GRE), and 3T ultrashort TE radial(3T-UTE) pulse sequences; minimum TEs were 0.96, 0.76, and 0.19 ms, respectively. R_2^* was estimated with an exponential signal model, normalized to 1.5T equivalents, and converted to LIC. Bland-Altman analysis compared 3T-based estimates to 1.5T-GRE.

5.0.3 Results:

LIC by 3T-GRE was unbiased versus 1.5T-GRE for $LIC \leq 25^{\text{mg/g}}$ ($sd=9.6\%$); 3T-GRE failed to quantify $LIC > 25^{\text{mg/g}}$. At high iron loads, 3T-UTE was unbiased ($sd=14.5\%$) compared to 1.5T-GRE. Further, 3T-UTE estimated LIC up to $50^{\text{mg/g}}$, exceeding 1.5T-GRE limits.

5.0.4 Conclusion

3T-UTE imaging can reliably estimate high liver iron burdens. In conjunction with 3T-GRE, 3T-UTE allows clinical LIC estimation across a wide range of liver iron loads.

5.1 Introduction

Chronic anemias such as thalassemia and sickle cell disease represent the most common genetic disorders in the world. Transfusion therapy in these patients produces severe iron deposition in the liver and other organs, leading to cardiac and endocrine dysfunction as well as liver cirrhosis. Iron overload in transfusional siderosis cannot be treated with phlebotomy; instead, patients receive iron chelators that bind and remove iron. Dosing must be adjusted based on tissue iron content, necessitating reliable iron quantitation techniques. Before 2005, needle biopsies were required to measure liver iron, with their attendant risks²¹ and sampling error^{22,23,24}. Since then, magnetic resonance imaging systems have become important tools for diagnosing and monitoring iron overload disorders including sickle cell disease, thalassemia, hemochromatosis, and neurodegenerative disorders^{4,84}. Both transverse relaxivity and magnetic susceptibility measurements have been

used to estimate tissue iron concentrations in the liver, heart, endocrine glands, and brain.

MRI-based iron quantitation at 1.5 Tesla(T) is now standard of care⁷⁹. However, it is estimated that 50% of new magnet installations are 3T and some imaging centers use exclusively 3T magnets; this necessitates development of robust imaging techniques for high-field systems. Previous studies have validated quantitation over lower iron burdens at 3T^{72,60,85}. However, liver iron quantitation with high-field scanners (3T and above) remains limited by rapid signal decay. When increasing the field strength from 1.5T to 3T, field-dependent enhancement causes R_2^* ($1/T_2^*$) decay to approximately double, leading to transverse decay times below 0.5 ms in the liver, well below the range standard gradient-echo techniques can reliably capture⁵⁸. Inadequate sampling of rapidly decaying signal components leads to an underestimate of liver iron concentration (LIC). The development of ultra-short echo time (UTE) sequences has dramatically decreased the minimum achievable echo time (TE), enabling acquisition of ultra-fast decay species⁸⁶. UTE has shown promise to perform structural imaging of cartilage and bone. The reduced TE could potentially lead to significantly increased dynamic range in quantitative imaging approaches used to non-invasively estimate LIC at 3T and above.

In this work, we measured liver R_2^* in human volunteers receiving treatment for transfusional iron overload using cartesian gradient echo (GRE) and UTE sequences. We obtained 3T LIC estimates in milligrams of iron per gram of dry liver (mg/g) for comparison with clinical LIC estimates obtained at 1.5T using a previously derived relationship between liver R_2^* at 1.5T and 3T⁵⁸. We demonstrate that 3D radial UTE imaging increased the achievable dynamic range of LIC estimates to match, and possibly exceed, estimates from cartesian gradient echo

images obtained at 1.5T, providing a reliable means to quantify high liver iron at 3T.

5.2 Methods

5.2.1 Participant Population

Study participants were selected from a population of patients at the Children’s Hospital of Los Angeles (CHLA) undergoing chronic transfusion therapy for sickle cell disease, thalassemia, and other rare anemia syndromes. Participants provided informed consent to participate in an IRB-approved study (CHLA Study CCI-14-00034). Each participant received a clinically indicated MRI assessment for iron overload on a 1.5T scanner followed by a research imaging protocol at 3T. Imaging data from a repeat clinical visit was available for a single participant and was weighted proportionally in resulting statistics.

Participant Assessment

Images were acquired on single-RF-transmit Philips Achieva 1.5T and 3T clinical scanners (software revision v3.2.2 or v5.1.7, Philips HealthTech, Best, Netherlands) using 16-element SENSE-XL torso coils. Clinical liver iron estimates were obtained from 1.5T R_2^* estimates using a 3-slice gradient echo acquisition, henceforth referred to as 1.5T-GRE. Two series - a 16-echo Cartesian gradient echo series (3T-GRE) and a set of seven single-echo, center-out, stack-of-stars, 3D radial images with varying echo times (3T-UTE) - were acquired at 3T. Compared to cartesian gradient echo, center-out radial trajectories facilitate significantly reduced echo times by beginning readout from the center of k-space; the removal of the dephasing gradient prior to readout allows the echo to be acquired

more quickly after excitation. 3T-UTE echo times were selected with approximate log spacing to maximize dynamic range. The minimum echo time of 0.19 ms was selected to facilitate quantitation of LIC $\geq 60^{\text{mg/g}}$; other scan parameters including gradient strength and slice thickness were selected to permit the shortest echo time. Relevant sequence parameters for all series are available in Table 5.1. All images were reconstructed on-scanner; the default reconstruction was used for 1.5T-GRE and 3T-GRE series while 3T-UTE images were reconstructed with the Philips SENSE implementation without undersampling. Clinical and research liver R_2^* estimates were made pixelwise in hand-segmented regions of interest (ROI) encompassing the whole liver but avoiding large vasculature and biliary structures. R_2^* estimates were made by fitting an exponential+constant ($\text{exp}+c$) model (see equation 5.1) to the data using Levenberg-Marquardt least squares minimization with previously-validated software developed at CHLA in MATLAB (Mathworks, Natick, MA)⁶⁰. The $\text{exp}+c$ signal model, which was used to fit 1.5T-GRE, 3T-GRE, and 3T-UTE data, is as follows:

$$S(t) = S_0 e^{-R_2^* t} + c \quad (5.1)$$

where $S(t)$ represents echo intensity at each echo time t , S_0 represents signal intensity at $t = 0$, R_2^* represents relaxation rate, and c represents noise bias and contributions from slow-decay species. The fitting model was chosen for all scans to allow for comparison of the 3T-UTE technique with our existing, clinically-established analysis toolbox⁶⁰. R_2^* estimates obtained at 3T were converted to 1.5T R_2^* equivalents using a previously-derived relationship⁵⁸:

$$R(Y) - R_{iY} = (R(1.5T) - R_{i1.5T}) * E_R(Y) \quad (5.2)$$

$$E_{R_2^*}(B_0) = -0.0086 + 0.68 * B_0 \quad (5.3)$$

where $R(Y)$ represents the relaxation rate R_2^* at a given field strength Y , R_{iY} represents the relaxation rate for normal liver at field strength Y , $E_R(Y)$ represents the relaxation rate enhancement for R_2^* from $1.5T$ to field strength $Y = B_0$ given by $E_{R_2^*}(B_0)$. Normal liver R_2^* values for $1.5T$ and $3T$ were assumed to be 31.1 Hz and 44.4 Hz, respectively, based on internally derived estimates from healthy controls. These values, derived from a young cohort of patients, are similar to but slightly lower than previously published values derived in adults⁷²; this disagreement is expected based on the difference in age between the subject populations and the known increase in liver iron accumulation with age^{87,31}.

All LIC estimates were made using the $1.5T$ R_2^* -LIC calibration curve derived from biopsy⁴. Bland-Altman analysis comparing $1.5T$ -GRE LIC estimates with $3T$ -UTE and $3T$ -GRE LIC estimates was performed; based on the expected failure of $3T$ -GRE techniques at high iron burdens, participants were assessed in two separate cohorts: $LIC \leq 25^{mg/g}$ and $LIC > 25^{mg/g}$.

Phantom

R_2^* estimates were validated in a phantom ($0-24$ mM $MnCl_2$ vials in a 0.25 mM $MnCl_2$ bath) constructed of $\frac{1}{4}$ "-plexiglass sheet measuring $16.5'' \times 12.5'' \times 7.5''$. 100 -mL Nalgene vials containing (0.0 , 0.5 , 0.75 , 1.0 , 1.5 , 2.0 , 2.5 , 3.5 , 5.0 , 8.0 , 12.0 , 16.0 , 24.0) mM $MnCl_2$ were suspended on the center line along the longest dimension or offset $2.25''$ laterally from the center line. Vials were staggered in a honeycomb layout to reduce inter-vial susceptibility effects. The phantom was imaged at $3T$ with the $3T$ -GRE and $3T$ -UTE protocols.

Simulation

A simulation evaluating the effects of proton-density fat fraction (PDFF) on exp+c-derived LIC estimates was conducted. Signals were simulated by superposing water and a 6-peak fat model⁸⁸ with PDFFs of 0%, 5%, 10%, and 20%. Decay was simulated as a mono-exponential and decay rates were calculated from a previously-derived LIC- R_2^* relationship^{4,58} up to 45^{mg/g}. Noise was added to match an approximate first-echo SNR of 40 for images obtained in a normal liver. Signals for each LIC-PDFF combination were simulated 20 times to provide pixelwise-like data and sampled at TEs matching the 3T-UTE and 3T-GRE protocols. Samples were fit using the same exp+c technique as imaging data, pixelwise-like-LIC estimates were averaged, and the resulting LIC error was determined.

Software

A historical repository containing snapshots of relevant code can be found at https://github.com/cornercase/snapshot_research_ute_vs_gre_LIC/releases/tag/v1.1

or via it's DOI: 10.5281/zenodo.570291.⁸⁹

RESULTS

Phantom

Analysis of phantom results (figure 5.1) demonstrated that the 3T-UTE and 3T-GRE protocols successfully quantified R_2^* up to 2830 Hz and 1910 Hz, respectively, equivalent to LICs of 35.8^{mg/g} and 24.4^{mg/g}. The 3T-GRE results demonstrated catastrophic failure in the highest concentration vial, showing saturation

of R_2^* rather than the expected linear increase; the sample was excluded from analysis. No saturation was observed in the UTE data. Linear regression of 3T-UTE data gave the following relationship: $R_2^*_{3T-UTE} = 117 \times [\text{mM MnCl}_2] + 1.6$ ($r^2 = 0.996$, $r_{adj}^2 = 0.995$). Regression of 3T-GRE results demonstrated a similar linear relationship: $R_2^*_{3T-GRE} = 120 \times [\text{mM MnCl}_2] + 3.5$ ($r^2 = 0.999$, $r_{adj}^2 = 0.999$). The regressions show less than 3% disagreement in the slope of the R_2^* -MnCl₂ relationship.

5.2.2 Participant

A set of 24 imaging series were gathered from 23 participants (11M/12F, 21.5 ± 12.0 years, 11 Thalassemia Major, 8 Sickle Cell Disease, 4 other rare anemia, LIC=1.9-40.7 mg/g); additional demographic information is summarized in table 5.2. Subjects were generally lean, had a broad range of iron overload, and had mild transaminitis.

Figure 5.3 demonstrates the scatter plot of LIC estimates measured with 3T-UTE and 3T-GRE compared with LIC estimates from 1.5T-GRE; a line of unity is displayed for reference. The 3T-GRE data (represented by **X**) track the unity line until LIC exceeds 22^{mg/g} ($R_2^* \approx 1750$ Hz) and then plateau, similar to the plateau demonstrated by 24 mM MnCl₂ in figure 5.1. In contrast, LIC by 3T-UTE (represented by **O**) tracks the unity line up to 40 mg/g. For some clinical iron estimates near 40^{mg/g}, the approximate upper limit of the 1.5T protocol, 3T-UTE produces higher iron estimates than 1.5T-GRE (see shaded region, figures 5.3&5.5).

The agreement between cartesian GRE measurements at 3T and 1.5T is summarized by Bland Altman analysis (figure 5.4). For subjects with clinical LIC ≤ 25 ^{mg/g} (represented by **●**), the 1.5T-GRE and 3T-GRE are unbiased with

respect to each other with a standard deviation of 9.6%. Participants with $LIC > 25^{\text{mg/g}}$ (represented by) demonstrated large bias ($37.3\% \pm 9.8$). The failure of 3T-GRE fits at high iron loads causes LIC by 3T-GRE to be uncorrelated with LIC by 1.5T-GRE, causing the bias to grow with the average of the two LIC estimates.

Figure 5.5 demonstrates the Bland Altman relationship between LIC derived from 3T-UTE versus 1.5T-GRE. For $LIC > 25^{\text{mg/g}}$, 3T-UTE LIC estimates were unbiased with a standard deviation of 14.5%. For lower LIC values, UTE overestimated LIC compared to 1.5T-GRE by an average of $15.7\% \pm 21.9\%$.

Simulation

Simulation results demonstrated that physiologic amounts of liver fat cause estimates of LIC by 3T-UTE to overestimate liver iron compared to 3T-GRE. 3T-UTE error grows with PDFF but is relatively stable across iron loads above $5^{\text{mg/g}}$. after an initial over-estimate of liver iron. Below $5^{\text{mg/g}}$, error in LIC by 3T-UTE grows for all PDFFs, suggesting the maximum echo is too short for the 3T-UTE protocol to reliably quantify slow decay in the presence of noise, similar to the bias demonstrated in 5.5. In contrast, the 3T-GRE protocol is relatively robust to fat effects until the signal decay approaches the upper limit of the dynamic range. Approaching the upper range limit, LIC by 3T-GRE overestimates LIC by up to 6% before failing. Results are further summarized in a supplemental figure.

DISCUSSION

Rapid decay rates have remained a persistent challenge for estimating high liver iron loads at 3T and higher field strengths. Although iron quantitation in the

heart and liver have been reported at 3T^{90,91}, this is the first study to match the dynamic range of 1.5T-GRE sequences. Our existing 3T-GRE techniques offered excellent robustness up to 20-25^{mg/g}, though the exact limit is scanner-dependent due to differing software options that limit echo spacing and first echo timing and hardware limitations such as coil blanking intervals and noise characteristics. The UTE protocol in this study was specifically designed to supplement an existing clinical quantitation workflow rather than replace it in order to maximize adoptability and permit the use of existing clinical tools without the need for algorithm or workflow changes. Both the phantom data (figure 5.1) and the human data (fig 5.3-5.5) suggest that the 3T-UTE can quantify R_2^* up to an LIC equivalent of $\geq 40^{mg/g}$. UTE therefore nearly doubles the range of iron compared to the 1900 Hz ($LIC \approx 24^{mg/g}$) limit of our 3T-GRE sequence. Further, 3T-UTE may even exceed the dynamic range of the 1.5T-GRE protocol, quantifying R_2^* up to $LIC \geq 49.2^{mg/g}$. Together, UTE and GRE at 3T in their current forms allow a comprehensive diagnostic alternative to 1.5T assessment.

Based on robust performance of 3T-GRE for low LIC quantitation⁷², we optimized the 3T-UTE sequence for performance at iron loads over 20^{mg/g}. As such, we chose to acquire UTE data to a maximum TE of 2.0 ms. One downside of this approach is that only one fat oscillation was sampled. At 3T, out-of-phase fat oscillations can cause a substantial reduction in magnitude of the echoes between 0.5 and 1 ms. The combination of these fat oscillations and the 3T-UTE protocol's chosen echo times lead to non-obvious interactions with the exp+c fitting model⁹², which assumes that the fat behavior can be sufficiently modeled by the bias term in equation 5.1. For LICs between 15^{mg/g} and 20^{mg/g}, which demonstrate R_2^* decay rates between 1200 Hz and 1800 Hz at 3T, the fat oscillations cause an apparent acceleration in R_2^* decay while the exponential decay suppresses fat oscillation data

from the later echoes. This causes overestimation of R_2^* and artificially increases LIC from 3T-UTE between 15 and 20^{mg/g}. Over this range, the fat oscillations also interact unfavorably with the bias coefficient from equation 5.1. We found the $S(0)$ -normalized bias, c , from equation 5.1 tended to be 2-4 times larger for the 3T-UTE fit than the 3T-GRE fit over the LIC range of 15-20^{mg/g}; over the higher and lower LIC ranges, the bias values were similar. This behavior is consistent with previous studies⁹². We speculate that extending 3T-UTE to longer echo times would improve the quantitation because the bias term will stabilize with increased oscillations.

The pixelwise exp+c fitting model (equation 5.1) was selected based on its robustness, biopsy validation, and lack of strict protocol and data export requirements^{4,93}. Such considerations may be important in driving clinical adoption, especially when clinical facilities have difficulty acquiring or exporting phase information or hope to assess UTE images with established curve fitting workflows designed for cartesian GRE techniques. Including spectral models of fat in the fitting algorithm may address the challenges related to bias while also allowing for the simultaneous estimation of tissue iron and fat content. This would overcome the 3T-UTE's previously-noted overestimation of LIC for moderate iron loads. However, this approach is more challenging due to stricter data and computational requirements⁹⁴. Further, the addition of fit parameters has been shown to increase the standard deviation of the R_2^* estimates⁹². In certain clinical settings, it may be preferable to choose between the UTE and GRE estimates depending on the patient's expected iron load. In this case, models such as exp+c, which lack explicit fat models, provide a reliable iron estimate; other fitting models such as truncated exponential⁹⁴ should work as long as appropriate R_2^* -LIC calibration curves are used^{95,90}. Though out of scope for this study, we speculate that R_2^*

estimation with complex fitting techniques will meet or exceed the performance of the magnitude-based technique presented here.

Bland-Altman analysis of the 3T-UTE data shows that it is unbiased with respect to 1.5T-GRE estimates for $LIC > 25^{\text{mg/g}}$. Disagreement between 3T-UTE and 1.5T-GRE estimates for $LIC > 40^{\text{mg/g}}$ (shaded region, Figures 5.3,5.5) suggest an improvement in the dynamic range from 3T-UTE compared to 1.5T-GRE rather than a failure of 3T-UTE. Though this could not be experimentally verified, the relationship between 3T-UTE and 1.5T-GRE was identical to the plateau observed between 3T-GRE and 1.5T-GRE; i.e., values exceeding the dynamic range “pile up.” In retrospect, the study would have benefitted from UTE at 1.5T, as well, to accurately measure $LIC > 40^{\text{mg/g}}$. We have subsequently integrated 1.5T-UTE into our clinical protocol.

The clinical applicability of the UTE technique is further supported by its robustness to chest wall motion. In contrast to GRE sequences, which can show significant respiratory ghosting in free-breathing subjects, no coherent ghosts were visible in free-breathing UTE scans. The demonstrated robustness of the free-breathing protocol will immediately improve LIC estimates for participants who cannot complete a breath-hold of over 10 seconds. Patient comfort is improved through the negation of breath-holds and the reduction in scan time due to decreased protocol duration and reduction in repeated series. SNR improvement relative to breath-holding has been demonstrated with triggered, free-breathing UTE imaging⁹⁶, but further studies will be needed to compare quantitative differences between free-breathing and breath-hold protocols in iron imaging.

Although many techniques that shorten TE compared to cartesian sequences are considered UTE sequences⁹⁷, the term “UTE” is often associated with 2D imaging that achieves short echo times by combining data from two excitations

with half-sinc pulses that use opposite slice-selection gradients⁹⁸. The shortened TE is achieved because readout takes place in the space traditionally occupied by the right tail of the sinc pulse. We previously attempted LIC quantitation on both Philips and GE magnets using half-pulse UTE but were unable to achieve reliable quantitation. We speculate that the severe off-resonance that occurs in iron-loaded livers, small timing inaccuracies, and slice-profile effects⁸⁶ led to the failure of this approach. In contrast, 3D UTE techniques such as the one chosen for this study use a non-selective excitation pulse, which have demonstrated more reliable R_2^* quantitation in phantoms⁸⁶. The non-selective UTE pulse is high-bandwidth and has a lower duration than the half-sinc pulses used in slice-selective UTE, preventing off-resonance from causing under-excitation. We believe that this key difference allows 3D UTE to succeed where 2D UTE failed.

Although this study focused on quantitation at 3T, the UTE protocol shows promise at other field strengths. Most notably, it may increase the dynamic range at 1.5T, resolving the demonstrated upper limit of 41^{mg/g}. Further, the imaging challenges resulting from the near-linear increase of R_2^* with field strength will compound at higher field strengths. UTE imaging will likely be the best approach to quantify even low and moderate liver iron at higher field strengths such as 7T. We therefore expect that the UTE for iron quantitation will grow in popularity at all field strengths. UTE approaches may also be synergistic for fat-water separation techniques as well as abdominal QSM⁹⁹.

5.3 Conclusion

Non-selective, center-out radial UTE imaging is a robust supplement to GRE for quantifying liver iron at 3T. Our 3T-UTE protocol accurately tracked 1.5T-GRE LIC estimates up to 40^{mg/g} and potentially measures LICs as high as 50^{mg/g}. The UTE pulse sequence was available through a clinical science key on both software release 3.2.2 and 5.1.7 Philips scanners and did not require breath-holding. The 3T-UTE protocol functions as a turn-key replacement for GRE imaging in high-LIC participants at 3T. Further improvement to the protocol and fitting approach may allow UTE to measure low and moderate iron concentrations with the same accuracy demonstrated at high iron.

5.4 Acknowledgments

This study was supported by the NIH National Institute of Diabetes and Digestive and Kidney Diseases R01-DK097115. Clinical science support was provided by Philips Healthcare. Research space and computational resources were generously provided by Dr. Krishna Nayak of the Magnetic Resonance Engineering Lab.

Parameter	1.5T Gradient Echo	3T Gradient Echo	3T UTE
TEs [ms]	0.96-11.5; 16 linearly spaced	0.76-8.8; 16 linearly spaced	0.19, 0.23, 0.35, 0.60, 0.85, 1.0, 2.0
FOV (AP[cm]xRL[cm])	30x40	30x40	31x31
Slice (# x thickness[mm])	3x10	3x10	6x15
Matrix	84x84	84x84	88x88
TR [ms]/FA [deg]	50/30	50/30	5/4
Scan time [sec]	14	14	5 per echo time/35 total
Breath-hold [sec]	14	14	none
Gradient strength	Max	Max	Max
Acceleration	No	No	TFE Factor 200

Table 5.1: Relevant scan parameters

Measurement	Min	Max	Mean±StDev
Height [cm]	117	179.8	156.2±15.3
Weight [kg]	20.1	89.7	54.3±17.1
Body Surface Area [m ²]	0.81	2.1	1.5±.3
Body Mass Index [kg/m ²]	14.7	34.3	21.9±5.1
Ferritin [ng/mL]	199	16300	4483±4890
ALT [U/L]	18	391	74.5±84.5

Table 5.2: Ranges of demographic and laboratory data for the participant population

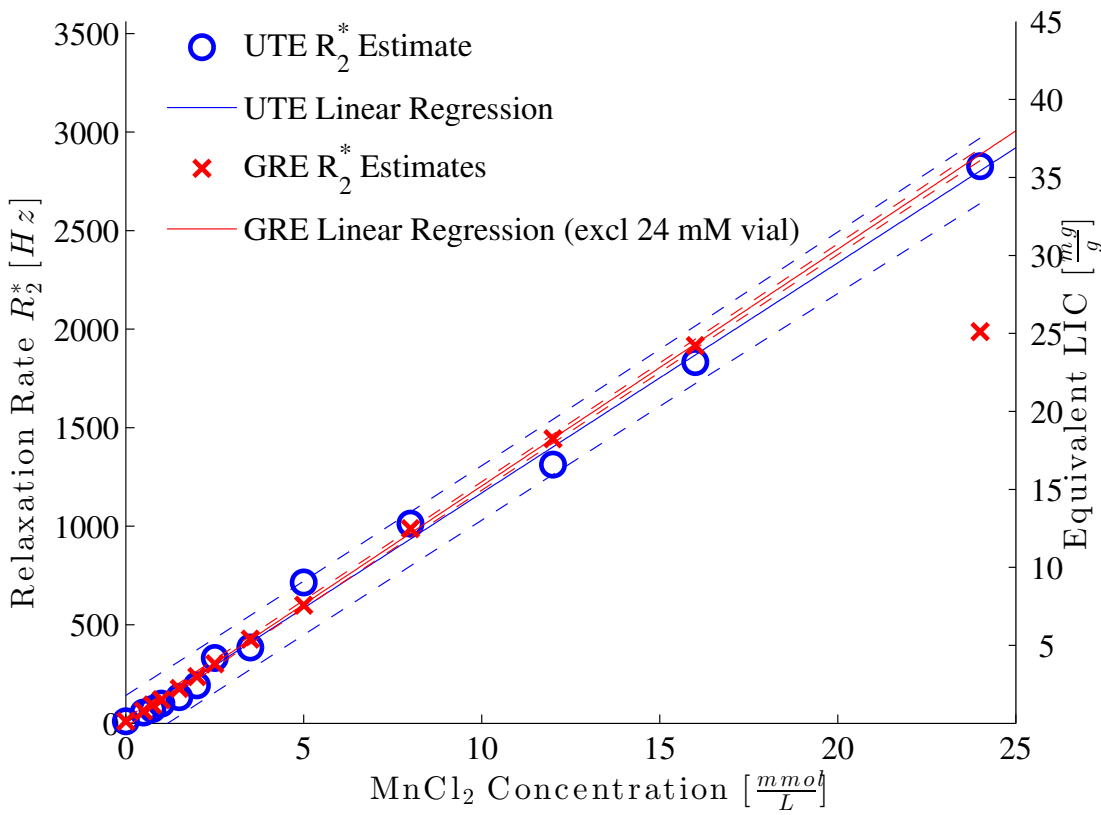


Figure 5.1: Phantom results demonstrate linear correlation of MnCl_2 concentration and R_2^* . Regression analysis demonstrated the following relationships: R_2^* -UTE = $117 \times [\text{mM } \text{MnCl}_2] + 1.6$ ($r^2 = 0.9955$, $r_{adj}^2 = 0.9951$, $p < 0.0001$); R_2^* -GRE = $120 \times [\text{mM } \text{MnCl}_2] + 3.5$ ($r^2 = 0.9998$, $r_{adj}^2 = 0.9998$, $p < 0.0001$). The R_2^* -GRE regression excluded the highest-concentration vial due to expected failure of fitting. 95% confidence intervals are shown with dashed lines for each regression.

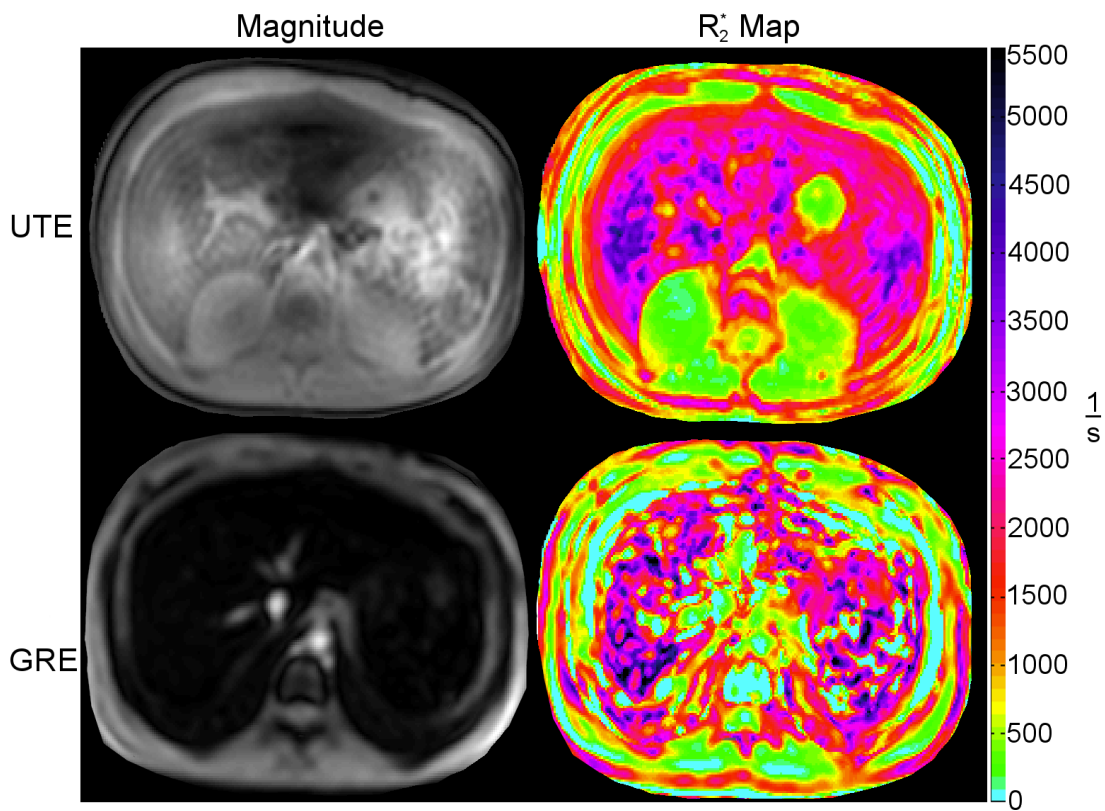


Figure 5.2: Example images demonstrating image quality of 3T-UTE (above) and 3T-GRE(below) first echo images and associated R_2^* maps. The image selected is from a subject with high LIC, causing the failure of the 3T-GRE protocol to capture sufficient signal to perform R_2^* estimation.

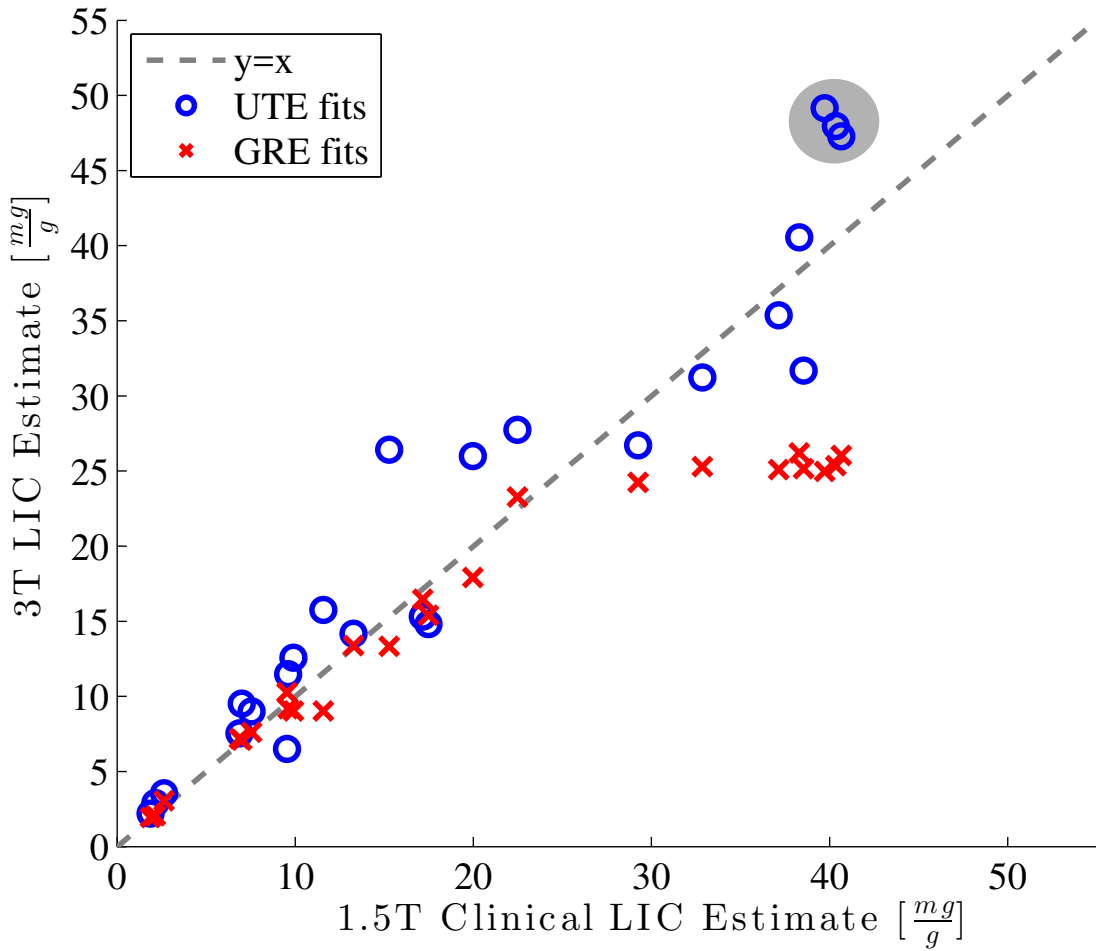


Figure 5.3: Scatter plot demonstrating LIC estimates made with 3T GRE and 3T UTE image series compared with clinical estimates. Catastrophic failure in LIC estimates is apparent in 3T GRE estimates for participants with clinical iron loads over 25 mg/g . Points in the shaded region demonstrate 3T-UTE LIC estimates that exceed the upper limit that 1.5T-GRE can quantify.

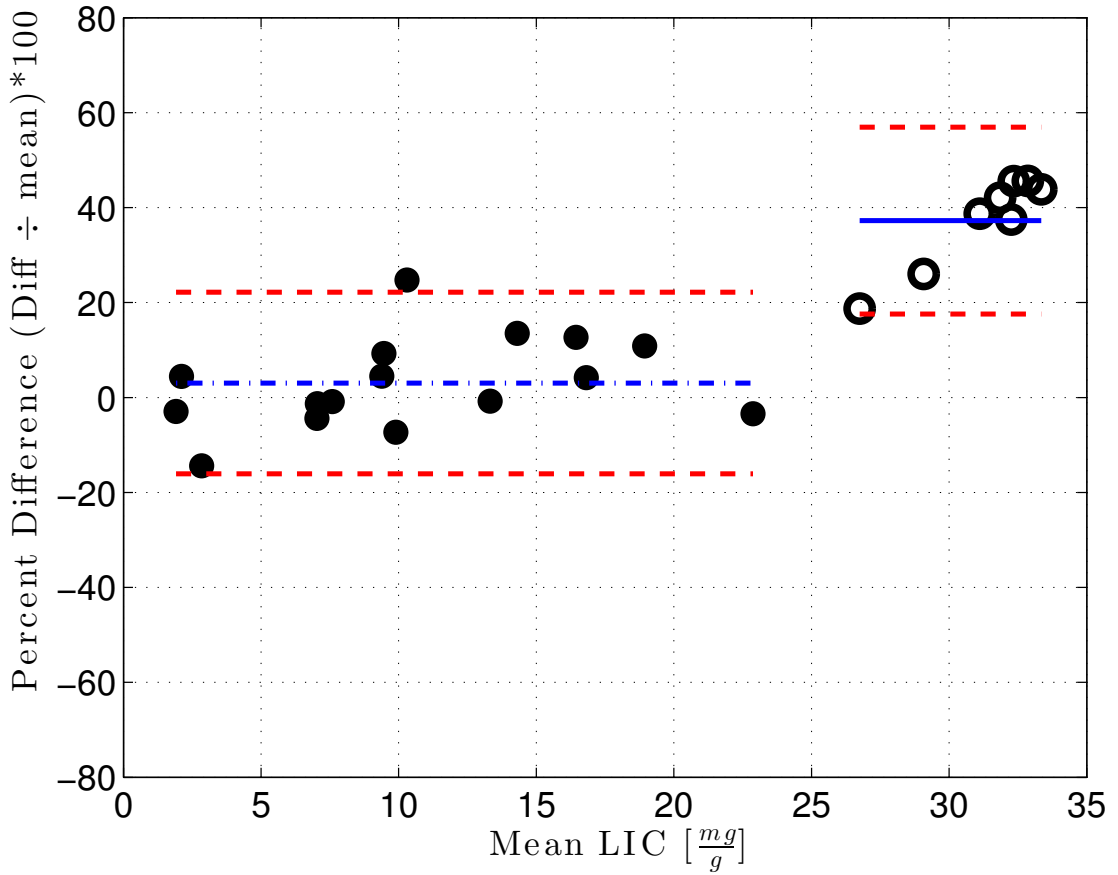


Figure 5.4: Bland-Altman analysis of LIC estimates made with 1.5T-GRE and 3T-GRE series. Solid circles (\bullet) represent participants with clinical LIC ≤ 25 mg/g ($\mu=3.0$ (not significant), $\sigma=9.6$). Unfilled circles (\circ) represent participants with clinical LIC > 25 mg/g ($\mu=37.3$, $\sigma=9.8$). 95% limits of agreement are shown as dashed lines. Insignificant bias is demonstrated with a dash-and-dotted line. The bias demonstrated in the low-LIC cohort is thought to be a result of a lack of sufficiently long TEs in the UTE protocol; simulation results (supplemental results) for the 3T-UTE protocol in low LIC loads supports this conclusion.

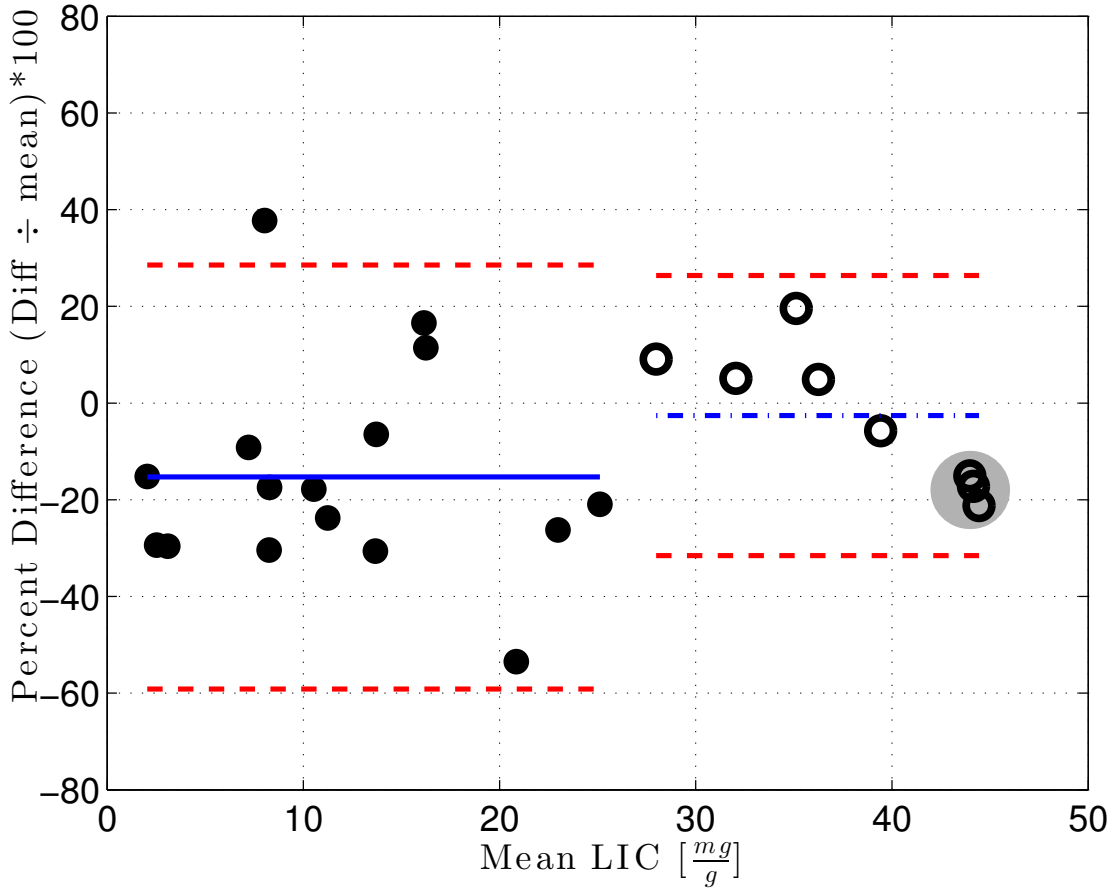


Figure 5.5: Bland-Altman analysis of LIC estimates made with 1.5T-GRE and 3T-UTE series. Solid circles (●) represent participants with clinical LIC $\leq 25 \text{ mg/g}$ ($\mu = -15.3$, $\sigma = 21.9$). Unfilled circles (○) represent participants with clinical LIC $> 25 \text{ mg/g}$ ($\mu = -2.6$ (not significant), $\sigma = 14.48$). 95% limits of agreement are shown as dashed lines. Insignificant bias is demonstrated with a dash-and-dotted line. Points in the shaded region demonstrate 3T-UTE LIC estimates that exceed the upper limit that 1.5T-GRE can quantify.

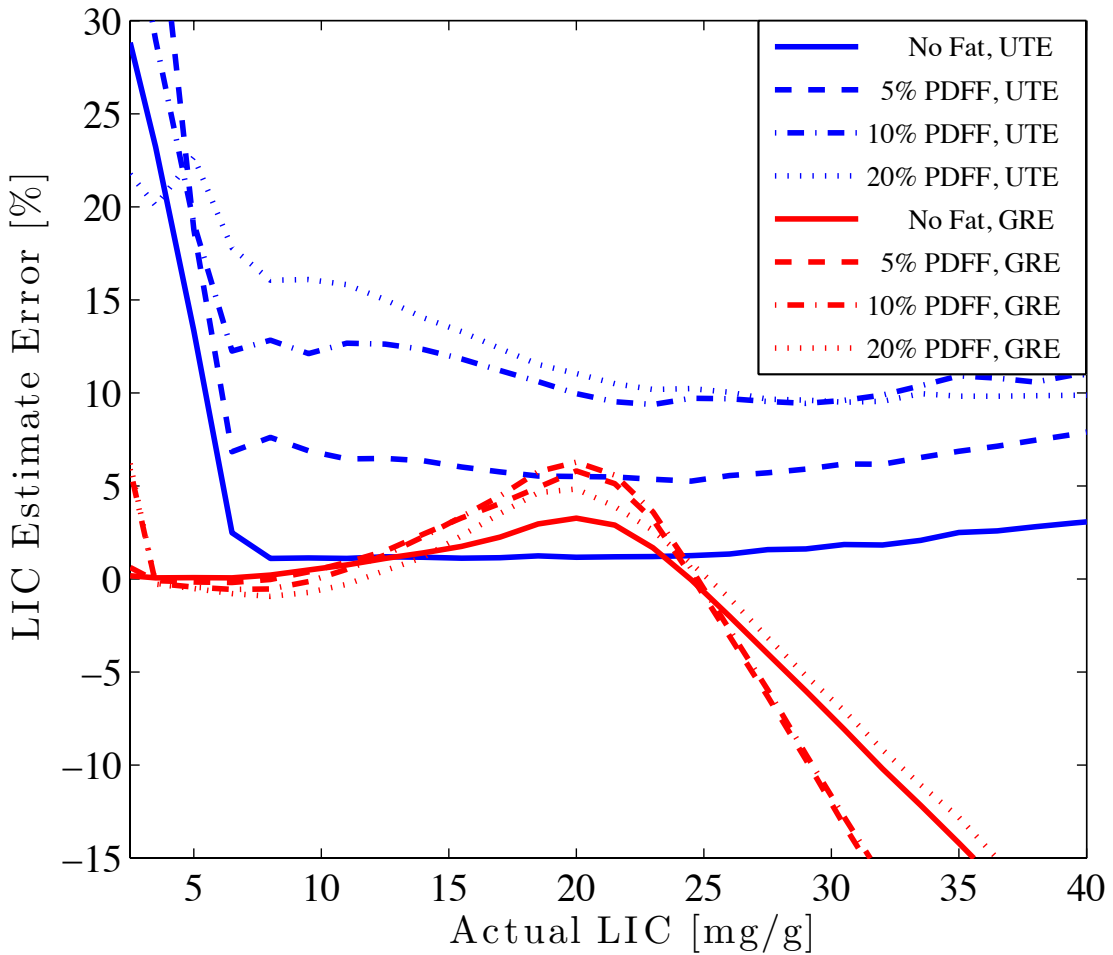


Figure 5.6: Simulation of 3T-GRE and 3T-UTE echo times with 0, 5, 10, and 20% PDFF over an LIC range of 0.5-45 mg/g demonstrate that increasing fat fraction has a greater effect on R_2^* for the UTE sequence than the GRE sequence. In particular, the 3T-UTE overestimates LIC more as PDFF increases for a given LIC. Further, at low LIC, the simulations for PDFF=0% indicate that LIC is overestimated when noise is present and the decay rate is slow. The magnitude of error due to physiologically realistic PDFF may explain the increased apparent measurement variation between GRE and UTE.

Chapter 6

Chemical Shift Imaging - A Spectroscopic Approach to Quantifying Iron

6.1 Abstract

6.1.1 Purpose

There is significant interest in the simultaneous quantitation of tissue iron and fat content. However, the effects of iron can confound phase-based fat quantitation techniques or cause catastrophic loss of signal at higher iron loads and field strengths. In this work, we present a modified chemical shift imaging spectroscopy pulse sequence developed to assess the feasibility of simultaneous quantitation of R_2 , R_2^* , and fat fraction.

6.1.2 Theory and Methods

The minimum TE limits the dynamic range of pulse sequences to estimate R_2^* . 4 chronically-transfused human volunteers were imaged with 1.5T cartesian gradient echo(1.5T-GRE), 3T cartesian gradient echo(3T-GRE), and modified CSI pulse sequences; minimum TEs were 0.96, 0.76, and 3.1 ms, respectively. R_2^* was estimated with an exponential signal model with and without a spectral model

for fat. Regression analysis compared CSI to clinical R_2^* -based LIC estimates. A phantom was assessed for validation.

6.1.3 Results

Human R_2^* estimates with the 3.1 ms echo time correlated well with clinical estimates (slope=1.09, $r_2^{\text{adj}}=0.9900$, $p=0.0033$). Phantom estimates achieved reasonable estimates of R_2^* but demonstrated a steeper relationship between imaging and CSI R_2^* than expected (slope=1.92, $r_2^{\text{adj}}=0.9710$, $p=0.0097$). R_2^* fitting was unsuccessful in all cases. Fat fraction estimation failed but significant spectral bandwidth is demonstrated in the CSI signals.

6.1.4 Conclusion

Short echo time CSI provides a promising approach to quantify R_2^* , R_2 , and PDFF in high-iron patients at 3T by increasing SNR and acquiring an increased number of samples for use with spectral techniques.

6.2 Introduction

Magnetic resonance imaging (MRI) is popular for the noninvasive estimation of tissue iron in patients with transfusional iron overload. Relaxation rates R_2 ($1/T_2$) and R_2^* ($1/T_2^*$) are often independently obtained at 1.5T to estimate iron^{7,4} and are showing increased use with 3T magnets. Although calibrations between LIC and R_2 and R_2^* have been established at 3T, a number of practical challenges limit the dynamic range of iron measurements for both spin echo and gradient echo techniques. Further, estimating R_2 via a CPMG multiecho sequence in conjunction with R_2^* at any field strength may provide additional clinical value and has potential

to expose the mechanisms of chelators used to treat iron overload⁶. Therefore, methods to obtain both measurements should be established at 3T.

Chemical shift imaging (CSI) is a spectroscopic technique that obtains one or more echoes of a single phase-encoded voxel after applying an excitation and an inversion RF pulse. The echo's free induction decay (FID) is governed by R_2^* , similar to the FID produced after a single RF pulse is applied. Unlike a traditional FID, the amplitude of the echo is enveloped by the R_2 decay. Though this approach is normally used to examine spectra to identify metabolites or gather chemical shift data, this technique also has the potential to simultaneously estimate R_2^* from the FID while estimating R_2 from the maximum intensity of the spin echo if processed in the time domain rather than the Fourier domain. In addition to providing two quantitative metrics of tissue iron, CSI increases SNR by imaging a large voxel than a traditional imaging sequence.

In this work, we present a modified CSI sequence that uses a custom RF pulse to substantially reduce echo time. Human validation of R_2^* estimates demonstrates that the substantial SNR improvements allow quantitation of R_2^* in heavily iron-loaded human subjects. Phantom data demonstrate further proof-of-concept R_2^* .

6.3 Theory

Slice-selective RF excitation pulses allow a considerable reduction of scan duration by exciting only a slice or slab of tissue rather than the whole body, obviating the need for phase encoding all 3 spatial dimensions. This prevents phase wrapping in the slice selection direction and reduces the number of repetitions required to produce an image, reducing specific absorption rate (SAR) and total scan duration. However, these pulses tend to require more time to transmit than “hard”,

non-selective RF pulses for an equivalent flip angle. This in turn increases the minimum echo time that a sequence can achieve.

The performance of a slice-selective pulse is commonly assessed in the Fourier domain because the slice profile, the shape of the excitation of a cross-sectional portion of tissue, is given by the Fourier transform of an RF pulse. When a slice selection gradient is applied during the RF pulse transmission, it creates a relationship (most commonly linear) between frequency and position. Any spins within the bandwidth of the pulse are excited. We can determine the shape of the slice profile with the Fourier transform of the RF pulse waveform.

$$\begin{aligned} M_z(\omega) &\propto \mathcal{F}(B_1^+(t)) \\ T_{slice} &\propto \frac{1}{\gamma G_z \tau} \end{aligned} \tag{6.1}$$

where M_z is the magnetization profile along the slice direction as a function of ω (spin frequency), B_1^+ is the excitation waveform at time t , γ is the Larmor frequency, G_z is the gradient strength, τ is the duration of the RF pulse, T_{slice} represents slice thickness, and \mathcal{F} represents the Fourier transform operator.

In general, there is a trade-off between pulse duration and the precision of the slice profile. For many clinical imaging applications, the increased echo time is of no importance and improving resolution improves the clinical applicability of the image, particularly when assessing physiologic structures for physical damage. For high iron loads, the quantitation is more important than the resolution of the image. Reduction of echo time is critical to capture rapid decay signals.

A custom RF pulse was designed to achieve adequate slice selection while reducing the pulse duration to achieve an sufficiently short echo time to capture iron's rapid decay exhibited. The pulse is based on a Dolph-Chebyshev window function and approximately 2-4 times faster than a traditional sinc pulse for a given flip

angle and slice thickness. In conjunction with a hard 180° inversion pulse, the CSI sequence minimum echo time was reduced to 3.1 ms from 7.1 ms. The time savings is apparent in figure 6.1. The slice profile produced by the Dolph-Chebyshev pulse (figure 6.3) shows less uniformity than the sinc pulse (figure 6.2). The reduction in slice profile homogeneity does not preclude the applicability of this pulse to relaxometry.

6.4 Methods

Study participants were selected from a population of patients at the Children's Hospital of Los Angeles (CHLA) undergoing chronic transfusion therapy for sickle cell disease, thalassemia, and other rare anemia syndromes. Participants provided informed consent to participate in an IRB-approved study (CHLA Study CCI-14-00034). Each participant received a clinically indicated MRI assessment for iron overload on a 1.5T scanner followed by a research imaging protocol at 3T. Images were acquired on single-RF-transmit Philips Achieva 1.5T and 3T clinical scanners (software revision v3.2.2, v5.1.7, or v5.1.9, Philips HealthTech, Best, Netherlands) using 16-element SENSE-XL torso coils. Reference liver iron (imaging) estimates were obtained from R_2^* estimates made with 1.5T or 3T imaging protocols. A 3-slice gradient echo dataset was gathered with the following parameters: FOV=30x40cm, slice thickness=10mm, matrix=84x84, TR=50ms, FA=30°, 16 linearly spaced echoes between [0.96-8.8] ms (min TE=0.76 for 3T), transverse slice plane. 1.5T- R_2^* was converted to 3T- R_2^* using a previously derived calibration⁵⁸. Spectroscopy data were obtained with a modified, single-echo CSI sequence using a Dolph-Chebyshev excitation pulse and hard inversion pulse with the following scan parameters: TE = [3.1,7.0,11.0,15.0]ms, TR=1000ms, NEX=1, matrix=

[36x20], voxel size=10.5x10.5mm, slice thickness=15mm, 1024 samples, spectral BW=8000 Hz.

A phantom was constructed out of 1-liter Nalgene bottles containing tap water, 1 and 3 mM MnCl₂ solutions, Philips Phantom Standard CuSO₄ Solution 11, and pure mineral oil. It was assessed with the same protocol as human subjects but used a coronal slice rather than transverse. The phantom B₁⁺ was assessed with a single slice, dual repetition time (TR) B₁⁺ mapping sequence⁸² with TE/TR₁/TR₂ =3ms/20ms/120ms, bandwidth of 2894Hz/pixel, voxel size of 4.2x4.2x8 mm³, and one signal average.

Voxels representing liver or phantom solution were identified within the CSI datasets by a graduate student with 5 years of experience. FIDs were gathered by removing samples from the echo signal prior to the maximum magnitude sample present for a given voxel. We hypothesized that iron-mediated center frequency shift would require additional quadrature demodulation. This was tested by fitting the data with and without a signal-maximizing quadrature demodulation scheme. The demodulation frequency was determined by finding the maximum echo amplitude after demodulation over 10 Hz increments for a range of ±300 Hz off-resonance. R₂^{*} and R₂ were estimated by applying an ExpC signal model (equation 6.2) to the magnitude FID of the 3.1ms dataset and the echo peaks of all datasets, respectively, using software developed in MATLAB. Simultaneous R₂^{*} and proton density fat fraction (PDFF) estimation was also performed by applying a signal model including a 6-peak spectral model for fat (henceforth “spectral”)⁹² to complex 3.1 ms FIDs.

$$S(t) = S_0 e^{-R_2^* t} + c \quad (6.2)$$

The spectral model is:

$$S(t) = S_0 e^{-R_2^* t} \times (W + F * p) \quad (6.3)$$

$$\begin{aligned} p = a_1 \times e^{j*2*pi*f_1*t} + a_2 \times e^{j*2*pi*f_2*t} + a_3 \times e^{j*2*pi*f_3*t} a_4 \\ \times e^{j*2*pi*f_4*t} + a_5 \times e^{j*2*pi*f_5*t} + a_6 \times e^{j*2*pi*f_6*t} \end{aligned} \quad (6.4)$$

with coefficients:

Coeff	1	2	3	4	5	6
a	0.047	0.039	0.006	0.12	0.70	0.088
f / (B0 * 42.58)	-0.6	0.5	1.95	2.6	3.4	3.8

W and F represent water and fat fraction, respectively. All fits constrained S_0 to a range of 90-180% of the maximum signal value present in a voxel's signal time course. R_2^* was constrained to a range of 10-5500 ms. When present in the fit, bias values were restricted to a range of 0-1 and PDFF was restricted to 0-20%. Imaging and CSI R_2^* values were compared using linear regression analysis.

SNR was estimated in CSI signals by calculating the quotient of the maximum echo intensity and the standard deviation of a noise-only voxel. Imaging SNR was determined by assessing the finding the quotient of signal intensity in a representative phantom ROI and the standard deviation of a noise-only ROI⁶⁷. Because the clinical R_2^* estimates were made using different protocols, image SNR was estimated by proxy in a 3D radial image with a TE of 2.27 ms (protocol otherwise identical to 3T-UTE protocol, chapter 5); the image was chosen as the nearest echo time available for comparison with the CSI data without on-scanner, post-acquisition noise correction activated.

6.5 Results

Analysis of phantom results demonstrated that delineations between the bottles (layout demonstrated in figure 6.4) could be identified in the low-resolution CSI data, indicating that the CSI sequence is capable of discriminating the different species. The water bottle was not differentiable from the larger MnCl₂ bottles. Quantified values of R₂^{*} are noted in table 6.1. Regression analysis demonstrated a fit line of R₂^{*}-CSI = 1.92 R₂^{*}-imaging - 273.27 ($p = 0.00972$, $r_{adj}^2=0.9710$). Imaging and CSI R₂ estimates were uncorrelated. A B₁⁺ map is demonstrated in figure 6.9.

Four human subjects with known moderate to severe liver iron quantities were assessed with the CSI protocol. Visual inspection of the CSI data demonstrated significantly reduced spatial resolution (figure 6.6). SNR was estimated in representative voxels and found to be approximately 1200 while imaging data demonstrated an SNR of about 320 in the corresponding regions. Numerical values for 3T-CSI and clinical 3T-equivalent R₂^{*} values are demonstrated in table 6.2. R₂^{*} estimates were found to best fit existing patient results without the need for demodulation. Linear regression of ExpC-CSI R₂^{*} values and imaging R₂^{*} estimates demonstrated a strong linear correlation (slope=1.09, $r_{adj}^2=0.9900$, $p=0.0033$); regression results are summarized in figure 6.7. ExpC R₂ estimates and ExpC R₂^{*} estimates performed on human CSI data with TE \geq 7.1 ms were uncorrelated with LIC. Spectral-CSI fitting failed to predict LIC and tended to generate unreasonably large proton density fat fraction estimates (see 6.8, right panel). Examples of signals and fit models are shown in figure 6.8.

6.6 Discussion

Quantitation of tissue iron has remained a persistent challenge at higher field strengths. Though recently developed imaging techniques with reduced echo times can quantify extreme iron loads ($LIC \geq 40 \text{ mg/g}$) with $1.5T^{100}$ and $3T$ magnets (chapter 5), the effects of fat, motion, imperfect breath-holding, new sampling trajectories, and processing techniques remain unexplored. Effects from fat that are negligible at longer echo times cause significant fitting error when UTE approaches are used, as demonstrated in chapter 5. Chemical shift imaging shows great promise as a technique to probe these questions and potentially accomplish iron quantitation in situations where imaging techniques fail.

Initial human subject results show that an unoptimized CSI protocol can match the dynamic range of clinical $1.5T$ R_2^* quantitation techniques while also providing spectral information that cannot feasibly be acquired using imaging sequences. The strong linear correlation between the R_2^* estimates from 3.1 ms CSI FIDs matches the expected R_2^* -LIC calibration within existing clinical measurement variability. When compared with UTE imaging data, CSI data demonstrates significantly improved SNR. Though UTE imaging can estimate most clinical iron burdens at $3T$, the SNR improvement from CSI may be useful when imaging approaches fail at extreme LICs or higher field strengths. The substantial SNR improvement over imaging sequences also allows CSI to capture signals where spin echo imaging sequences fail. Traditional spin echo sequences are limited to a minimum echo times of $4\text{-}6 \text{ ms}$ and fail to quantify moderate to severe liver iron. In contrast, the high SNR demonstrated in the CSI FIDs outweighed rapid R_2 decay, giving CSI the potential to achieve a dynamic range in R_2 -based LIC quantitation matching that of the $1.5T$ imaging. What's more, we have achieved first echo times as short as 0.97 ms in spin echo imaging sequences using modified RF pulses such as those

presented in figure 6.1. Further optimization of the protocol using lower excitation angles and new pulses could potentially drive first echo times below 1 ms, paving the way for extreme dynamic range gains.

Though existing dynamic range limits of CSI- R_2^* -based LIC estimates may be sufficient for clinical decision making, the failure to estimate R_2 in human CSI data demonstrates that shorter first echo times may be necessary. Given that human R_2^* estimation only succeeded in 3.1 ms CSI data, we believe that the longer echo times did not capture usable signal. The equivalent 3T- R_2 conversions (noted in table 6.2) would normally require a minimum echo time well below 3.1 ms to quantify R_2 with images. It is therefore unsurprising that longer echoes could not acquire usable signal. Further, the success of the 3.1 ms TE at capturing quantifiable data is somewhat surprising even with improved SNR. Human R_2 estimation ultimately failed due to an insufficiently sampled decay curve rather than a failure of the technique itself. It is likely that further reducing minimum TE will allow sufficient sampling of the R_2 decay curve to achieve reasonable estimates.

Inspection of phantom R_2 estimates found that the fits were reasonable given the data. This suggests that R_2 estimation should be possible. However, the lack of correlation between imaging and CSI R_2 estimates is not completely understood. The challenges of using spin echoes for fast decay quantitation have been well-established at 3T^{36,99} and significant B_1^+ inhomogeneity effects are discussed in chapter 4. The achieved B_1^+ in the phantom range from about 50% to 150%, which may be responsible for the failed correlation. The recent development of techniques such as MR fingerprinting¹⁰¹ may provide a more robust way to estimate R_2 and probe tissue morphology than spin echo R_2 estimates alone. MR fingerprinting normally relies primarily on the relaxation parameters for each tissue. Applying the Monte Carlo simulation⁶ to MR fingerprinting would allow us to directly join

our imaging parameters to the underlying iron distribution while also including confounders such as B_1^+ heterogeneity. It is also likely that improved sampling schemes would directly improve R_2 estimates and increase robustness of higher order approaches.

Improving decay sampling will likely improve also improve the usability of CSI's spectral data. Particularly, a more reliable estimate of proton density may be possible with shorter TEs. As previously demonstrated, a reliable S_0 estimate can significantly improve relaxometry estimates as shown in chapter 2. We speculate that the failure to estimate PDFF is related to a lack of appropriate constraints for the increased degrees of freedom in the fitting problem. Fat oscillations may cause underestimates of total proton density, which can have large consequences on subsequent decay and PDFF estimates. A reliable S_0 estimate would be useful immediately useful in anchoring all fits but the higher dimensionality of the spectral fits particularly stands to benefit from better initial constraints in this case. Using an S_0 constraint alone or using the theoretically inferior ExpC model to provide a reasonable constraint for decay parameters will likely increase the robustness of spectral fits without the need for additional acquisitions. We hope to improve these approaches when a sufficiently large dataset is gathered.

Although CSI is officially an imaging technique, it straddles the worlds of imaging and spectroscopy. When applying CSI to body imaging, users familiar with imaging and spectroscopy alike must take care to avoid pitfalls due to assumptions they may have developed in their previous research or experience. From an imaging perspective, the use of multiple phase encoding gradients makes CSI datasets susceptible to aliasing in two (or three) directions rather than one, as is common in slice-selective MRI where the readout filter prevents aliasing in the frequency encoding direction. Combined with the low resolution of the data, it can

be challenging to realize that the sequence is not working as intended. Likewise, in contrast to many spectroscopic approaches water suppression must be disabled or else the central peak of the signal will be suppressed, confounding R_2 and R_2^* estimates. Further, an uncommonly high spectral bandwidth is necessary to capture large off-resonance and fat oscillations in the signal. Although the term chemical shift imaging may imply that electron shielding in organic molecules is completely responsible for the frequency shifts even though the susceptibility of the iron's susceptibility causes off-resonance by amplifying the local magnetic field. Finally, while 35 ms is commonly the shortest echo time used in spectroscopy, the aggressively short echo times presented here are an absolute requirement to capture the rapid signal decay. For these reasons, the data resulting from this application of CSI is neither conventional imaging data nor conventional NMR data that a clinical spectroscopist would be familiar with interpreting; extreme care should be taken to ensure that the protocol is functioning as expected.

In addition to the theoretical and implementation challenges, a number of practical challenges must be resolved before CSI is clinically applicable. Due to the need for phase encoding in two directions to suppress aliasing, the CSI protocols tend to exhibit long durations. Although the free-breathing acquisitions here were sufficient to quantify R_2^* , the error introduced remains unquantified. Reducing scan duration sufficiently for use with breath-holding would likely require multi-coil acceleration techniques. Saturation bands may be helpful but their effect on the spectral content of the remaining images is unknown. It may also be possible to reduce the TR, though no signal models have been testing with T_1 effects in this context. Image segmentation is complicated by the low resolution of the image. Although choosing landmarks from survey images can allow for correct ROI placement, we have not explored techniques to ensure that partial voluming does not

Material	CSI R_2^* [Hz]	Imaging R_2^* [Hz]
CuSO ₄ 150	10	
1mM MnCl ₂	221	126
3mM MnCl ₂	319	342
mineral oil	183	101

Table 6.1: R_2 and R_2^* estimates in phantom

Patient	3T-CSI R_2^* [Hz]	3T-equivalent R_2^* [Hz]	3T- R_2 [Hz] (computed)
1	1380	1484	265
2	927	910	200
3	3516	3322	410
4	1708	1795	295

Table 6.2: 3T-CSI and 3T-equivalent R_2^* estimates in four human subjects. Conversion to R_2 is included for reference.

invalidate fit results. Further, traditional fitting approaches can be confounded by the spectral content of the signals; significant oscillations can be exposed by the high bandwidth of the readout which are not usually noticeable in imaging datasets and lead to the erroneous amplification of decay rates.

6.7 Conclusion

CSI combined with reduced TE through custom RF pulses was successful at quantifying R_2^* in four high iron patients. Phantom data suggest that simultaneous R_2^* and R_2 estimation can be accomplished with mono-exponential fitting techniques. With additional validation, optimization of protocol parameters, and further decreased TEs, we expect that CSI will provide robust liver iron estimates and potentially fat quantitation with high dynamic range at many field strengths.

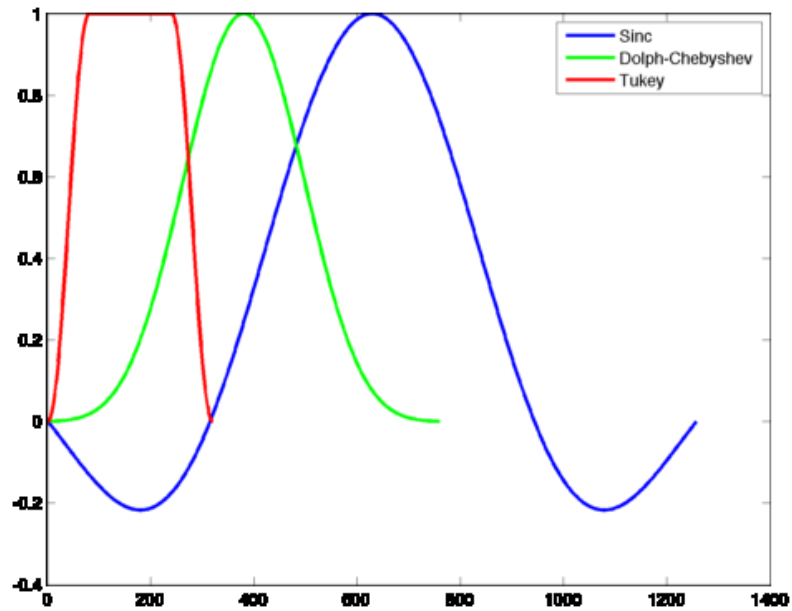


Figure 6.1: Comparison if sinc (blue), Dolph-Chebyshev (green), and Tukey (red) excitation pulses for a given flip angle.

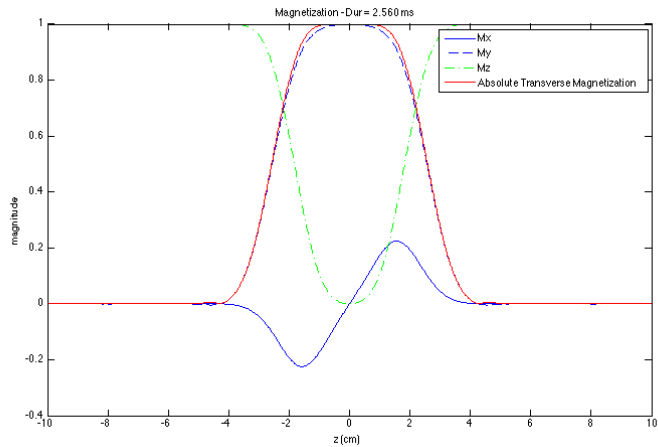


Figure 6.2: Achieved slice profile for Sinc Pulse

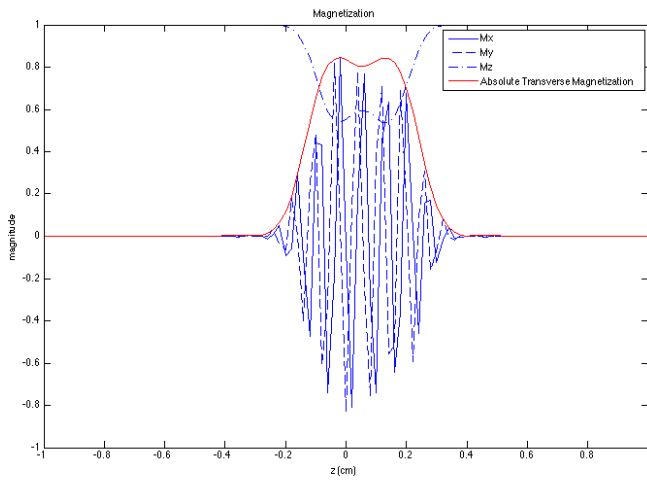


Figure 6.3: Achieved slice profile for Dolph-Chebyshev pulse

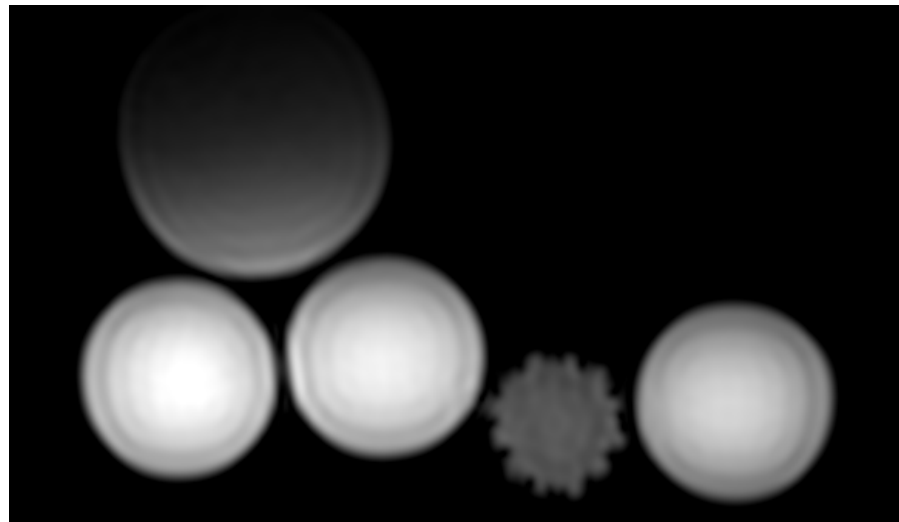


Figure 6.4: Layout of the phantom demonstrating, from top to bottom, left to right, bottles of Philips Solution 11, mineral oil, tap water, 1mM MnCl_2 , tap water, and 3mM MnCl_2 .

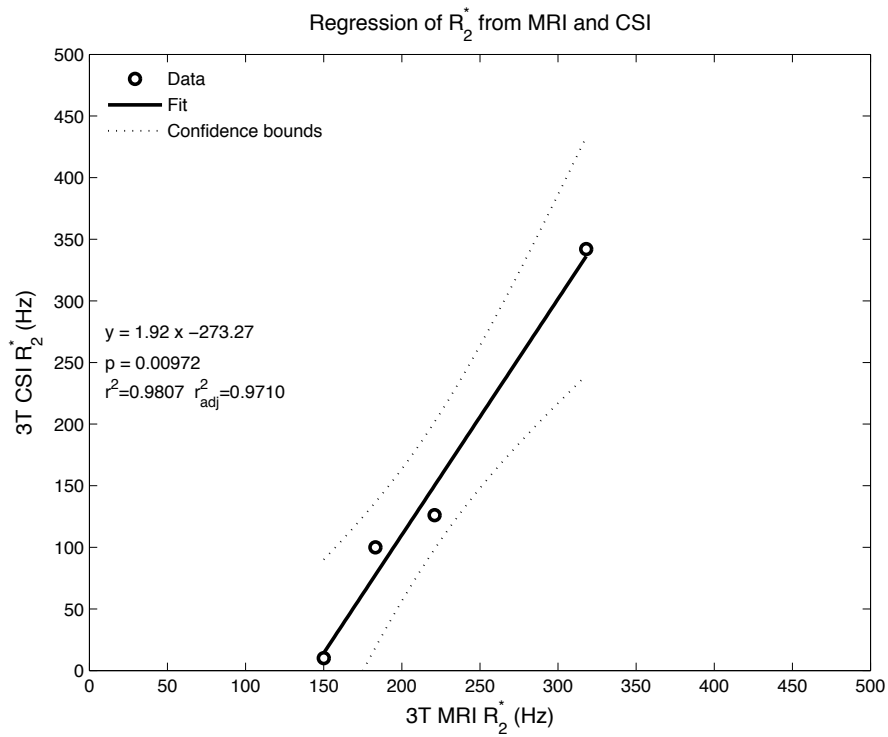


Figure 6.5: Regression of phantom R_2^* estimates. The water vial was excluded due to inability to differentiate it from surrounding $MnCl_2$ vials in the CSI R_2^* and S_0 images. The slope is notably steeper than the expected relationship. However, the magnet reported an unreliable shim for the CSI sequence, which can lead to accelerated R_2^* decay.

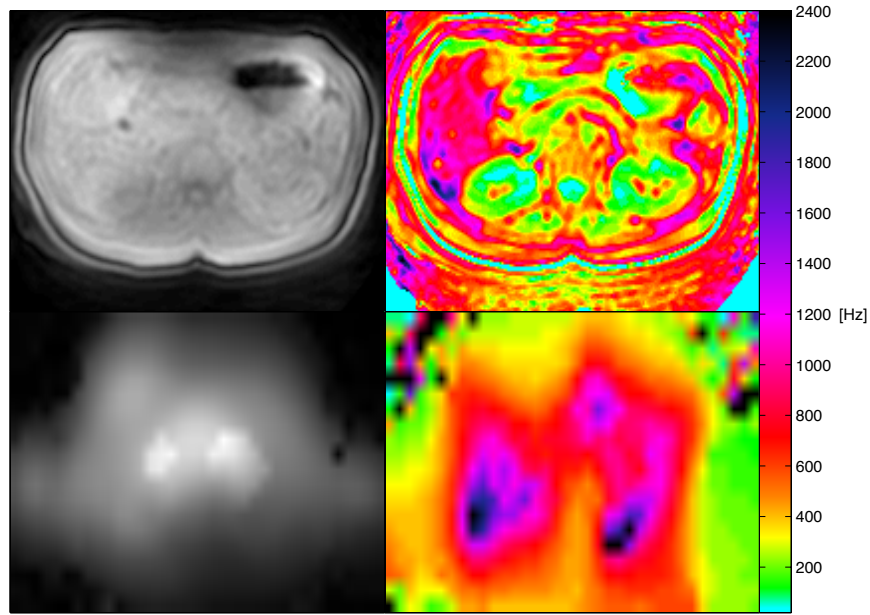


Figure 6.6: Comparison of standard image and R_2^* map with CSI S0 image and R_2^* map. Slice location is not preserved between the images shown.

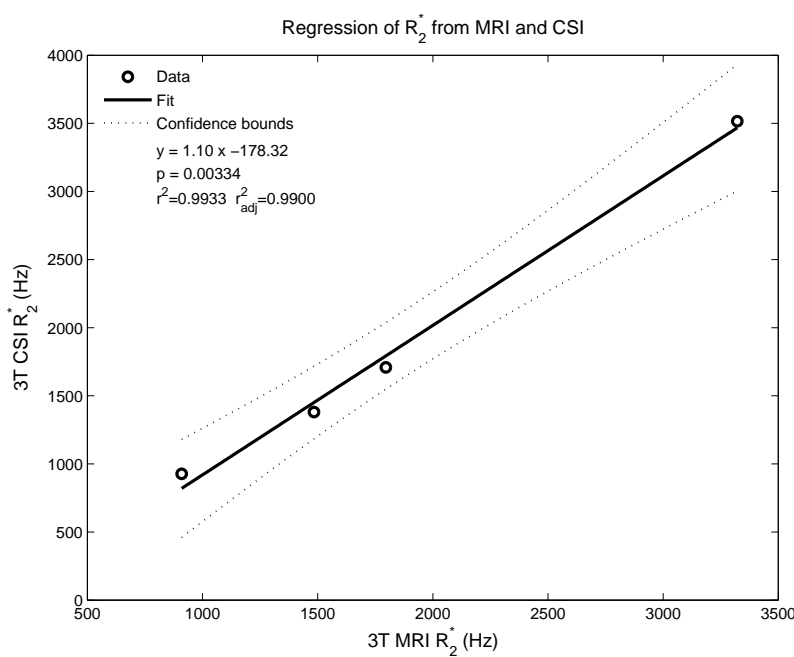


Figure 6.7: Regression of clinically-obtained 3T R_2^* estimates and CSI R_2^* estimates in four human subjects.

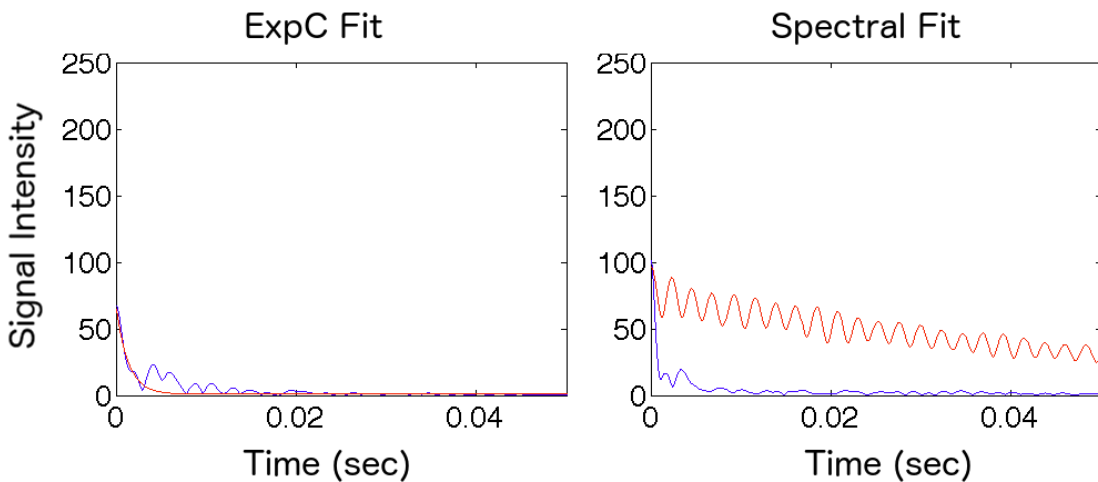


Figure 6.8: A demonstration of signal from a single voxel (blue curve) and resulting fit (red curve). The ExpC model (left) displays reasonable relaxation estimation behavior even in the presence of increased spectral content. The spectral fit (right) fails, likely due to the high order of the model; this often leads to overestimating PDFF significantly.

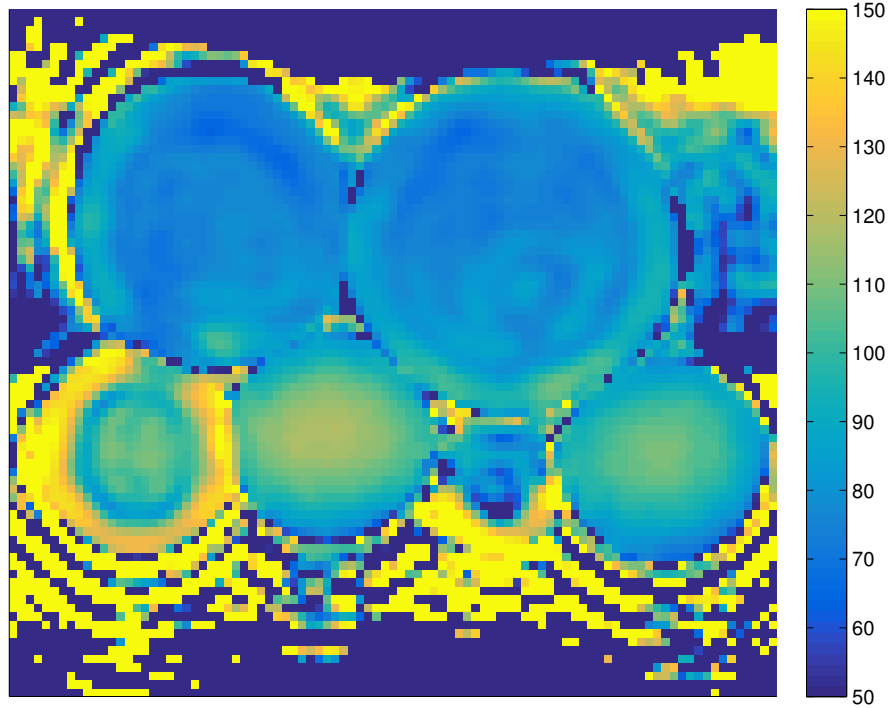


Figure 6.9: B_1^+ map demonstrating the wide variety of flip angles achieved in the phantom.

Chapter 7

Conclusion

MRI has become the clinical standard of care to assess iron in a variety of organs due to its safety, noninvasiveness, reproducibility, and speed. Although the original techniques that have seen wide-spread clinical adoption were developed at 1.5T, the proliferation of 3T scanners requires the validation of these quantitative techniques at a new field strength. What's more, field-dependent enhancement of iron's signal decay rate leads to the failure of existing scan and analysis techniques for moderate-to-high iron patients at 3T — both R_2^* and R_2 contrast mechanisms demonstrate catastrophic failure near liver iron loads of about 20 mg/g. These findings correspond well with the minimum echo time limits of about 0.7 ms and 4 ms in commonly-used cartesian gradient echo and spin echo techniques. We selected a multi-faceted approach, first involving the development of new MRI pulse sequences and applying them to phantom and human subject scanning; combined with simulations and updated curve fitting techniques, these new imaging techniques increase the dynamic range of 3T-LIC measurement. By extending simulation frameworks to account for 3T non-idealities, developing custom RF pulses with shorter duration, leveraging center-out k -space acquisitions, better utilizing acquired images through improved fitting, and characterizing imperfections encountered at 3T, the limitations of 3T were largely overcome. The results of this work have ultimately facilitated the expansion 3T's capabilities to include iron quantitation across the entire clinically relevant range.

7.1 Original contributions

We first addressed the previously-demonstrated insensitivity⁴⁹ of R_2 to LIC at 1.5T by using a proton density constraint derived from muscle tissue. Human subject data acquired at 1.5T demonstrated the importance of estimating proton density to ensure R_2 sensitivity for high-iron patients, increasing sensitivity relative to unconstrained results by 300%. We found that simulated experiments from our Monte-Carlo framework agreed. Further, the implementation of a constrained non-exponential signal model⁵⁶ showed the saturation of a background decay parameter at a similar iron load to the expected saturation of liver ferritin stores; a second decay parameter in the same model associated with particulate iron increased continuously, mirroring the behavior of increased hemosiderin concentration. Together these results suggest that CPMG spin echo can provide more information about cellular iron distribution than R_2^* or single spin echo- R_2 alone. It also supports our previous speculation that the function of chelators could be reasonably probed using spin echo based techniques.

Second, we addressed the calibration of R_2 and R_2^* vs LIC at 3T using the Monte Carlo model. Through this work, we showed that the 3T relaxivity enhancement for R_2 and R_2^* were 1.48 and 2.03, respectively, when compared to 1.5T calibrations. These results are consistent with experimental results⁷² but provide a closed-form mathematical solution to the relaxivity enhancement as well as an inexpensive way to validate relativity enhancement for an arbitrary field strength prior to in vivo validation.

After answering the question of field-dependent enhancement, the impact of a common imaging confound called B_1^+ inhomogeneity on R_2 and R_2^* LIC estimates was assessed. B_1^+ maps were acquired in human subjects at both 1.5T and 3T to estimate the magnitude of spatial excitation variation. The inclusion of a 3D

Bloch simulator in the Monte-Carlo framework allowed pulse imperfections to be modeled. The results demonstrated that both spatial flip angle variation and whole-liver underexcitation can change R_2 -based liver iron estimates. However, the simulation provides a mechanism to determine the R_2 -LIC calibration curve if the magnitude of the B_1^+ heterogeneity is known. This may allow for numerical correction or selective voxel inclusion to ensure accurate R_2 estimates. The spatial excitation heterogeneity was found to be only relevant to spin-echo imaging. For gradient-echo imaging, the loss of initial intensity only reduced SNR, which can cause failure of quantitation at high iron loads; this effect only occurs in images with readily apparent catastrophic loss of liver signal and does not pose a threat of going unnoticed in the fitting process.

Although R_2^* imaging is robust to excitation heterogeneity, imaging speed still limits R_2^* quantitation to about 2000 Hz when using cartesian readouts on 1.5T and 3T systems, maximum LICs of about 40^{mg/g} and 20^{mg/g} respectively. We overcame this limitation by developing and validating a human imaging protocol using 3D radial imaging to achieve quantitation to at least 40^{mg/g} of iron. Further, we show that it likely quantifies LIC \geq 50^{mg/g}. Though previous studies achieved quantitation in phantoms with a variety of UTE techniques, only recent attempts to use half-pulse excitations in human subjects have succeeded¹⁰⁰. In addition to extending dynamic range of R_2^* -LIC iron quantitation, the radial UTE technique was found to be robust to chest wall motion, allowing the elimination of breath-holding for patients who cannot tolerate extended breath-holding. With further optimization, it may be possible map higher iron loads and show value at lower field strengths as well.

Finally, we assessed a novel means of characterizing iron at 3T involving CSI spectroscopy sequences. The CSI approach is particularly interesting because it

has the potential to estimate both R_2 and R_2^* while also increasing SNR. The inclusion of modified RF pulses reduced the achievable echo time by over 50%, with further opportunities to reduce the echo time with decreased flip angles. The pulse sequence demonstrated good correlation between R_2^* and LIC in high-iron patients and achieved successful proof-of-concept R_2^* estimation in phantoms. It also provided improved spectral information which will be useful for fat quantitation.

7.2 Future Work

This work has opened the door to a variety of continuing research areas. The continued development of the simulation framework allow for more realistic and varied experiments to be conducted while the new scan and fitting techniques may be further refined to decrease variability and uncover new data for use in research and clinical settings. These opportunities are explained below.

Based on the finding that B_1^+ heterogeneity and significant underexcitation regularly occur in liver imaging, improved corrective measures may reduce variability by correcting rather than discarding affected pixels. There may be a closed-form relationship that allows for correction of R_2 maps based on an acquired B_1^+ map at exam time or as an offline reconstruction. In the absence of a well-posed closed-form correction, the existence of regions of varying excitation efficiency might be corrected using the Monte Carlo frame work to build iron-load specific signals for all iron loads.

The many quantitative techniques to assess total body iron have primarily depended on biopsy as the gold standard for liver iron quantitation. As such, iron overload metrics have been compared to one another using Bland-Altman analysis with LIC(3T versus 1.5T, LIC by R_2 versus LIC by R_2^* , LIC by MRI

versus LIC by biopsy, SQUID, or CT). However, biopsy has large sampling and tissue-processing(drying, paraffin extraction) uncertainties; all other indirect metrics have subject-specific variations in their calibration curves. Advancements in gene therapy and bone marrow transplantation have created unique opportunities to sample total-body iron with improved accuracy: patients can present with extremely high total body iron resulting from transfusion but can be treated with phlebotomy once their anemia is cured. Hematocrit and phlebotomized blood volume permit highly accurate measure of iron removal. With such a metric, many techniques can be reassessed against an improved gold standard. Though R_2 and R_2^* are currently thought to be equal measures of longitudinal iron quantitation, phlebotomy would allow a more accurate comparison of the two for a cohort of patients. Further, iron distribution predictions from the Monte Carlo framework could be tested; the known iron accessibility differences between hemosiderin and ferritin^{102,103} would allow for in-vivo validation of the Jensen⁵⁶ signal model and improved understanding of chelator pharmacokinetics. Such patients would also assist with the validation of our finding that the background relaxation rate and aggregate parameter rate diverge as the iron storage mechanisms shift to accommodate high iron quantities. Leveraging the fact that large and small hemosiderin stores demonstrate different accessibilities, growing and shrinking at different rates, would allow for the validation of divergent behavior demonstrated in the patient data and Monte Carlo framework in chapter 2. Such studies would assist with the characterization of chelator behaviors on the different iron populations in the body and provide new insight into iron storage in the human body.

The success of the UTE imaging approach may be able to offer more than just increased dynamic range at 3T. The known 40^{mg/g} limit of 1.5T R_2^* methods could be immediately resolved by back-porting the protocol to 1.5T. Further, the effects

of the free-breathing protocol on exhibited measurement variation remain uncharacterized. We demonstrated that significant variability results from the exclusion of a fat model to a greater degree than traditional gradient echo. Developing a better selection of echo times and imaging parameters may increase the data's inherent robustness to fat, improve low-iron variability, and possibly contribute to the achievement of simultaneous fat and iron quantitation in even moderate-to-high iron patients.

Finally, the development of custom RF pulses has allowed for slice-selective spin echo imaging with drastically reduced echo times. The behavior of the resulting signals is not fully understood. R_2 quantitation in particular demonstrated challenges due to the non-exponential nature of the signal, especially when low flip angles were used to achieve sub-millisecond echo times. Improvements in reconstruction, such as a repurposing of multislice reconstruction to reduce slice profile effects, may improve the viability of ultra-short slice-selective RF pulses. The simulation framework could be used to better understand the signals and validate mathematical models to describe signal behavior.

7.3 Summary

In closing, we identified a need for improved iron quantitation techniques at 3T. Through the creation and testing of new scanning and fitting approaches in combination with the characterization of the differences between 1.5T and 3T LIC quantitation, we have enabled reliable LIC quantitation across the clinically relevant range at 3T. Further, we have exposed numerous opportunities to understand treatments and better quantify tissue iron at all available field strengths.

Reference List

- [1] Poggiali E, Cassinerio E, Zanaboni L, Cappellini MD. An update on iron chelation therapy. *Blood Transfus* 2012;10:411–422.
- [2] scielo.cl. Art43_fenton_reaction. <http://www.scielo.cl/fbpe/img/jcchems/v58n4/art43-figure06.jpg>. 2017.
- [3] Clare S. *Functional MRI (fMRI): Methods and Applications*. Ph.D. thesis. University of Nottingham. Nottingham, Nottinghamshire, England, United Kingdom. 1997.
- [4] Wood JC, Enriquez C, Ghugre N, Tyzka JM, Carson S, Nelson MD, Coates TD. MRI R₂ and R_{2*} mapping accurately estimates hepatic iron concentration in transfusion-dependent thalassemia and sickle cell disease patients. *Blood* 2005;106:1460–1465.
- [5] Weisstein EW. Fourier Series. <http://mathworld.wolfram.com/FourierSeries.html>.
- [6] Ghugre NR. *Calibration of Iron-Mediated MRI Relaxation by Monte Carlo Modeling*. Ph.D. thesis. University of Southern California. Los Angeles. 2008.
- [7] Pierre TGS, Clark PR, Chua-anusorn W, Fleming AJ, Jeffrey GP, Olynyk JK, Pootrakul P, Robins E, Lindeman R. Noninvasive measurement and imaging of liver iron concentrations using proton magnetic resonance. *Blood* 2005;105:855–861.
- [8] Brandhagen DJ, Fairbanks VF, Baldus W. Recognition and management of hereditary hemochromatosis. *Am Fam Physician* 2002;65:853–860.
- [9] Aigner E, Theurl I, Theurl M, Lederer D, Haufe H, Dietze O, Strasser M, Datz C, Weiss G. Pathways underlying iron accumulation in human nonalcoholic fatty liver disease. *Am J Clin Nutr* 2008;87:1374–1383.
- [10] NHLBI. What Are Thalassemias? - NHLBI, NIH. <https://www.nhlbi.nih.gov/health/health-topics/topics/thalassemia#>. 2012.

- [11] Chattipakorn N, Kumfu S, Fucharoen S, Chattipakorn S. Calcium channels and iron uptake into the heart. *World J Cardiol* 2011;3:215–218.
- [12] Kohgo Y, Ikuta K, Ohtake T, Torimoto Y, Kato J. Body iron metabolism and pathophysiology of iron overload. *Int J Hematol* 2008;88:7–15.
- [13] Goodsell D. Ferritin and Transferrin. RCSB Protein Data Bank 2002;.
- [14] Bacon BR, Britton RS. The pathology of hepatic iron overload: A free radical-Mediated Process? *Hepatology* 1990;11:127–137.
- [15] Ehlers KH, Levin AR, Markenson AL, Marcus JR, Klein AA, Hilgartner MW, Engle MA. Longitudinal study of cardiac function in thalassemia major. *Ann N Y Acad Sci* 1980;344:397–404.
- [16] Bartzokis G, Tishler TA, Lu PH, Villablanca P, Altshuler LL, Carter M, Huang D, Edwards N, Mintz J. Brain ferritin iron may influence age- and gender-related risks of neurodegeneration. *Neurobiology of Aging* 2007; 28:414–423.
- [17] Harrison SA, Bacon BR. Hereditary hemochromatosis: Update for 2003. *Journal of Hepatology* 2003;38:14–23.
- [18] Smith SW. The Role of Chelation in the Treatment of Other Metal Poisonings. *J Med Toxicol* 2013;9:355–369.
- [19] Jamuar SS, Lai AH. Safety and efficacy of iron chelation therapy with deferiprone in patients with transfusion-dependent thalassemia. *Ther Adv Hematol* 2012;3:299–307.
- [20] Hennigar GR, Greene WB, Walker EM, de Saussure C. Hemochromatosis caused by excessive vitamin iron intake. *Am J Pathol* 1979;96:611–623.
- [21] Angelucci E, Baronciani D, Lucarelli G, Baldassarri M, Galimberti M, Giardini C, Martinelli F, Polchi P, Polizzi V, Ripalti M, Muretto P. Needle liver biopsy in thalassaemia: Analyses of diagnostic accuracy and safety in 1184 consecutive biopsies. *Br J Haematol* 1995;89:757–761.
- [22] Ambu R, Crispioni G, Sciot R, Eyken PV, Parodo G, Iannelli S, Marongiu F, Silvagni R, Nurchi V, Costa V, Faa G, Desmet VJ. Uneven hepatic iron and phosphorus distribution in beta-thalassemia. *Journal of Hepatology* 1995; 23:544–549.
- [23] Emond MJ, Bronner MP, Carlson TH, Lin M, Labbe RF, Kowdley KV. Quantitative Study of the Variability of Hepatic Iron Concentrations. *Clinical Chemistry* 1999;45:340–346.

- [24] Villeneuve JP, Bilodeau M, Lepage R, Côté J, Lefebvre M. Variability in hepatic iron concentration measurement from needle-biopsy specimens. *Journal of Hepatology* 1996;25:172–177.
- [25] From AM, Maleszewski JJ, Rihal CS. Current Status of Endomyocardial Biopsy. *Mayo Clin Proc* 2011;86:1095–1102.
- [26] Lightwood R, Reber HA, Way LW. The risk and accuracy of pancreatic biopsy. *The American Journal of Surgery* 1976;132:189–194.
- [27] Urru SAM, Tandurella I, Capasso M, Usala E, Baronciani D, Giardini C, Visani G, Angelucci E. Reproducibility of liver iron concentration measured on a biopsy sample: A validation study in vivo. *Am J Hematol* 2015;90:87–90.
- [28] Prieto J, Barry M, Sherlock S. Serum Ferritin in Patients with Iron Overload and with Acute and Chronic Liver Diseases. *Gastroenterology* 1975;68:525–533.
- [29] Lipschitz DA, Cook JD, Finch CA. A clinical evaluation of serum ferritin as an index of iron stores. *N Engl J Med* 1974;290:1213–1216.
- [30] de Virgiliis S, Sanna G, Cornacchia G, Argioli F, Murgia V, Porcu M, Cao A. Serum ferritin, liver iron stores, and liver histology in children with thalassaemia. *Arch Dis Child* 1980;55:43–45.
- [31] Puliyel M, Spoto R, Berdoukas VA, Hofstra TC, Nord A, Carson S, Wood J, Coates TD. Ferritin trends do not predict changes in total body iron in patients with transfusional iron overload. *Am J Hematol* 2014;89:391–394.
- [32] Mills SR, Doppman JL, Nienhuis AW. Computed Tomography in the Diagnosis of Disorders of Excessive Iron Storage of the Liver. *J Comput Assist Tomogr* 1977;1:101–104.
- [33] Houang MTW, Skalicka A, Arozena X, Huehns ER, Shaw DG. CORRELATION BETWEEN COMPUTED TOMOGRAPHIC VALUES AND LIVER IRON CONTENT IN THALASSÆMIA MAJOR WITH IRON OVERLOAD. *The Lancet* 1979;313:1322–1323.
- [34] Chapman RW, Williams G, Bydder G, Dick R, Sherlock S, Kreef L. Computed tomography for determining liver iron content in primary haemochromatosis. *Br Med J* 1980;280:440–442.
- [35] Wood JC, Mo A, Gera A, Koh M, Coates T, Gilsanz V. Quantitative computed tomography assessment of transfusional iron overload. *Br J Haematol* 2011;153:780–785.

- [36] Wood JC. Estimating tissue iron burden: Current status and future prospects. *Br J Haematol* 2015;170:15–28.
- [37] Longo R, Ricci C, Masutti F, Vidimari R, Croce LS, Bercich L, Tiribelli CM, Palma LD. Fatty Infiltration of the Liver: Quantification by ¹H Localized Magnetic Resonance Spectroscopy and Comparison with Computed Tomography. *Invest Radiol* 1993;28:297–302.
- [38] Pearce MS, Salotti JA, Little MP, McHugh K, Lee C, Kim KP, Howe NL, Ronckers CM, Rajaraman P, Craft AW, Parker L, Berrington de González A. Radiation exposure from CT scans in childhood and subsequent risk of leukaemia and brain tumours: A retrospective cohort study. *The Lancet* 2012;380:499–505.
- [39] Brittenham GM, Farrell DE, Harris JW, Feldman ES, Danish EH, Muir WA, Tripp JH, Bellon EM. Magnetic-susceptibility measurement of human iron stores. *N Engl J Med* 1982;307:1671–1675.
- [40] Wood JC. Diagnosis and management of transfusion iron overload: The role of imaging. *Am J Hematol* 2007;82:1132–1135.
- [41] Kaltwasser JP, Gottschalk R, Schalk KP, Hartl W. Non-invasive quantitation of liver iron-overload by magnetic resonance imaging. *Br J Haematol* 1990; 74:360–363.
- [42] Jensen PD, Jensen FT, Christensen T, Ellegaard J. Non-invasive assessment of tissue iron overload in the liver by magnetic resonance imaging. *Br J Haematol* 1994;87:171–184.
- [43] Mazza P, Giua R, Marco SD, Bonetti MG, Amurri B, Masi C, Lazzari G, Rizzo C, Cervellera M, Peluso A, Et A. Iron overload in thalassemia: Comparative analysis of magnetic resonance imaging, serum ferritin and iron content of the liver. *Haematologica* 1995;80:398–404.
- [44] Yan SQ, Sun JZ, Yan YQ, Wang H, Lou M. Evaluation of Brain Iron Content Based on Magnetic Resonance Imaging (MRI): Comparison among Phase Value, R2* and Magnitude Signal Intensity. *PLOS ONE* 2012;7:e31748.
- [45] Noetzli LJ, Papudesi J, Coates TD, Wood JC. Pancreatic iron loading predicts cardiac iron loading in thalassemia major. *Blood* 2009;114:4021–4026.
- [46] Papakonstantinou O, Alexopoulou E, Economopoulos N, Benekos O, Kattamis A, Kostaridou S, Ladis V, Efsthathopoulos E, Gouliamos A, Kelekis NL. Assessment of iron distribution between liver, spleen, pancreas, bone marrow, and myocardium by means of R2 relaxometry with MRI in patients with β -thalassemia major. *J Magn Reson Imaging* 2009;29:853–859.

- [47] Bloch F. Nuclear Induction. *Phys Rev* 1946;70:460–474.
- [48] Torrey HC. Bloch Equations with Diffusion Terms. *Phys Rev* 1956;104:563–565.
- [49] Ghugre NR, Coates TD, Nelson MD, Wood JC. Mechanisms of tissue-iron relaxivity: Nuclear magnetic resonance studies of human liver biopsy specimens. *Magn Reson Med* 2005;54:1185–1193.
- [50] Zuyderhoudt FM, Hengeveld P, van Gool J, Jörning GG. A method for measurement of liver iron fractions in needle biopsy specimens and some results in acute liver disease. *Clin Chim Acta* 1978;86:313–321.
- [51] Yamada I, Aung W, Himeno Y, Nakagawa T, Shibuya H. Diffusion Coefficients in Abdominal Organs and Hepatic Lesions: Evaluation with Intravoxel Incoherent Motion Echo-planar MR Imaging. *Radiology* 1999;210:617–623.
- [52] Engelhardt R, Langkowski JH, Fischer R, Nielsen P, Kooijman H, Heinrich HC, Bücheler E. Liver iron quantification: Studies in aqueous iron solutions, iron overloaded rats, and patients with hereditary hemochromatosis. *Magnetic Resonance Imaging* 1994;12:999–1007.
- [53] Papakonstantinou O, Kostaridou S, Maris T, Gouliamos A, Premetis E, Kouloulias V, Nakopoulou L, Kattamis C. Quantification of liver iron overload by T2 quantitative magnetic resonance imaging in thalassemia: Impact of chronic hepatitis C on measurements. *J Pediatr Hematol Oncol* 1999 Mar-Apr;21:142–148.
- [54] Bulte JW, Miller GF, Vymazal J, Brooks RA, Frank JA. Hepatic hemosiderosis in non-human primates: Quantification of liver iron using different field strengths. *Magn Reson Med* 1997;37:530–536.
- [55] Alexopoulou E, Stripeli F, Baras P, Seimenis I, Kattamis A, Ladis V, Efstathopoulos E, Brountzos EN, Kelekis AD, Kelekis NL. R2 relaxometry with MRI for the quantification of tissue iron overload in β -thalassemic patients. *J Magn Reson Imaging* 2006;23:163–170.
- [56] Jensen J, Chandra R. Theory of nonexponential NMR signal decay in liver with iron overload or superparamagnetic iron oxide particles. *Magn Reson Med* 2002;47:1131–1138.
- [57] Ghugre NR, Wood JC. Relaxivity-iron calibration in hepatic iron overload: Probing underlying biophysical mechanisms using a Monte Carlo model. *Magn Reson Med* 2011;65:837–847.

- [58] Ghugre NR, Doyle EK, Storey P, Wood JC. Relaxivity-iron calibration in hepatic iron overload: Predictions of a Monte Carlo model. *Magn Reson Med* 2015;74:879–883. epub:September 19, 2014.
- [59] Stanisz GJ, Odrobina EE, Pun J, Escaravage M, Graham SJ, Bronskill MJ, Henkelman RM. T1, T2 relaxation and magnetization transfer in tissue at 3T. *Magn Reson Med* 2005;54:507–512.
- [60] Meloni A, Zmyewski H, Rienhoff HY Jr, Jones A, Pepe A, Lombardi M, Wood JC. Fast approximation to pixelwise relaxivity maps: Validation in iron overloaded subjects. *Magn Reson Imaging* 2013;31:1074–1080.
- [61] Yamada S, Matsuzawa T, Yamada K, Yoshioka S, Ono S, Hishinuma T. A Modified Signal Intensity Equation of Carr-Purcell-Meiboom-Gill Pulse Sequence for MR Imaging. *Tohoku J Exp Med* 1989;158:203–209.
- [62] Urbanchek MG, Picken EB, Kallaiainen LK, Kuzon WM. Specific Force Deficit in Skeletal Muscles of Old Rats Is Partially Explained by the Existence of Denervated Muscle Fibers. *J Gerontol A Biol Sci Med Sci* 2001; 56:B191–B197.
- [63] Overmoyer BA, McLaren CE, Brittenham GM. Uniformity of liver density and nonheme (storage) iron distribution. *Arch Pathol Lab Med* 1987; 111:549–554.
- [64] Christoforidis A, Perifanis V, Spanos G, Vlachaki E, Economou M, Tsatra I, Athanassiou-Metaxa M. MRI assessment of liver iron content in thalassamic patients with three different protocols: Comparisons and correlations. *Eur J Haematol* 2009;82:388–392.
- [65] Gandon Y, Olivié D, Guyader D, Aubé C, Oberti F, Sebille V, Deugnier Y. Non-invasive assessment of hepatic iron stores by MRI. *Lancet* 2004;363:357–362.
- [66] St Pierre TG, Clark PR, Chua-anusorn W. Single spin-echo proton transverse relaxometry of iron-loaded liver. *NMR Biomed* 2004;17:446–458.
- [67] Gudbjartsson H, Patz S. The Rician Distribution of Noisy MRI Data. *Magn Reson Med* 1995;34:910–914.
- [68] Ghugre NR, Gonzalez-Gomez I, Shimada H, Coates TD, Wood JC. Quantitative analysis and modelling of hepatic iron stores using stereology and spatial statistics. *J Microsc* 2010;238:265–274.

- [69] Ghugre NR, Gonzalez-Gomez I, Butensky E, Noetzli L, Fischer R, Williams R, Harmatz P, Coates TD, Wood JC. Patterns of hepatic iron distribution in patients with chronically transfused thalassemia and sickle cell disease. *Am J Hematol* 2009;84:480–483.
- [70] Michaelis L, Coryell CD, Granick S. Ferritin Iii. the Magnetic Properties of Ferritin and Some Other Colloidal Ferric Compounds. *J Biol Chem* 1943; 148:463–480.
- [71] Shoden A, Sturgeon P. Hemosiderin. *AHA* 2004;23:376–392.
- [72] Storey P, Thompson AA, Carqueville CL, Wood JC, de Freitas RA, Rigsby CK. R2* imaging of transfusional iron burden at 3T and comparison with 1.5T. *J Magn Reson Imaging* 2007;25:540–547.
- [73] Ghugre NR, Enriquez CM, Coates TD, Nelson MD, Wood JC. Improved R2* measurements in myocardial iron overload. *J Magn Reson Imaging* 2006; 23:9–16.
- [74] Yablonskiy DA, Haacke EM. Theory of NMR signal behavior in magnetically inhomogeneous tissues: The static dephasing regime. *Magn Reson Med* 1994; 32:749–763.
- [75] Guo H, Au WY, Cheung JS, Kim D, Jensen JH, Khong PL, Chan Q, Chan KC, Tosti C, Tang H, Brown TR, Lam WW, Ha SY, Brittenham GM, Wu EX. Myocardial T2 Quantitation in Patients With Iron Overload at 3 Tesla. *J Magn Reson Imaging* 2009;30:394–400.
- [76] Chappell KE, Patel N, Gatehouse PD, Main J, Puri BK, Taylor-Robinson SD, Bydder GM. Magnetic resonance imaging of the liver with ultrashort TE (UTE) pulse sequences. *J Magn Reson Imaging* 2003;18:709–713.
- [77] Gatehouse PD, Bydder GM. Magnetic Resonance Imaging of Short T2 Components in Tissue. *Clinical Radiology* 2003;58:1–19.
- [78] Li Y, Chen Z, Wang J. Differential diagnosis between malignant and benign hepatic tumors using apparent diffusion coefficient on 1.5-T MR imaging: A meta analysis. *Eur J Radiol* 2012;81:484–490.
- [79] Wood JC, Zhang P, Rienhoff H, Abi-Saab W, Neufeld E. R2 and R2* are equally effective in evaluating chronic response to iron chelation. *Am J Hematol* 2014;89:505–508.
- [80] Greenman RL, Shirosky JE, Mulkern RV, Rofsky NM. Double inversion black-blood fast spin-echo imaging of the human heart: A comparison between 1.5T and 3.0T. *J Magn Reson Imaging* 2003;17:648–655.

- [81] Hornak JP, Szumowski J, Bryant RG. Magnetic field mapping. *Magn Reson Med* 1988;6:158–163.
- [82] Yarnykh VL. Actual flip-angle imaging in the pulsed steady state: A method for rapid three-dimensional mapping of the transmitted radiofrequency field. *Magn Reson Med* 2007;57:192–200.
- [83] Wood JC, Cohen AR, Pressel SL, Aygun B, Imran H, Luchtman-Jones L, Thompson AA, Fuh B, Schultz WH, Davis BR, Ware RE, the TWiTCH Investigators. Organ iron accumulation in chronically transfused children with sickle cell anaemia: Baseline results from the TWiTCH trial. *Br J Haematol* 2016;172:122–130.
- [84] Stankiewicz J, Panter SS, Neema M, Arora A, Batt C, Bakshi R. Iron in Chronic Brain Disorders: Imaging and Neurotherapeutic Implications. *Neurotherapeutics* 2007;4:371–386.
- [85] Alústiza Echeverría JM, Castiella A, Emparanza JI. Quantification of iron concentration in the liver by MRI. *Insights Imaging* 2011;3:173–180.
- [86] Josan S, Kaye E, Pauly JM, Daniel BL, Pauly KB. Improved half RF slice selectivity in presence of eddy currents with out-of-slice saturation. *Magn Reson Med* 2009;61:1090–1095.
- [87] Cook JD, Finch CA, Smith NJ. Evaluation of the iron status of a population. *Blood* 1976;48:449–455.
- [88] Hernando D, Liang ZP, Kellman P. Chemical shift-based water/fat separation: A comparison of signal models. *Magn Reson Med* 2010;64:811–822.
- [89] Eamon Doyle. Cornercase/snapshot_research_ute_vs_gre_LIC: Post-acceptance revision. Zenodo 2017;.
- [90] Meloni A, Positano V, Keilberg P, De Marchi D, Pepe P, Zuccarelli A, Campisi S, Romeo MA, Casini T, Bitti PP, Gerardi C, Lai ME, Piraino B, Giuffrida G, Secchi G, Midiri M, Lombardi M, Pepe A. Feasibility, reproducibility, and reliability for the T^{*2} iron evaluation at 3 T in comparison with 1.5 T. *Magn Reson Med* 2012;68:543–551.
- [91] Alam MH, Auger D, McGill LA, Smith GC, He T, Izgi C, Baksi AJ, Wage R, Drivas P, Firmin DN, Pennell DJ. Comparison of 3 T and 1.5 T for T2* magnetic resonance of tissue iron. *J Cardiovasc Magn Reson* 2016;18.
- [92] Hernando D, Kramer JH, Reeder SB. Multipeak fat-corrected complex R2* relaxometry: Theory, optimization, and clinical validation. *Magn Reson Med* 2013;70:1319–1331.

- [93] Wood JC, Zhang P, Rienhoff H, Abi-Saab W, Neufeld EJ. Liver MRI is more precise than liver biopsy for assessing total body iron balance: A comparison of MRI relaxometry with simulated liver biopsy results. *Magn Reson Imaging* 2015;33:761–767.
- [94] He T, Gatehouse PD, Kirk P, Mohiaddin RH, Pennell DJ, Firmin DN. Myocardial T^{*}2 measurement in iron-overloaded thalassemia: An ex vivo study to investigate optimal methods of quantification. *Magn Reson Med* 2008;60:350–356.
- [95] Garbowski MW, Carpenter JP, Smith G, Roughton M, Alam MH, He T, Pennell DJ, Porter JB. Biopsy-based calibration of T2* magnetic resonance for estimation of liver iron concentration and comparison with R2 Ferriscan. *J Cardiovasc Magn Reson* 2014;16:40.
- [96] Gai ND, Malayeri A, Agarwal H, Evers R, Bluemke D. Evaluation of optimized breath-hold and free-breathing 3D ultrashort echo time contrast agent-free MRI of the human lung. *J Magn Reson Imaging* 2016;43:1230–1238.
- [97] Tyler DJ, Robson MD, Henkelman RM, Young IR, Bydder GM. Magnetic resonance imaging with ultrashort TE (UTE) PULSE sequences: Technical considerations. *J Magn Reson Imaging* 2007;25:279–289.
- [98] Pauly JM, Conolly SM, Nishimura DG. Magnetic resonance imaging of short T₂ species with improved contrast. 1992. u.S. Classification: 324/309 International Classification: : G01R 3320.
- [99] Hernando D, Levin YS, Sirlin CB, Reeder SB. Quantification of Liver Iron with MRI: State of the Art and Remaining Challenges. *J Magn Reson Imaging* 2014;40:1003–1021.
- [100] Krafft AJ, Loeffler RB, Song R, Tipirneni-Sajja A, McCarville MB, Robson MD, Hankins JS, Hillenbrand CM. Quantitative ultrashort echo time imaging for assessment of massive iron overload at 1.5 and 3 Tesla. *Magn Reson Med* 2017;pp. n/a–n/a.
- [101] Ma D, Gulani V, Seiberlich N, Liu K, Sunshine JL, Duerk JL, Griswold MA. Magnetic Resonance Fingerprinting. *Nature* 2013;495:187–192.
- [102] Finch CA, Hegsted M, Kinney TD, Thomas ED, Rath CE, Haskins D, Finch S, Fluharty RG. Iron Metabolism. *Blood* 1950;5:983–1008.
- [103] Saito H, Hayashi H. Transformation rate between ferritin and hemosiderin assayed by serum ferritin kinetics in patients with normal iron stores and iron overload. *Nagoya J Med Sci* 2015;77:571–583.